

## Università degli Studi di Napoli *Federico II*

DOTTORATO DI RICERCA IN  
**FISICA FONDAMENTALE ED APPLICATA**

Ciclo: XVII

Coordinatore: Prof. Raffaele Velotta

### **Search for Tau Neutrinos in the $\tau \rightarrow e$ Decay Channel in the OPERA Experiment**

Settore Scientifico Disciplinare FIS/01

**Dottorando**  
[Behzad Hosseini](#)

**Tutore:**  
Prof. [Giovanni De Lellis](#)

Anni 2012/2015



Wings are a constraint that makes  
it possible to fly.  
— Robert Bringhurst

To my family ...



# Contents

<b>List of figures</b>	<b>v</b>
<b>List of tables</b>	<b>xi</b>
<b>Introduction</b>	<b>1</b>
<b>1 Neutrino Oscillations</b>	<b>3</b>
1.1 A Brief History Of Neutrino Discovery . . . . .	3
1.1.1 Discovery Of Electron Neutrino . . . . .	3
1.1.2 Discovery Of Muon Neutrino . . . . .	4
1.1.3 Discovery Of Tau Neutrino . . . . .	5
1.2 The Mass of Neutrinos . . . . .	6
1.3 Neutrino Oscillations . . . . .	7
1.4 Mikheyev-Smirnov-Wolfenstein Effect . . . . .	12
1.5 Neutrino Oscillation Experiments . . . . .	13
1.5.1 Solar Neutrinos . . . . .	14
1.5.2 Atmospheric Neutrino Experiments . . . . .	17
1.5.3 Search for $\theta_{13}$ . . . . .	20
1.5.4 Summary of neutrino oscillation parameters . . . . .	22
<b>2 The OPERA Experiment</b>	<b>25</b>
2.1 The CNGS Neutrino Beam . . . . .	25
2.2 The OPERA Detector . . . . .	28
2.3 Emulsion Target . . . . .	28
2.4 Target Tracker . . . . .	29
2.5 Muon Spectrometers . . . . .	30
2.6 VETO System . . . . .	32
2.7 Automated Scanning System . . . . .	32
2.8 Physics Performances . . . . .	34
2.8.1 Tau detection and signal efficiency . . . . .	34
2.8.2 Background . . . . .	36
2.8.3 Sensitivity to $\nu_\mu \rightarrow \nu_\tau$ oscillation . . . . .	39
2.8.4 The fourth $\nu_\tau$ candidate event . . . . .	40

## Contents

---

<b>3 Search For <math>\nu_\tau</math> Interactions in <math>\tau \rightarrow e</math> Decay Channel</b>	<b>45</b>
3.1 Monte Carlo Event Simulation . . . . .	45
3.2 Electronic Detector Analysis . . . . .	48
3.2.1 Event Classification . . . . .	48
3.2.2 MuonID Classification . . . . .	48
3.2.3 Brick Finding . . . . .	48
3.3 Emulsion Analysis Chain . . . . .	49
3.3.1 Changeable Sheet Analysis . . . . .	50
3.3.2 CS to Brick Connection . . . . .	51
3.3.3 Scan-back . . . . .	52
3.3.4 Volume Scan . . . . .	53
3.3.5 Vertex Reconstruction . . . . .	54
3.3.6 Decay Search . . . . .	55
3.4 Event Location and Decay Search Efficiency Assessment . . . . .	56
3.4.1 Efficiency Assessment with Monte Carlo Simulations . . . . .	56
3.4.2 Efficiency Assessment Base on Data . . . . .	58
<b>4 Energy Estimation of Electromagnetic Showers</b>	<b>61</b>
4.1 Purposes of this Analysis . . . . .	61
4.2 Basetrack Construction . . . . .	62
4.3 Shower Reconstruction in ECC Bricks . . . . .	64
4.3.1 Passage of particles inside the matter . . . . .	64
4.3.2 Selection of the signal . . . . .	68
4.3.3 Background Evaluation . . . . .	68
4.3.4 Variables . . . . .	70
4.3.5 Boosted Decision Tree . . . . .	74
4.4 Energy Estimation by Using One or Two ECC Bricks . . . . .	76
4.4.1 Definition of different zones within the Brick . . . . .	77
4.4.2 Events in Zone1 . . . . .	80
4.4.3 Events in Zone2 . . . . .	86
4.5 $\nu_e$ Analysis . . . . .	91
4.5.1 zone1 . . . . .	92
4.5.2 zone2 . . . . .	93
<b>5 Results</b>	<b>95</b>
5.1 $\nu_e$ Data Analysis . . . . .	95
5.1.1 Event 9197043461 . . . . .	95
5.1.2 Event 226395185 . . . . .	99
5.2 Kinematical Selection . . . . .	103
5.3 Overall Detection Efficiency . . . . .	104
<b>Conclusion</b>	<b>107</b>

## **Contents**

---

<b>Acknowledgments</b>	<b>119</b>
------------------------	------------



# List of Figures

1.1	Energy spectrum of the electron in $\beta$ -decay [2]. . . . .	3
1.2	The schematic diagram of Brookhaven experiment [12]. . . . .	5
1.3	The diagram for the terms in the three-neutrino oscillation probability [27]. . . . .	9
1.4	Coherent forward scattering diagrams for neutrinos going through matter [29]. . . . .	12
1.5	Solar neutrino flux from different reactions at the Earth's surface, together with the energy thresholds of the experiments performed so far [31]. . . . .	14
1.6	Best fit regions at 90, 99 and 99.73 % C.L. obtained fitting solar neutrino data (red dashed contours); reactor antineutrino data (blue dotted contours); all data (shaded region) [47]. . . . .	16
1.7	Left: Atmospheric neutrinos produced in Earth's atmosphere, Right: A sketch showing the relation between zenith angle and the distance travelled by atmospheric neutrinos. . . . .	17
1.8	Points with error bars: data; Red: Monte Carlo without oscillations; Green: Monte Carlo with best-fitted oscillation effects [56]. . . . .	18
1.9	Number of muon-like events in Super-Kamiokande as a function of L/E (points). The histogram shows the Monte Carlo prediction without oscillations [58]. . . . .	19
1.10	Measured prompt energy spectrum of the far detector compared with the no oscillation (top) and their ratio (bottom) from the measurements of the two near detectors. Only statistical errors are shown [66]. . . . .	20
1.11	Measured prompt energy spectrum in the Far hall compared to extrapolation of the Near halls detected flux assuming no oscillation (top) and their ratio (bottom). If there were no oscillation the Far/Near ratio should always be 1 (dashed line in the bottom plot). The red line shows the best $\nu e$ disappearance fit. Only statistical errors are shown [68]. . . . .	21
1.12	The ratio of the measured spectrum of far detector to the no oscillation prediction [70]. . . . .	21
1.13	Three neutrino $\Delta m^2$ Pattern of squared neutrino mass and flavor components: Normal and inverted hierarchies [72]. . . . .	22
1.14	Limits on oscillation parameters inferred from data of oscillation experiments. One can see the allowed region for atmospheric sector (upper-middle part, conjunction of Super-Kamiokande and K2K allowed regions) and for solar sector (middle part, SNO and KamLand). LSND and MiniBoone results in the upper part of the plot [74]. . . . .	23

## List of Figures

---

2.1 Main components of the CNGS beam line [80]. . . . .	26
2.2 The energy of CNGS beam spectrum and oscillation probability multiplied by the $\nu_\tau$ cross section [81]. . . . .	26
2.3 Overview of the OPERA detector [83]. . . . .	27
2.4 Schematic structure of an ECC brick. . . . .	28
2.5 Schematic view of the two scintillator planes of a TT wall on the left, and a scintillator strip with the wave length shifting fibers on the right [87, 88]. . . . .	29
2.6 Schematic view of a $\nu_\tau$ CC interaction and the decay of its final state $\tau$ lepton as it would appear inside the brick, in the CS emulsion films and in the TT strips [90].	30
2.7 Drift plane arrangement in the muon spectrometer. Also shown are two planes of RPC's with inclined strips (XPC's) [95]. . . . .	31
2.8 Schematic view of a XPC detector plane [96]. . . . .	31
2.9 A schematic view of the ESS microscope (left); Taking a series of successive images in different depths of the Emulsion (right). . . . .	33
2.10 Micro-track reconstruction in one emulsion layer by combining clusters belonging to images at different levels (left); micro-track connections across the plastic base to form base-tracks (right). . . . .	33
2.11 $\tau$ decay length distribution. . . . .	34
2.12 Schematic picture of the $\tau$ detection technique in the ECC cell for short (top) and long (bottom) decays [102]. . . . .	35
2.13 Impact parameter measured in data and compared with simulation. . . . .	36
2.14 $\tau$ kink angle distribution for the $\tau \rightarrow e$ decay mode. . . . .	36
2.15 Tau decay topology in the $\nu_\tau^{CC}$ and the corresponding background from one prong decay of charmed particles when the produced muon is missed. . . . .	37
2.16 Schematic view of the background from large angle muon scattering. A scattered muon could be as same as the decay of $\tau \rightarrow \mu$ channel. . . . .	37
2.17 Topologies of the $\nu_\tau$ signal (a), background from hadron re-interactions from $\nu_\mu^{NC}$ (b) and $\nu_\mu^{CC}$ (c). . . . .	38
2.18 The present data analysis status of OPERA. . . . .	39
2.19 Display of the $\nu_\tau$ candidate event as seen by the electronic detectors in the x-z projection (top) and y-z projection (bottom). The brick containing the neutrino interaction is highlighted in magenta. Solid lines show the position of tracks measured in the primary and downstream bricks. Dashed lines show the linear extrapolation of the tracks using positions and slopes at the last measured point in the bricks [106]. . . . .	41
2.20 Event display of the fourth $\nu_\tau$ candidate event; Left: the y-z projection longitudinal to the neutrino direction, Right: the view transverse to the neutrino direction. The primary and decay vertices are indicated as "v1" and "v2" respectively [106].	42
2.21 The $\tau$ direction (red arrow) and the other primary particles (black arrows) in the plane transverse to the beam. The blue arrow shows the vectorial sum of the primary particles except the parent.. . . . .	42

3.1 Flow diagram of the analysis chain to search for neutrino interactions [113]. . .	46
3.2 Whole detector display in (a) x-z and (b) y-z projections for an event classified as $1\mu$ ; and (c) and (d) show x-z and y-z projections respectively, for a $0\mu$ event. . .	49
3.3 The $3 \times 3 \times 3$ matrix where the brick identification algorithm is applied. The true brick where the interaction occurred is the 111. . . . .	50
3.4 After the bricks are extracted, the CS scanning result is superimposed to a zoom of the TT display. Clearly brick B contains the event and it is thus developed. . .	50
3.5 The alignment between the two layers is done by matching the Compton- electron tracks [117]. . . . .	51
3.6 Schematic representation of the "scanback" procedure. When the track disappear for 5 consecutive plates the interaction point is located [117]. . . . .	52
3.7 Schematic drawing of the volume scan. Scanning 10 plates downstream of the stopping point and 5 upstream prepare this volume. . . . .	53
3.8 Impact parameter distribution of the primary tracks in $1\mu$ events with respect to the reconstructed vertex, after the primary vertex definition. The distribution is normalized to unity. . . . .	55
3.9 The parent search procedure consists of searching for segments connecting an extra-track to the primary vertex. . . . .	56
4.1 The principle of base-track reconstruction: the micro-tracks matching are obtained when an acceptable agreement in slope and position is found. Joining the two points closer to the base forms the base-track. . . . .	63
4.2 Base-track $\chi^2$ distribution for the MC signal with the cut $\chi^2 < 2.5$ . . . . .	64
4.3 Energy loss mechanism for electrons and positrons in copper. Above the "critical energy" the main mechanism is the emission of bremsstrahlung radiation. . . .	65
4.4 Cross section for the interactions of photons in lead. At high energies ( $> 10$ MeV) the main contribution is pair production [120]. . . . .	65
4.5 Two-dimensional model of an electromagnetic shower. Two processes, bremsstrahlung and pair production are responsible for the energy degradation and the shower development. . . . .	66
4.6 A schematic view of electromagnetic shower reconstruction within the brick. .	67
4.7 Fraction of selected base-tracks as a function of the opening angle of the cone.	69
4.8 Alpha definition for each base-track inside the cone. . . . .	70
4.9 The value of " $\alpha$ " angle; Left: Signal, Right: Background. . . . .	70
4.10 The impact parameter, IP, calculated for each base-track . . . . .	71
4.11 The value of " $\frac{IP}{\Delta Z}$ "; Left: Signal, Right: Background. . . . .	72
4.12 $\Delta S_x$ and $\Delta S_y$ distribution; Top Left: $\Delta S_x$ for Signal, Top Right: $\Delta S_x$ for Background, Bottom Left: $\Delta S_y$ for Signal, Bottom Right: $\Delta S_y$ for Background . . . .	73
4.13 The " $\chi^2$ " distribution in the reconstruction of base-tracks; Left: Signal, Right: Background. . . . .	73

## List of Figures

---

4.14 A BDT as obtained from the TMVA toolkit. The tree is grown from a sequence of splits onto variables, to obtain the highest purity; for example in this tree the highest purity is $P = 0.931$ . . . . .	74
4.15 BDT evaluation plots obtained via the TMVA toolkit; Top Left: Input variable distribution, Top Right: Correlation matrix, Bottom Left: ROC curve, Bottom Right: Overtraining check. . . . .	76
4.16 Profile histogram of the number of base-tracks as the function of the decay point of $\tau$ lepton inside each plate. Each plate corresponds to 1.3 mm thickness with 1 mm of lead. This plot is normalized to 1. . . . .	77
4.17 Profile histogram of the number of tracks reconstructed in the CS as a function of the decat point of $\tau$ . . . . .	78
4.18 A schematic view of the different regions defined in the brick. . . . .	79
4.19 Energy spectrum of electron in $\tau \rightarrow e$ decay channel. . . . .	80
4.20 The normalized distribution of the input variables. Signal distribution is shown in blue and the background distributions is in red; Top Left: Alpha distribution, Top Middle: Impact Parameter over $\Delta Z$ distribution, Top Right: Angular difference in X projection, Bottom Left: Angular difference in Y projection, Bottom Middle: $\chi^2$ distribution. . . . .	81
4.21 The correlation matrix; Left: Signal, Right: Background. . . . .	82
4.22 The cut efficiencies and the optimal cut value coming out by BDT algorithm. The signal tracks having a BDT response greater than 0.2 are selected. . . . .	82
4.23 The calibration curve of the energy as a function of the number of base-tracks for the Zone1 region. . . . .	83
4.24 The $\frac{\Delta E}{E}$ distribution. . . . .	84
4.25 The $\sigma_E$ as a function of the electron energy. . . . .	85
4.26 The 2D schematic view of the electromagnetic showers reconstruction within two bricks. . . . .	86
4.27 Number of base-tracks of the showers within the second brick as the function of the number of plates. . . . .	87
4.28 The region used for the Zone2 analysis; only the first 20 plates of the second brick are used in this work. . . . .	87
4.29 The normalized distribution of the input variables. Signal distribution is shown in blue and the background distributions is in red; Top Left: Alpha distribution, Top Middle: Impact Parameter over $\Delta Z$ distribution, Top Right: $\chi^2$ distribution, Bottom Left: Angular difference in X projection, Bottom Middle: Angular difference in Y projection. . . . .	88
4.30 The correlation matrix; Left: Signal, Right: Background. . . . .	89
4.31 The cut efficiencies and the optimal cut value coming out by BDT algorithm. The signal tracks having a BDT response greater than 0.31 are selected. . . . .	89
4.32 The calibration curve of the energy as a function of the number of base-tracks for the Zone2 region. . . . .	90

---

4.33 The $\frac{\Delta E}{E}$ distribution. . . . .	90
4.34 The $\sigma_E$ as a function of the electron energy. . . . .	91
4.35 The electron neutrino analysis for the Zone1; Left: The calibration curve of the energy versus the number of base-tracks for the Zone1 region, Right: The $\frac{\Delta E}{E}$ distribution. . . . .	92
4.36 The electron neutrino analysis for the Zone2; Left: The calibration curve of the energy versus the number of base-tracks for the Zone2 region, Right: The $\frac{\Delta E}{E}$ distribution. . . . .	93
4.37 Momentum spectrum of electron; Left: in $\tau \rightarrow e$ decay channel, Right: for $\nu_e$ interactions. . . . .	94
5.1 Electronic detector display of the event 9197043461; top: the XZ projection and bottom: the YZ projection. . . . .	96
5.2 Zoom of the target tracker where the interaction took place (it is highlighted in pink). . . . .	96
5.3 Tracks found in the CS analysis. The lengths of the arrows are proportional to their slopes. . . . .	97
5.4 Scan-back tracks in the emulsion films as seen in the projection XZ and YZ. Each plate corresponds to 1.3 mm on the Z axis. . . . .	98
5.5 Vertex display of the interaction contained in the brick 40009. Left: Side View; Right: Front View. . . . .	99
5.6 Electronic detector display of the event 226395185; top: the XZ projection and bottom: the YZ projection. . . . .	100
5.7 Zoom of the target tracker where the interaction occurred (it is highlighted in pink). . . . .	101
5.8 Tracks found in the CS analysis. The lengths of the arrows are proportional to their slopes. . . . .	101
5.9 The base-tracks found in plates 53 and 54. . . . .	102
5.10 A schematic view of the electromagnetic shower reconstruction within two bricks. . . . .	103
5.11 Definition of the $z_{dec}$ variable. Blue rectangles represent the 1 mm lead plates; yellow rectangles represent the emulsion films. . . . .	104
5.12 Distribution of kinematical variables for the $\tau \rightarrow e$ decay channel; Top Left: $z_{dec}$ , Top Right: $p_T^{electron}$ , Bottom Left: kink angle $\theta_{kink}$ , Bottom Right: $E_{electron}$ . . .	105
5.13 Energy distribution of the electrons generated by the $\tau$ decay; Left: before the application of the oscillation probability; Right: after the application of the oscillation probability. . . . .	106



# List of Tables

1.1	Summary of best global fit of neutrino oscillation parameters, taken from [71]. $\Delta m^2$ is defined herein as $m_3^2 - (m_1^2 + m_2^2)/2$ , with $+\Delta m^2$ for NH and $-\Delta m^2$ for IH.	22
2.1	CNGS beam features [75]. . . . .	27
2.2	The $\tau$ decay channels investigated by OPERA [97]. . . . .	34
2.3	The total number of background events for each $\tau$ decay channel. . . . .	38
2.4	Summary of the collected data samples and the contained events. . . . .	39
2.5	Summary of the signal and backgrounds expectations for the analysed sample [106]. . . . .	40
2.6	Selection criteria for the $\nu_\tau$ interaction search in the $\tau \rightarrow 1h$ decay channel and the values measured for the fourth $\nu_\tau$ candidate event [106]. . . . .	43
3.1	MC samples used in the analyses of this work. . . . .	57
3.2	The summary of event location and DS efficiency for each reconstruction step for 2008 and 2009 data selection. The efficiency of each step is cumulative with respect to previous steps. The uncertainties are due to statistical errors. . . . .	58
3.3	The summary of event location and DS efficiency for each reconstruction step for 2010, 2011 and 2012 data selection. The efficiency of each step is cumulative with respect to previous steps. The uncertainties are due to statistical errors. . . . .	58
3.4	Event location and DS efficiency for $\nu_\mu^{CC} \xrightarrow{mis} \nu_\mu^{NC}$ channel for 2008 and 2009 data selection. It is because of the misidentification of the muon track for $\nu_\mu^{CC}$ events. The uncertainties are due to statistical errors. . . . .	59
3.5	Event location and DS efficiency for $\nu_\mu^{CC} \xrightarrow{mis} \nu_\mu^{NC}$ channel for 2010, 2011 and 2012 data selection. The uncertainties are due to statistical errors. . . . .	59
3.6	The summary of event location for OPERA data. . . . .	59
4.1	The length of the electromagnetic shower inside the OPERA bricks. . . . .	78
4.2	The average number of base-tracks in each event . . . . .	92
4.3	The P0, P1 and $\sigma$ given by the fit for $\nu_e$ events . . . . .	92
4.4	The average number of base-tracks in each event . . . . .	93
4.5	The P0, P1 and $\sigma$ given by the fit for $\nu_e$ events . . . . .	93
5.1	Impact parameters of the particles attached to the primary vertex. . . . .	98
5.2	Selection criteria for the $\nu_\tau$ interaction search in the $\tau \rightarrow e$ decay channel. . . . .	104

## **List of Tables**

---

5.3	Summary of the $\tau$ detection efficiency for 2008-2009 data selection. The uncertainties are due to statistical errors. . . . .	105
5.4	Summary of the $\tau$ detection efficiency for 2008-2009 data selection done in the previous analysis [125]. . . . .	106

# Introduction

The only particles that experiencing the weak interaction are “neutrinos”. Thus, the study of weak forces requires the unique neutrino particles. Neutrino interactions are a powerful tool to investigate the internal structure of the nucleons as well as astrophysical objects.

Neutrino physics during the last decades has improved impressively. Neutrinos are classified as a fundamental particle in the Standard Model (SM) and are regarded as massless particles. Nevertheless, the solar neutrino deficit and the atmospheric neutrino anomaly, observed and confirmed by several neutrino experiments, stimulated the hypothesis that neutrinos have a non null mass and oscillate. If neutrinos are not massless and if mass and flavor eigenstates do not coincide, the Standard Model requires an extension.

There are experimental evidences suggesting the  $\nu_\mu \rightarrow \nu_\tau$  oscillation in the atmospheric sector, but a direct evidence of the  $\nu_\tau$  appearance was missing. This fact requires a detector with the capability of detecting the short-lived  $\tau$  lepton produced in  $\nu_\tau$  Charged Current interactions.

The OPERA experiment was designed to provide a conclusive proof of the neutrino oscillations hypothesis in the  $\nu_\mu \rightarrow \nu_\tau$  channel through the observation of the  $\tau$  lepton in the region indicated by the Super-Kamiokande experiment. A very pure  $\nu_\mu$  beam, produced by the SPS accelerator at CERN, travels 730 km to reach the OPERA detector, located at LNGS. After five years data taking, from 2008 to 2012, OPERA has recorded neutrino interactions equivalent to  $\sim 1.8 \times 10^{20}$  pot and has discovered four  $\nu_\tau$  candidates so far.

Having observed four  $\nu_\tau$  candidates with a background of 0.23 events,  $\nu_\mu \rightarrow \nu_\tau$  oscillations are established at  $4.2\sigma$  level.

This PhD work is done in the framework of Napoli group contributing to the OPERA experiment. The main goal of the work is to study the full analysis chain of neutrino interactions in the OPERA detector and to develop a new method to estimate the energy of electromagnetic showers for the detection of the  $\tau \rightarrow e$  decay in the search for neutrino oscillations. In this work the OPERA ECC brick is used as a calorimeter to reconstruct the electromagnetic shower and to estimate the energy of the electron within the brick. It exploits the correlation between the energy of the electron and the number of produced shower tracks detected through its electromagnetic shower. Possible physical and instrumental backgrounds have been also considered in this study, as they may influence the number of shower tracks detected inside

## Introduction

---

the brick.

Due to the electron identification capability exploited for the reconstruction of the  $\tau \rightarrow e$  decay, OPERA is able to perform also a  $\nu_\mu \rightarrow \nu_e$  oscillation search. In the CNGS beam the expected  $\nu_e$  contamination is relatively small compared to the dominant  $\nu_\mu$  component ( $\nu_e/\nu_\mu = 0.8\%$ ) and allows search for the oscillation  $\nu_\mu \rightarrow \nu_e$  seeking an excess of  $\nu_e$  charged current events. Although the energy of the neutrino beam is high enough to be optimized for the  $\nu_\tau$  search rather than for  $\nu_e$ . This analysis is thus also useful for the  $\nu_\mu \rightarrow \nu_e$  oscillation search and the energy is a key element to discriminate between oscillated events (low energy) and the  $\nu_e$  contamination in the beam (high energy).

The content of this thesis is structured in five chapters: the first chapter presents the neutrino history and the neutrino detection. The three-flavor neutrino oscillation phenomenon will be discussed. The last part of this chapter explains the experimental context of neutrino oscillations.

An overview about the OPERA experiment will be reported in the second chapter. First, the CNGS neutrino beam will be described and afterwards, the OPERA detector and physics performances will be detailed.

In the chapter 3 the location procedure of a neutrino interaction in the OPERA target, together with the full analysis chain used to evaluate the detection efficiencies will be described.

Then, in the chapter 4 the description of a new algorithm aimed to analyze showers involving one or two bricks along the beam direction will be presented. The main background sources are described and the relationship between the number of shower tracks found inside the brick and the energy is discussed.

At the end, chapter 5 describes the results for the kinematical selection and also some  $\nu_e$  interactions located in the Napoli scanning lab will be presented.

# 1 Neutrino Oscillations

## 1.1 A Brief History Of Neutrino Discovery

### 1.1.1 Discovery Of Electron Neutrino

In 1930, Wolfgang Pauli first postulated the existence of neutrino (electron neutrino) to explain how the energy and momentum could be conserved in  $\beta$ -decay. The hypothesis of  $\beta$ -decay was that one neutron decays into one electron and one proton [1].



Experimental results had shown that the emitted electrons have a continuous spectrum instead of a single energy as shown in Figure 1.1.

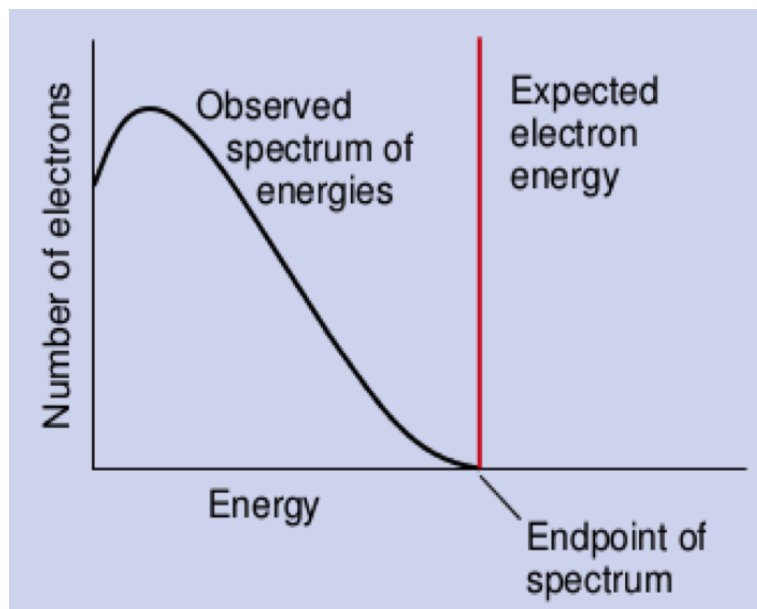


Figure 1.1 – Energy spectrum of the electron in  $\beta$ -decay [2].

For this energy missing in the  $\beta$ -decay, Pauli proposed the existence of a third neutral particle in the  $\beta$ -decay process which escaped detection: “... *I have hit upon a desperate remedy to save the exchange theorem of statistics and the law of conservation of energy. Namely, the possibility that there could exist in the nuclei electrically neutral particles, that I wish to call neutrons, which have spin 1/2 and obey the exclusion principle and which further differ from light quanta in that they do not travel with the velocity of light. The mass of the neutrons should be of the same order of magnitude as the electron mass and in any event not larger than 0.01 proton masses. The continuous beta spectrum would then become understandable by the assumption that in beta decay a neutron is emitted in addition to the electron such that the sum of the energies of the neutron and the electron is constant...*” [3, 4].

In 1932, after Chadwick discovered the neutron [5], the problem of statistics and spin of the nuclei was solved. But the mass of neutrons proved that the neutrons could not be same as the Pauli's particle proposed. Fermi renamed the Pauli's particle as “*neutrino*” in 1933-34 [6]. Therefore the fundamental Beta-decay process turned out to be



After Pauli's hypothesis, measuring the recoil of the nucleus during its beta-decay was one of the main goals of physicist. The first result of all the measurements was the confirmation of the idea that only one neutrino was emitted with the electron. Moreover, it was clear that a big and a very sensitive detector was needed to detect neutrinos.

Around 25 years later in 1956, Cowan and Reines designed an experiment to show the existence of neutrinos [7]; they built a target made of 400 liters of a mixture of cadmium chloride and water and they put this target near a nuclear reactor [8]. So, the electron anti-neutrinos coming from the nuclear reactor interacted with the protons inside the target and produced a neutron and a positron (a process called the inverse  $\beta$ -decay) [9, 10]:



### 1.1.2 Discovery Of Muon Neutrino

Lederman, Schwartz and Steinberger in 1962 [10], proposed an experiment to check the existence of a second type of neutrino associated with a muon rather than an electron. This experiment was carried out at Brookhaven. For this experiment an accelerator was needed because the energies involved in radioactive decays are not high enough to directly produce muons.

A beam of 15 GeV protons produced by the accelerator hits a beryllium target to produce a beam of  $\pi^+$  decaying into muons and neutrinos. The produced pions decayed in a 21 meter long decay tunnel (Figure 1.2).

## 1.1. A Brief History Of Neutrino Discovery

The decay process is [11]

$$\pi^+ \rightarrow \mu^+ + \nu_\mu . \quad (1.4)$$

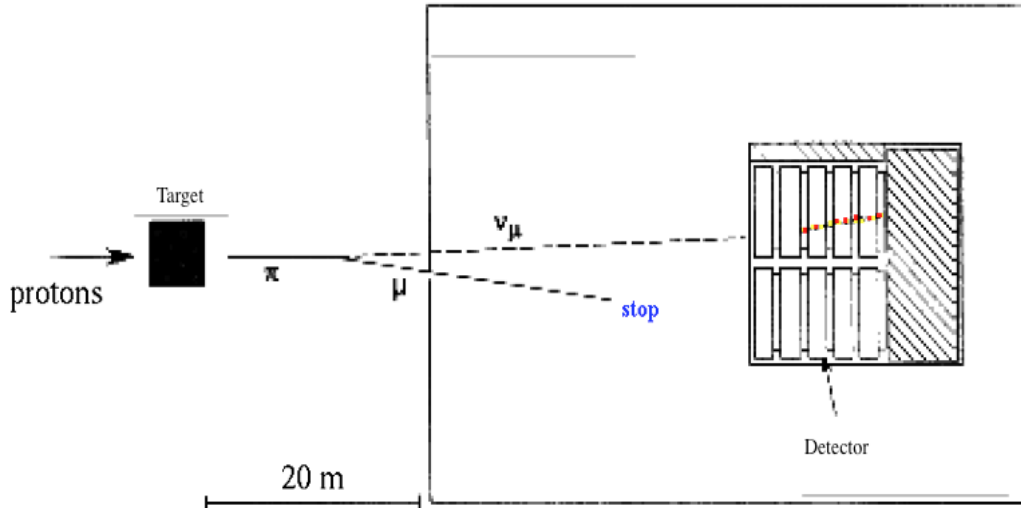


Figure 1.2 – The schematic diagram of Brookhaven experiment [12].

A shielding material, made of 13.5 meter of steel, was located in the end of the decay tunnel, absorbing all the charged particles. After that, a neutrino detector with a weight of 10 tons has been used to observe the production of charged leptons produced in the neutrino interactions. Therefore, by 1962 it became clear that two kinds of neutrinos exist: one associated with electrons (electron-neutrinos,  $\nu_e$ ) and one with muons (muon-neutrinos,  $\nu_\mu$ ) [13].

### 1.1.3 Discovery Of Tau Neutrino

Muon and electron have almost the same properties, however the muon, with the mass of  $m_\mu = 105.66$  MeV, is much heavier than the electron,  $m_e = 0.511$  MeV. This difference in the masses of muon and electron leads scientists to formulate the hypothesis that lepton(s) heavier than muon could exist. In 1957-77, M. Perl et al [14]; performed an experiment to answer to this question where the result was the discovery of the third lepton, tau ( $\tau^\pm$ ), at the  $e^+ + e^-$  collider at Stanford. Therefore, a third type of neutrino,  $\nu_\tau$ , must exist that takes part in the weak interaction together with  $\tau$ . In 2001, this was confirmed by an experiment performed by the DONUT Collaboration at Fermilab [15].

With the discoveries of the W and Z bosons in 1983, the knowledge of weak interactions was completed. A few years later, in 1989, the study of the Z boson at LEP (Large Electron–Positron Collider) showed that only three lepton families and therefore three types of neutrinos exist [16].

## 1.2 The Mass of Neutrinos

The Standard Model (SM) of particle physics [17] is a mathematical description which was formulated in the 60's. Neutrinos in the SM were introduced as massless particles as far as there were no direct evidence for their mass. Also, in the SM no right handed neutrinos,  $\nu_R$ , exist. However, there are left handed neutrinos,  $\nu_L$ , that couples to the W and Z bosons. As a result, in the SM there is no mixing and no CP violation in the lepton sector. But now we know that neutrinos oscillate and therefore they do have masses. To accommodate the neutrino mass in the same way as for quark and charged lepton masses, a right-handed neutrino is needed in the SM. Then the *Dirac mass term* could be written as

$$\mathcal{L}_D = -m_D \bar{\nu}_L \nu_R + h.c., \quad (1.5)$$

where the  $m_D$  is a mass parameter. Similar to the mass terms of charged leptons and quarks, this term conserves the lepton number that discerns neutrinos and leptons with negative charge from anti-neutrinos and leptons with positive charge. In addition, each interaction in the SM conserves the leptonic number for each family,  $L_e$ ,  $L_\mu$  and  $L_\tau$ . Each neutrino mass eigenstate,  $\nu_i$ , varies from its anti-neutrino mass eigenstate,  $\bar{\nu}_i$ , in the sense that  $L(\bar{\nu}_i) = -L(\nu_i)$ . The neutrino is called as *Dirac neutrino* when  $\bar{\nu}_i \neq \nu_i$ . In the other hand, since neutrinos are electrically neutral, a left-handed *Majorana mass term* could be only introduced from a chirally left-handed neutrino

$$\mathcal{L}_{m_L} = -\frac{1}{2} \left[ (\overline{\nu_L})^c m_L \nu_L - \overline{\nu_L} m_L^\dagger (\nu_L)^c \right] = -\frac{m_L}{2} \nu_L^T \nu_L + h.c.. \quad (1.6)$$

Also the right-handed Majorana mass term could be written for right-handed neutrino,  $\nu_R$ , as

$$\mathcal{L}_{m_R} = -\frac{m_R}{2} (\overline{\nu_R})^c \nu_R + h.c., \quad (1.7)$$

where  $\nu^c$  is the charge conjugated of  $\nu$ .  $\mathcal{L}_m$  mixes  $\nu$  and  $\bar{\nu}$  because both  $\nu_R$  and  $\nu_R^c$  absorb neutrino and create anti-neutrino.  $\nu_R^c$  and  $\nu_R$  are not the mass eigenstates and the term  $m_R (\overline{\nu_R})^c \nu_R$  contains  $\nu_R \leftrightarrow \nu_R^c$  mixing, where this mixing yields the neutrino mass eigenstate as  $\nu_i = \nu_R + \nu_R^c$ .

As a summary, in extensions of the standard model within a symmetry group, there are many methods to explain a mass term for the neutrinos. As we also mentioned in this section, a Majorana particle, which is a fermion, is its own antiparticle. On the other hand, Dirac particles are different from their antiparticles. So, depending on the nature of neutrinos, an appropriate mass term can be added to the Lagrangian.

If we consider that the neutrino is a Dirac type neutrino, then it differs from its own antiparticle. Hence, there will be a left-handed neutrino that interacts with a right-handed anti-neutrino via weak interaction. If we assume that the neutrino is a Majorana type neutrino, then the neutrino is its own antiparticle and its mass term in the Lagrangian could be written as both left term (L) and right term (R) as :  $\mathcal{L}_L^{Majorana} + \mathcal{L}_R^{Majorana}$ .

At the moment there is no evidence to say that massive neutrinos are Dirac particles or Majorana particles. Scientists are searching for double beta decays with or without neutrino emission in their final state. If there will be no neutrino in the final state, then the neutrino is a Majorana type neutrino because the conservation of lepton number is violated. Otherwise, it is a Dirac type neutrino and the lepton number is conserved with adding a right-handed partner for each existing left-handed neutrino.

From direct measurements of neutrino masses, the following upper limits for neutrino masses have been acquired. The upper limit for the electron neutrino,  $\nu_e$ , was obtained by measuring the end-point of the high-energy part of the beta-spectrum in the Tritium decay and is given by:

$$m_{\nu_e} \leq 2.3 \text{ eV} \quad (95\% \text{C.L.}) [18]. \quad (1.8)$$

The first limit for the mass of muon neutrino,  $\nu_\mu$ , was obtained by muon momentum analysis in the pion decay ( $\pi^+ \rightarrow \mu + \nu_\mu$ ) and it was:

$$m_{\nu_\mu} \leq 170 \text{ KeV} \quad (90\% \text{C.L.}) [19]. \quad (1.9)$$

The first upper limit for the mass of tau neutrino,  $\nu_\tau$ , is determined from the measurement of the distribution of the effective mass of the five pions in the decay  $\tau \rightarrow \nu_\tau + 5\pi$ . So the upper limit on the mass of  $\nu_\tau$  is:

$$m_{\nu_\tau} \leq 18.2 \text{ MeV} \quad (95\% \text{C.L.}) [20]. \quad (1.10)$$

Furthermore, due to the effect of neutrinos on the structure formation in the early universe other bounds also can be obtained. Combining the two CMB (Cosmic Microwave Background) anisotropy measurements with LSS (Large Scale Structure) data analysis, the upper bound can be reduced to:

$$\sum m_{\nu_i} \leq 0.71 \text{ eV} [21]. \quad (1.11)$$

## 1.3 Neutrino Oscillations

In the 1950s, Bruno Pontecorvo proposed that the neutrino oscillations are a quantum mechanical phenomenon in the analogy with kaon oscillations [22]. Pontecorvo's idea was also including sterile neutrinos, since by that time only electron neutrinos were known.

Afterwards, for the first time in 1962 Maki, Nakagawa and Sakata considered a model with oscillation of different neutrino flavors [23].

In 1970s many physicists, including Pontecorvo and Bilenky [24], developed the modern neutrino oscillation theory.

## Chapter 1. Neutrino Oscillations

---

Neutrino oscillations explain experimental results by allowing neutrino flavor transitions. It is assumed that physically interacting (and observable) flavor eigenstates, like  $\nu_e$  or  $\nu_\mu$  are a combination of mass eigenstates (usually denoted as  $\nu_1, \nu_2, \nu_3$  and etc.). Mass eigenstates propagate through space with different velocities, as they have different masses. This causes the oscillation of neutrino flavor. In other words, this means that if at some point in space a pure beam of neutrinos of one flavor will be produced, the beam will not be anymore pure after traveling some distance. Therefore, if there will be an experiment only sensitive to a certain flavor, a deficit will be observed [25].

The probability of flavor oscillation depends on the type of initial and final neutrino, their energy and the distance they have traveled. Determining these probabilities are one of the main goals of modern neutrino oscillation experiments.

In the framework of three-flavor neutrino oscillation if neutrinos have masses, so three neutrino mass eigenstates exist. The neutrino state is coupled to the W boson by the charged-current interaction. A particular charged lepton is coupled to a flavor eigenstates,  $\nu_e, \nu_\mu$  and  $\nu_\tau$ . Due to the existence of three active neutrinos, the mixing matrix can be a  $3 \times 3$  unitary matrix. In this case we can write

$$\begin{pmatrix} \nu_e \\ \nu_\mu \\ \nu_\tau \end{pmatrix} = \begin{pmatrix} \nu_{e1} & \nu_{e2} & \nu_{e3} \\ \nu_{\mu 1} & \nu_{\mu 2} & \nu_{\mu 3} \\ \nu_{\tau 1} & \nu_{\tau 2} & \nu_{\tau 3} \end{pmatrix} \begin{pmatrix} \nu_1 \\ \nu_2 \\ \nu_3 \end{pmatrix} = U \begin{pmatrix} \nu_1 \\ \nu_2 \\ \nu_3 \end{pmatrix}. \quad (1.12)$$

The matrix  $U$  is known as the Pontecorvo-Maka-Nakagawa-Sakata (PMNS) matrix [26], and it is a unitary matrix so

$$UU^\dagger = U^\dagger U = I \rightarrow U^{-1} = U^\dagger = (U^*)^T. \quad (1.13)$$

So we can also write

$$\begin{pmatrix} \nu_1 \\ \nu_2 \\ \nu_3 \end{pmatrix} = \begin{pmatrix} \nu_{e1}^* & \nu_{\mu 1}^* & \nu_{\tau 1}^* \\ \nu_{e2}^* & \nu_{\mu 2}^* & \nu_{\tau 2}^* \\ \nu_{e3}^* & \nu_{\mu 3}^* & \nu_{\tau 3}^* \end{pmatrix} \begin{pmatrix} \nu_e \\ \nu_\mu \\ \nu_\tau \end{pmatrix}. \quad (1.14)$$

To calculate the oscillation probability lets just assume that we have a neutrino in a pure flavor eigenstate  $|\nu_\alpha(0)\rangle$  state at time  $t=0$

$$|\nu_\alpha(0)\rangle = |\nu_\alpha\rangle = \sum_{i=1}^3 U_{\alpha i}^* |\nu_i\rangle. \quad (1.15)$$

Therefore the wave function evolves as

$$|\nu_\alpha(t)\rangle = \sum_{i=1}^3 U_{\alpha i}^* e^{-ip_i \cdot x} |\nu_i\rangle, \quad (1.16)$$

where  $p_i \cdot x = E_i t - \mathbf{p}_i \cdot \mathbf{x}$ . If we assume that the neutrino is relativistic, then  $t = x = L$ , after

### 1.3. Neutrino Oscillations

travelling a distance  $L$  the wave function could be rewritten as

$$|\nu_\alpha(L)\rangle = \sum_{i=1}^3 U_{\alpha i}^* e^{-i\phi_i} |\nu_i\rangle, \quad (1.17)$$

where  $\phi_i = p_i \cdot x = E_i t - |p_i| L \approx (E_i - |p_i|)L$ . Simply we can approximately calculate the  $p_i$  as

$$p_i = \sqrt{E_i^2 - m_i^2} = E_i \sqrt{1 - \frac{m_i^2}{E_i^2}} = E_i (1 - \frac{m_i^2}{E_i^2})^{1/2} \approx E_i (1 - \frac{m_i^2}{2E_i^2}). \quad (1.18)$$

So far

$$\phi_i = (E_i - |p_i|)L \approx \frac{m_i^2 L}{2E_i}. \quad (1.19)$$

By assuming  $\alpha, \beta, \gamma = e, \mu, \tau$  and  $i, j, k = 1, 2, 3$  we can determine the amplitude as

$$A(\nu_\alpha \rightarrow \nu_\beta) = \langle \nu_\beta | \nu_\alpha(t) \rangle, \quad (1.20)$$

and due the Equation 1.16 we have

$$A(\nu_\alpha \rightarrow \nu_\beta) = (\sum_{j=1}^3 U_{\beta j} \langle \nu_j |) (\sum_{i=1}^3 U_{\alpha i}^* e^{-i\phi_i} |\nu_i\rangle) = \sum_{i=1}^3 U_{\alpha i}^* U_{\beta i} e^{-i\phi_i}, \quad (1.21)$$

from which we can get the oscillation probability

$$P(\nu_\alpha \rightarrow \nu_\beta) = |\langle \nu_\beta | \nu_\alpha(t) \rangle|^2 = \left| \sum_{i=1}^3 U_{\alpha i}^* U_{\beta i} e^{-i\phi_i} \right|^2. \quad (1.22)$$

The terms in oscillation probability formula come from the diagram shown in Figure 1.3. By

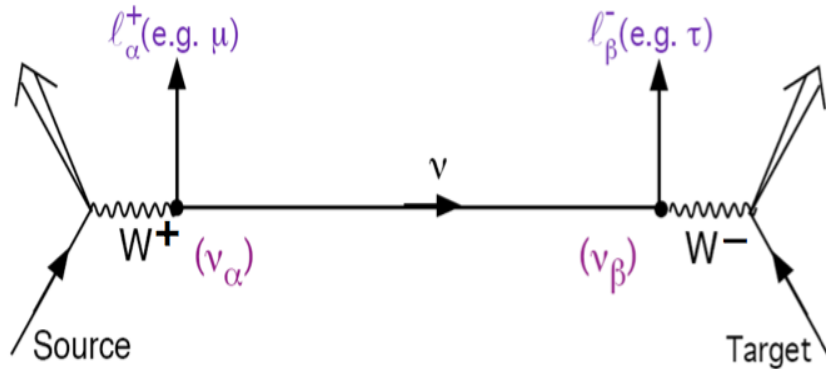


Figure 1.3 – The diagram for the terms in the three-neutrino oscillation probability [27].

## Chapter 1. Neutrino Oscillations

---

using the complex relation in the following equation

$$|a + b + c|^2 = |a|^2 + |b|^2 + |c|^2 + 2\Re(ab^* + ac^* + bc^*), \quad (1.23)$$

we can rewrite the oscillation probability as

$$P(\nu_\alpha \rightarrow \nu_\beta) = \sum_{i=1}^3 |U_{\alpha i}^* U_{\beta i}|^2 + 2 \sum_{i < j}^3 \operatorname{Re} [U_{\alpha i}^* U_{\beta i} U_{\alpha j} U_{\beta j}^* e^{i(\phi_j - \phi_i)t}]. \quad (1.24)$$

Concerning the Equation 1.19

$$\phi_j - \phi_i = \frac{m_j^2 L}{2E_j} - \frac{m_i^2 L}{2E_i} = \frac{\Delta m_{ij}^2 L}{2E} \quad (1.25)$$

where  $\Delta m_{ij}^2 = m_j^2 - m_i^2$  and  $E_i = E_j = E$ . Due to  $e^{i\theta} = \cos\theta + i\sin\theta$  we can write

$$\begin{aligned} P(\nu_\alpha \rightarrow \nu_\beta) &= \sum_{i=1}^3 |U_{\alpha i}^* U_{\beta i}|^2 + 2 \sum_{i < j}^3 \operatorname{Re} (U_{\alpha i}^* U_{\beta i} U_{\alpha j} U_{\beta j}^*) \cos \frac{\Delta m_{ji}^2 L}{2E} \\ &\quad + 2 \sum_{i < j}^3 \operatorname{Im} (U_{\alpha i}^* U_{\beta i} U_{\alpha j} U_{\beta j}^*) \sin \frac{\Delta m_{ji}^2 L}{2E} \\ &= \sum_{i=1}^3 |U_{\alpha i}^* U_{\beta i}|^2 + 2 \sum_{i < j}^3 \operatorname{Re} (U_{\alpha i}^* U_{\beta i} U_{\alpha j} U_{\beta j}^*) \\ &\quad - 4 \sum_{i < j}^3 \operatorname{Re} (U_{\alpha i}^* U_{\beta i} U_{\alpha j} U_{\beta j}^*) \sin^2 \frac{\Delta m_{ji}^2 L}{4E} + 2 \sum_{i < j}^3 \operatorname{Im} (U_{\alpha i}^* U_{\beta i} U_{\alpha j} U_{\beta j}^*) \sin \frac{\Delta m_{ji}^2 L}{2E} \\ &= \sum_{i=1}^3 |U_{\alpha i}^* U_{\beta i}|^2 - 4 \sum_{i < j}^3 \operatorname{Re} (U_{\alpha i}^* U_{\beta i} U_{\alpha j} U_{\beta j}^*) \sin^2 \frac{\Delta m_{ji}^2 L}{4E} \\ &\quad + 2 \sum_{i < j}^3 \operatorname{Im} (U_{\alpha i}^* U_{\beta i} U_{\alpha j} U_{\beta j}^*) \sin \frac{\Delta m_{ji}^2 L}{2E}. \end{aligned} \quad (1.26)$$

By knowing that  $\sum_{i=1}^3 |U_{\alpha i}^* U_{\beta i}|^2 = \delta_{\alpha\beta}$  the final formula for the three neutrino flavor oscillation probability could be written as

$$\begin{aligned} P(\nu_\alpha \rightarrow \nu_\beta) &= \delta_{\alpha\beta} - 4 \sum_{i < j}^3 \operatorname{Re} (U_{\alpha i}^* U_{\beta i} U_{\alpha j} U_{\beta j}^*) \sin^2 \frac{\Delta m_{ji}^2 L}{4E} \\ &\quad + 2 \sum_{i < j}^3 \operatorname{Im} (U_{\alpha i}^* U_{\beta i} U_{\alpha j} U_{\beta j}^*) \sin \frac{\Delta m_{ji}^2 L}{2E}. \end{aligned} \quad (1.27)$$

The unitary matrix  $U$  can be built as a product of 3 unitary rotation matrices including complex

phases:

$$O_1(\theta_1, \alpha_1, \beta_1, \gamma_1) = \begin{pmatrix} c_1 e^{i\alpha_1} & s_1 e^{-i\beta_1} & 0 \\ -s_1 e^{i\beta_1} & c_1 e^{i\alpha_1} & 0 \\ 0 & 0 & e^{i\gamma_1} \end{pmatrix}, \quad (1.28)$$

$$O_2(\theta_2, \alpha_2, \beta_2, \gamma_2) = \begin{pmatrix} e^{i\gamma_2} & 0 & 0 \\ 0 & c_2 e^{i\alpha_2} & s_2 e^{-i\beta_2} \\ 0 & -s_2 e^{i\beta_2} & c_2 e^{-i\alpha_2} \end{pmatrix}, \quad (1.29)$$

$$O_3(\theta_3, \alpha_3, \beta_3, \gamma_3) = \begin{pmatrix} c_3 e^{i\alpha_3} & 0 & s_3 e^{-i\beta_3} \\ 0 & e^{i\gamma_3} & 0 \\ -s_3 e^{i\beta_3} & 0 & c_3 e^{-i\alpha_3} \end{pmatrix}. \quad (1.30)$$

Where  $c_i \equiv \cos \theta_i$  and  $s_i \equiv \sin \theta_i$  for  $i = 1, 2, 3$ . The standard parameterization for the matrix U is

$$U = \begin{pmatrix} e^{i\gamma_2} & 0 & 0 \\ 0 & c_2 e^{i\alpha_2} & s_2 e^{-i\beta_2} \\ 0 & -s_2 e^{i\beta_2} & c_2 e^{-i\alpha_2} \end{pmatrix} \begin{pmatrix} c_3 e^{i\alpha_3} & 0 & s_3 e^{-i\beta_3} \\ 0 & e^{i\gamma_3} & 0 \\ -s_3 e^{i\beta_3} & 0 & c_3 e^{-i\alpha_3} \end{pmatrix} \begin{pmatrix} c_1 e^{i\alpha_1} & s_1 e^{-i\beta_1} & 0 \\ -s_1 e^{i\beta_1} & c_1 e^{i\alpha_1} & 0 \\ 0 & 0 & e^{i\gamma_1} \end{pmatrix}. \quad (1.31)$$

By multiplying these matrices the matrix U will be as

$$\begin{pmatrix} c_1 c_3 e^{i(\alpha_1 + \gamma_2 + \alpha_3)} & s_1 c_3 e^{i(-\beta_1 + \gamma_2 + \alpha_3)} & s_3 e^{i(\gamma_1 + \gamma_2 - \beta_3)} \\ -s_1 c_2 e^{i(\beta_1 + \alpha_2 + \gamma_3)} - c_1 s_2 s_3 e^{i(\alpha_1 - \beta_2 + \beta_3)} & c_1 c_2 e^{i(-\alpha_1 + \alpha_2 + \gamma_3)} - s_1 s_2 s_3 e^{i(-\beta_1 - \beta_2 + \beta_3)} & s_2 c_3 e^{i(\gamma_1 - \beta_2 - \alpha_3)} \\ s_1 s_2 e^{i(\beta_1 + \beta_2 + \gamma_3)} - c_1 c_2 s_3 e^{i(\alpha_1 - \alpha_2 + \beta_3)} & -c_1 s_2 e^{i(-\alpha_1 + \beta_2 + \gamma_3)} - s_1 c_2 s_3 e^{i(\beta_1 - \alpha_2 + \beta_3)} & c_2 c_3 e^{i(\gamma_1 - \alpha_2 - \alpha_3)} \end{pmatrix}. \quad (1.32)$$

To simplify the Equation 1.32, let's define some new variables as below

$$\begin{aligned} a &= (\alpha_1 - \beta_1) - (\alpha_2 + \beta_2 - \gamma_2) - \gamma_3 \\ b &= -\beta_2 - \alpha_2 \\ c &= -\alpha_2 - \alpha_3 \\ d &= \beta_1 + (\alpha_2 + \beta_2) + (\alpha_3 + \gamma_3) \\ e &= -\alpha_1 + (\alpha_2 + \beta_2) + (\alpha_3 + \gamma_3) \\ f &= \gamma_1. \end{aligned} \quad (1.33)$$

So

$$U = \begin{pmatrix} e^{ia} & 0 & 0 \\ 0 & e^{ib} & 0 \\ 0 & 0 & e^{ic} \end{pmatrix} \begin{pmatrix} c_1 c_3 & s_1 c_3 & s_3 e^{-i\delta} \\ -s_1 c_2 - c_1 s_2 s_3 e^{i\delta} & c_1 c_2 - s_1 s_2 s_3 e^{i\delta} & s_2 c_3 \\ s_1 s_2 - c_1 c_2 s_3 e^{i\delta} & -c_1 s_2 - s_1 c_2 s_3 e^{i\delta} & c_2 c_3 \end{pmatrix} \begin{pmatrix} e^{id} & 0 & 0 \\ 0 & e^{ie} & 0 \\ 0 & 0 & e^{if} \end{pmatrix}.$$

(1.34)

If neutrinos are Majorana particles, then the left-handed and the right-handed neutrino fields are correlated. Therefore, only a common phase of three left-handed neutrino fields can be redetermined (e.g.,  $f = 0$ ). Then

$$U = \begin{pmatrix} c_{12}c_{13} & s_{12}c_{13} & s_{13}e^{-i\delta} \\ -s_{12}c_{23} - c_{12}s_{23}s_{13}e^{i\delta} & c_{12}c_{23} - s_{12}s_{23}s_{13}e^{i\delta} & s_{23}c_{13} \\ s_{12}s_{23} - c_{12}c_{23}s_{13}e^{i\delta} & -c_{12}s_{23} - s_{12}c_{23}s_{13}e^{i\delta} & c_{23}c_{13} \end{pmatrix} \begin{pmatrix} e^{i\rho} & 0 & 0 \\ 0 & e^{i\sigma} & 0 \\ 0 & 0 & 1 \end{pmatrix}, \quad (1.35)$$

where  $c_{ij} = \cos\theta_{ij}$  and  $s_{ij} = \sin\theta_{ij}$ . But if we consider that the neutrinos are Dirac particles, the neutrinos are different from their antiparticles and the phases can be removed from the unitary matrix. Then the neutrino-mixing matrix could be written as

$$U = \begin{pmatrix} c_{12}c_{13} & s_{12}c_{13} & s_{13}e^{-i\delta} \\ -s_{12}c_{23} - c_{12}s_{23}s_{13}e^{i\delta} & c_{12}c_{23} - s_{12}s_{23}s_{13}e^{i\delta} & s_{23}c_{13} \\ s_{12}s_{23} - c_{12}c_{23}s_{13}e^{i\delta} & -c_{12}s_{23} - s_{12}c_{23}s_{13}e^{i\delta} & c_{23}c_{13} \end{pmatrix}. \quad (1.36)$$

## 1.4 Mikheyev-Smirnov-Wolfenstein Effect

In this chapter till now we have assumed that neutrinos propagate in vacuum freely from the source to the detector. But in many conditions, this is not the case. So, the question will be, is the matter important for neutrinos?

First Wolfenstein and later Mikheyev and Smirnov figured out that the neutrino oscillation probabilities could be strongly affected by the presence of matter. When neutrinos travel through matter, their coherent forward scattering from particles along their way, can affect their propagation [28].

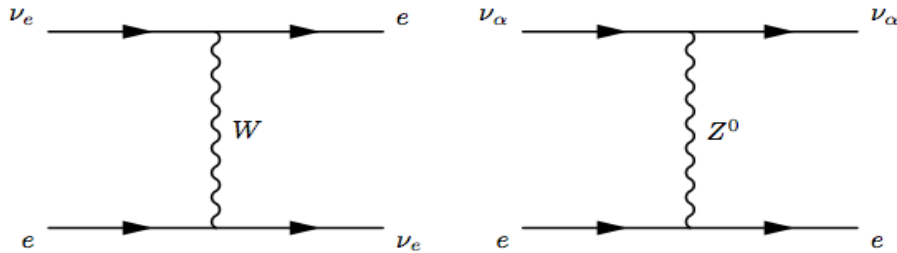


Figure 1.4 – Coherent forward scattering diagrams for neutrinos going through matter [29].

This progress could be either via a Charged Current (CC) or Neutral Current (NC) reaction as it's shown in Figure 1.4. The charged current process can only occur for electron neutrinos. However, neutral current scattering affects all flavors  $\nu_\alpha$  equally. Therefore, the MSW effect [30] is an additional potential in the Hamiltonian that depends on the density of the matter

## 1.5. Neutrino Oscillation Experiments

---

traveled by the neutrinos. For example for  $\nu_e$ , there is an additional potential from W exchange induced  $\nu_e$  forward scattering due to the ambient matter

$$V = \sqrt{2}G_F N_e, \quad (1.37)$$

where  $G_F$  is the Fermi coupling constant and  $N_e$  stands for the electron density. So, for the neutrino oscillation in the matter we can write

$$i \frac{d}{dt} \begin{pmatrix} \nu_e \\ \nu_\mu \end{pmatrix} = \begin{pmatrix} -\frac{\Delta m^2}{4E} \cos 2\theta + \sqrt{2}G_F N_e & \frac{\Delta m^2}{4E} \sin 2\theta \\ \frac{\Delta m^2}{4E} \sin 2\theta & \frac{\Delta m^2}{4E} \cos 2\theta \end{pmatrix} \begin{pmatrix} \nu_e \\ \nu_\mu \end{pmatrix}. \quad (1.38)$$

In some experimental condition only two flavors take part to the oscillation. In these cases, it is easy to show that the formulas for the oscillation probabilities of the previous section reduce to

$$P(\nu_e \rightarrow \nu_\mu)_v = \sin^2 2\theta \sin^2 \left( \frac{1.27 \Delta m^2 L}{E} \right), \quad (1.39)$$

and so far we can write the neutrino oscillation probability in matter as

$$P(\nu_e \rightarrow \nu_\mu)_M = \sin^2 2\theta_M \sin^2 \left( \frac{1.27 \Delta m_M^2 L}{E} \right), \quad (1.40)$$

where

$$\Delta m_M^2 = \sqrt{(\Delta m^2 \cos 2\theta - 2\sqrt{2}G_F E N_e)^2 + (\Delta m^2 \sin 2\theta)^2}, \quad (1.41)$$

and

$$\sin^2 2\theta_M = \frac{\left( \frac{\Delta m^2}{2E} \right)^2 \sin^2 2\theta}{\left( \frac{\Delta m^2}{2E} \right)^2 \sin^2 2\theta + \left( \frac{\Delta m^2}{2E} \cos 2\theta - \sqrt{2}G_F N_e \right)^2}. \quad (1.42)$$

That means due to the MSW effect, neutrinos can pass through a medium with critical density. Therefore, the resonant condition might be fulfilled even for a very small mixing angle,  $\theta$ , in vacuum. In Equation 1.42 the MSW resonance appears when

$$\frac{\Delta m^2}{2E} \cos 2\theta = \sqrt{2}G_F N_e. \quad (1.43)$$

## 1.5 Neutrino Oscillation Experiments

Depending on the neutrino sources the neutrino oscillation experiments could be categorized in three groups: solar neutrino experiments, atmospheric neutrino experiments and reactor experiments. Neutrino oscillation experiments can be also categorized depending on their

appearance or disappearance detection mode. Appearance mode experiments are those measuring the transitions between one neutrino flavor to other neutrino flavors. However, in disappearance mode experiments the survival probability of a neutrino flavor could be measured by comparing the expected number of interactions with the actual number of interactions in the detector.

Historically, depending on the particular study about neutrinos different neutrino experiments have been done over the years by using the different detector technologies. A neutrino experiment could include some of the following: low energy threshold to study the low-energy neutrinos (for solar neutrinos); good particle identification to detect the electrons and muons in neutrino studies and good energy measurement (for oscillation experiments); good angular resolution for astrophysical neutrinos; good time resolution (for supernova neutrinos); and charge identification. Obviously, only one experiment cannot explain all of these things. Neutrino physicists, according to their aim, will select the most suitable technology in their particular experiment.

### 1.5.1 Solar Neutrinos

The nuclear fusion process in the core of the Sun produces solar neutrinos. In this process, neutrinos are produced exclusively with electron flavor in a wide energy spectrum. Their investigations are provided by different solar neutrino experiments, where as shown in Figure 1.5, each of them is designed to investigate a specific energy range.

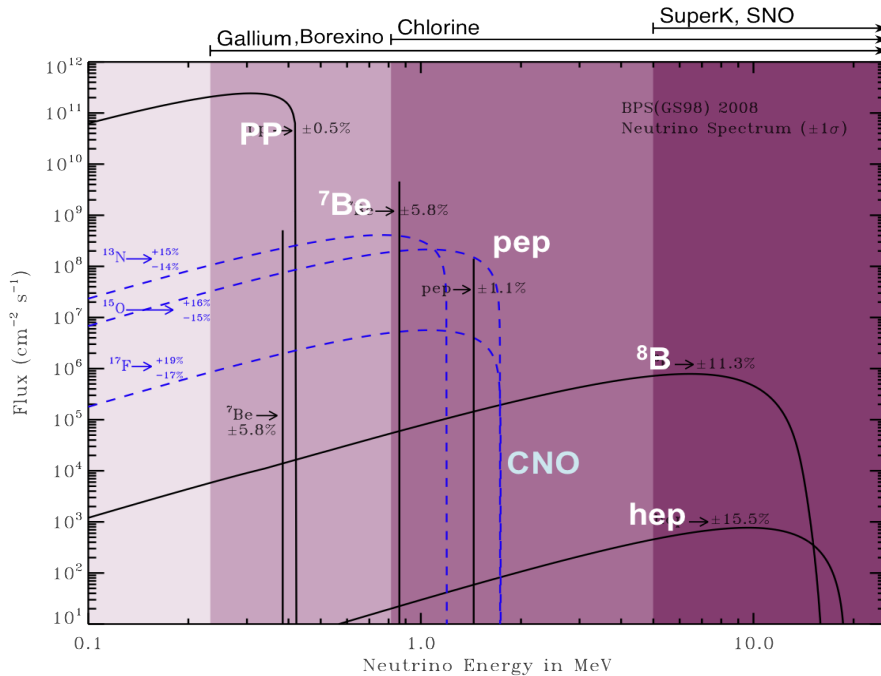


Figure 1.5 – Solar neutrino flux from different reactions at the Earth's surface, together with the energy thresholds of the experiments performed so far [31].

## 1.5. Neutrino Oscillation Experiments

---

In 1968, Davis and his colleagues announced the first result on detection of solar neutrinos at Homestake experiment in the United States, a long series of 'radiochemical' experiments.

Radiochemical experiments [32, 33] provide the lowest energy thresholds in which, through the inverse beta decay, a neutrino is caught by an element that is converted to another element (a charged-current interaction). An example for radiochemical experiments is the chlorine solar neutrino experiment, the reaction  $\nu_e + {}^{37}Cl \rightarrow {}^{37}Ar + e$  [34]. By using the gallium instead of chlorine as a target,  $\nu_e + {}^{71}Ga \rightarrow {}^{71}Ge + e$  [35], even lower thresholds of 0.233 MeV could be achieved. The produced isotope will decay back to the original element because it is unstable.

In radiochemical experiments, there is a tank with a target element inside that usually a compound such as perchloro-ethylene ( $Cl_2Cl_4$ ) or gallium-trichloride ( $GaCl_3$ ). By exposing the target element for a while the daughter element can be extracted from the tank, and therefore the number of radioactive decays will be counted. But there are three problems for radiochemical experiments: they cannot measure the energy, they are not sensitive to direction and their time resolution is very poor.

Several experiments like Homestake using chlorine as a target element; GALLEX/GNO [36] using gallium; and also the SAGE [37] experiment using a pure liquid gallium were carried on for the detection of solar neutrinos flux.

However the HOMESTAKE [38] experiment was the first experiment that detected the solar neutrinos, but there was a problem: the detected solar neutrinos in HOMESTAKE experiment had a rate smaller, around 30%, than the expected rate of the Standard Solar Model (SSM) [39]. This problem was known as solar neutrino problem (SNP) [40]. At that time it was seemed that a solution could be the  $\nu_e$  oscillation. This deficit observed by HOMESTAKE was later proved by GALLEX experiment in Italy and by the SAGE gallium experiment in Russia. It seemed likely that the source of the solar neutrino problem was the behavior of the neutrino, and in the other word in neutrino oscillations. Even if there was no incontrovertible evidence, still it could be shown that there was a deficit of  $\nu_e$ , however it could not be proven that they had oscillated into some other type of neutrino. Therefore, it was necessary to have a detector that is able to directly compare the CC and NC interaction rates, having the energies in order of 1 MeV.

In 1984, Herb Chen thought that maybe using the heavy water would be a solution to this problem. The molecule of heavy water,  $D_2O$ , is made by two deuterium (the heavier isotope of normal hydrogen whose its nucleus contains a neutron in addition to the proton) and an oxygen. Deuterium is extremely unstable and it can easily broken up; this process can appear in two different ways

$$\nu + D \rightarrow p + p + e^- \quad (\text{CC}) \quad [41], \quad (1.44)$$

## Chapter 1. Neutrino Oscillations

---

which incoming neutrino can be only electron-neutrino;

$$\nu + D \rightarrow p + n + \nu \quad (\text{NC}) \quad [42], \quad (1.45)$$

however for neutral interaction case, incoming neutrino can be any flavor of neutrino. This results provided by researchers from Sudbury Neutrino Observatory (SNO) in Canada [43]. The SNO data show the solar neutrinos deficit is due to the oscillation of electron neutrinos into  $\nu_\mu$  and  $\nu_\tau$  that were below the energy threshold to produce charged current interactions. In this picture, the validity of SSM is preserved.

Also the KamLAND [44] experiment in Japan, perceived the disappearance of  $\bar{\nu}_e$  by using the neutrinos coming from nuclear reactors. These results were a confirmation of the oscillation solution for the solar neutrino problem.

A combined analysis of KamLAND and SNO results with other solar experiment data, in particular the one collected in the SuperKamiokande [45] experiment, is summarized by Figure 1.6, which shows that [46]

$$\Delta m_{12}^2 = 7.92(1 \pm 0.09) \times 10^{-5} \text{ eV}^2, \quad (1.46)$$

$$\sin^2 \theta_{12} = 0.314^{+0.18}_{-0.15}. \quad (1.47)$$

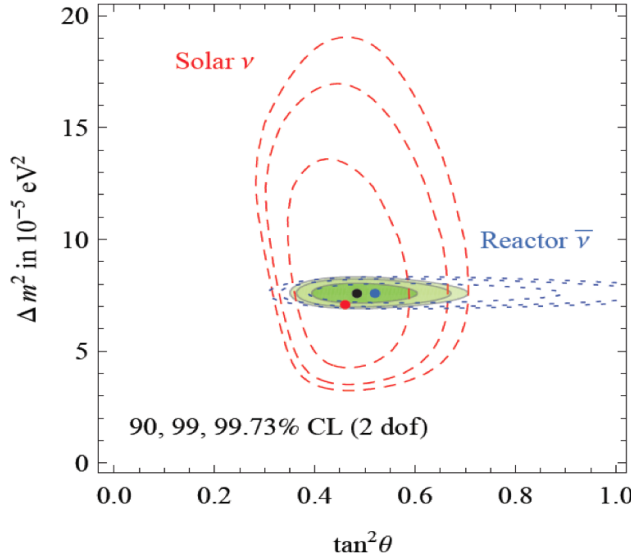


Figure 1.6 – Best fit regions at 90, 99 and 99.73 % C.L. obtained fitting solar neutrino data (red dashed contours); reactor antineutrino data (blue dotted contours); all data (shaded region) [47].

### 1.5.2 Atmospheric Neutrino Experiments

Atmospheric neutrinos are produced in the interactions of cosmic rays with the nuclei of the Earth's atmosphere and coming from the decay of secondary particles, mostly pions and kaons, into muons and muon neutrinos, shown in Figure 1.7. Their average energy is in GeV/nucleon energy region, thus resulting much more higher than the one associated to solar neutrinos [48, 49].

A possible detection of atmospheric neutrinos is performed by underground detectors that receive a flux of neutrinos from all the directions that should be necessarily symmetric with respect to the vertical axis, see Figure 1.7. The neutrinos forming this flux can be divided in upward and downward neutrinos.

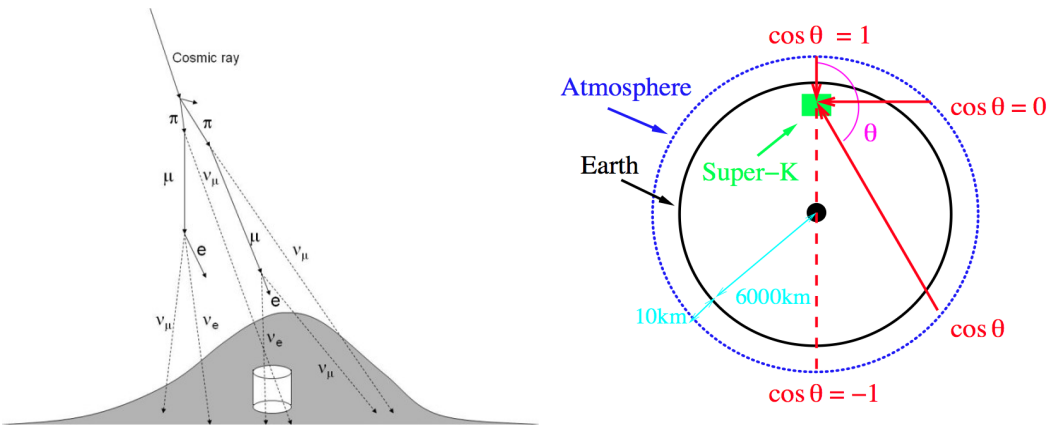


Figure 1.7 – Left: Atmospheric neutrinos produced in Earth's atmosphere, Right: A sketch showing the relation between zenith angle and the distance travelled by atmospheric neutrinos.

First observations of atmospheric neutrinos occurred in the 1960s, by two deep underground experiments performed at the Kolar Gold Field Mine, in South India [50], and at the East Rand Proprietary Gold Mine, South Africa [51]. In the early 1980s proton decay experiments detected the first completely contained atmospheric neutrino interactions where their all-visible secondary particles were stopped in the detector.

A first signal of an atmospheric neutrino anomaly was found by the measurements coming from Kamiokande experiment in 1988 [52]. Kamiokande detector was found the muon-like events resulted a fraction of  $0.59 \pm 0.07$  respect to Monte Carlo predictions while the results for electron-like events were in agreement with Monte Carlo predictions. This anomaly is well described by the disappearance of  $\nu_\mu$  due to neutrino oscillations [53].

Another anomaly compatible with the Kamiokande data, resulted from the Irvine Michigan Brookhaven (IMB) [54] detector in the USA, a  $24 \times 18 \times 19 \text{ m}^3$  tank filled with about 8 kton of water. In particular, the neutrino deficit was found only in the contained events with energy below 1.5 GeV.

## Chapter 1. Neutrino Oscillations

---

Eventually the anomaly could be confirmed and explained when the Super-Kamiokande collaboration published their result in 1998 [55]. The Super-Kamiokande detector is capable to measure and determine the direction of solar neutrinos. It is also true for atmospheric neutrinos. This gives the possibility of measuring the number of neutrinos as a function of an angle made by their direction and the axis perpendicular to the Earth's surface (zenith angle).

Since the production of atmospheric neutrinos is isotropic, the number of downward-going neutrinos must be equal to the number of upward-going. Therefore, if there is no any effect like oscillation, one expects

$$N_l(\cos\theta) = N_l(-\cos\theta), \quad (1.48)$$

where  $\theta$  is zenith angle, see Figure 1.7. Downward-going neutrinos only travel around 15 km; while, upward-going neutrinos cross the whole Earth to reach the detector. The events in the SK detector are divided into two categories according to their energy: "sub-GeV" ( $E < 1.33$  GeV) and "multi-GeV" ( $E > 1.33$  GeV). So far, Super-Kamiokande data are best reproduced by the Monte Carlo, taking into account the oscillation effects. The oscillations are identified as a  $\nu_\mu \rightarrow \nu_\tau$  transition where other hypotheses like oscillating to sterile neutrinos or  $\nu_\mu \rightarrow \nu_e$  oscillations were strongly disfavored by the data, see Figure 1.8.

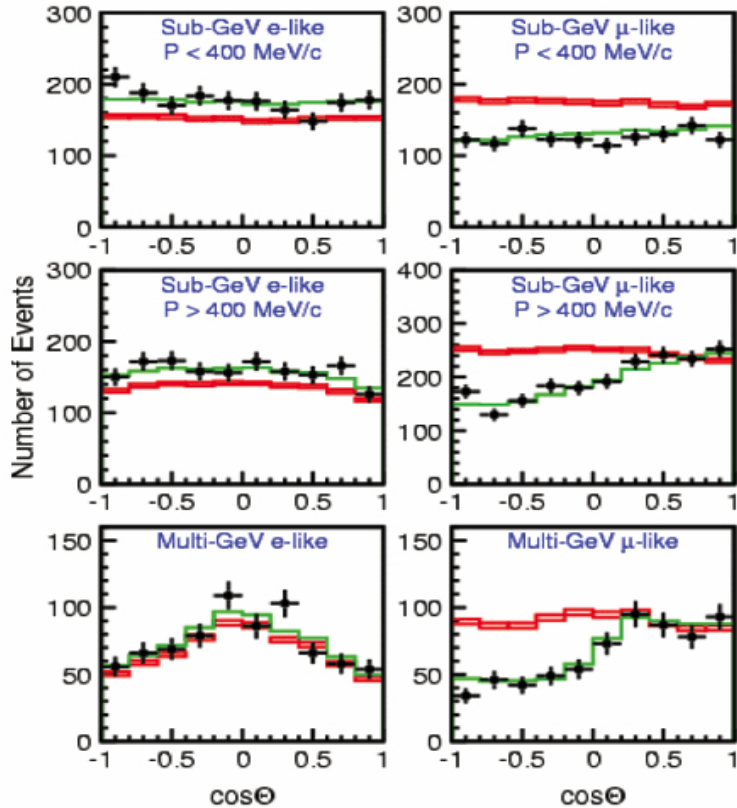


Figure 1.8 – Points with error bars: data; Red: Monte Carlo without oscillations; Green: Monte Carlo with best-fitted oscillation effects [56].

## 1.5. Neutrino Oscillation Experiments

---

The result can be also briefly given as a value of up-down asymmetry [55]:

$$A_{\mu}^{up-down} = -0.296 \pm 0.048 \pm 0.01, \quad (1.49)$$

$$A_e^{up-down} = -0.036 \pm 0.067 \pm 0.02. \quad (1.50)$$

This was considered as  $6\sigma$  model-independent evidence that a fraction of the upward-going atmospheric  $\nu_{\mu}$  flux disappears, where the asymmetry for electron neutrinos is consistent with 0. Moreover, a ratio of the data to Monte Carlo as a function of L/E [57] is shown in Figure 1.9.

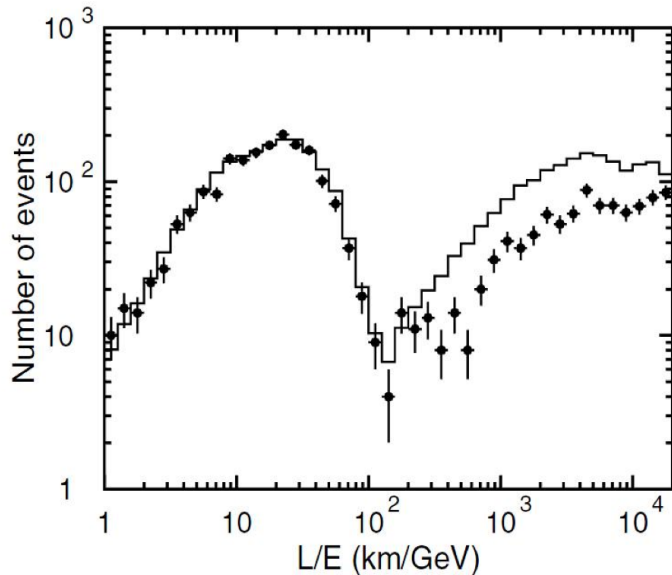


Figure 1.9 – Number of muon-like events in Super-Kamiokande as a function of L/E (points). The histogram shows the Monte Carlo prediction without oscillations [58].

Atmospheric data support maximal mixing, with the following oscillation parameters [46]:

$$\sin^2 \theta_{23} = 0.44(1^{+0.41}_{-0.22}). \quad (1.51)$$

$$\Delta m_{23}^2 = 2.4(1^{+0.21}_{-0.26}) \times 10^{-3} \text{ eV}^2, \quad (1.52)$$

### 1.5.3 Search for $\theta_{13}$

The long-baseline experiments tried to find the upper set limits for  $\theta_{13}$  through looking at  $\nu_\mu \rightarrow \nu_e$  oscillation. However, recently the best upper limit for  $\theta_{13}$  is measured in the CHOOZ [59] experiment where is a short baseline experiment. In this experiment, a scintillator detector is located underground,  $\sim 1$  km far from the nuclear reactor core to measure the electron antineutrinos that is produced at a nuclear power plant in France.

The new generations of experiments to measure  $\theta_{13}$  are categorized in two different kinds:

- The experiments that measure the disappearance of  $\bar{\nu}_e$  from the produced antielectron neutrinos in reactors, like Double-CHOOZ [60], RENO [61] and Daya Bay [62].
- The experiments that measure the appearance of electron neutrinos at  $\nu_\mu \rightarrow \nu_e$  oscillations coming from a  $\nu_\mu$  beam generated in an accelerator complex, such as T2K [63] and NOvA [64].

The T2K collaboration for the first time published a result of  $2.5\sigma$  from zero for  $\sin^2(2\theta_{13})$  in July 2011, where is a strong sign of the  $\theta_{13} \neq 0$ . In December of the same year the Double-CHOOZ collaboration announced their first results, as shown in Figure 1.10, that increases the difference of the  $\sin^2(2\theta_{13})$  value and zero up to about  $3\sigma$ , in comparing with results coming from T2K and MINOS [65] experiments.

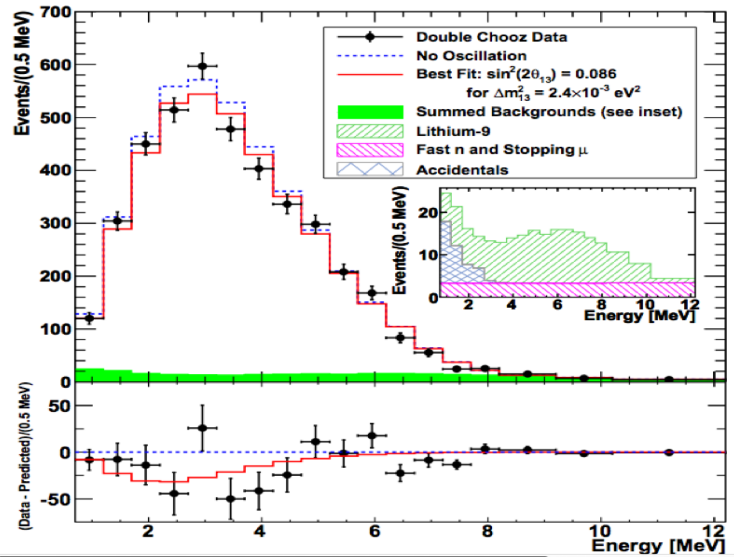


Figure 1.10 – Measured prompt energy spectrum of the far detector compared with the no oscillation (top) and their ratio (bottom) from the measurements of the two near detectors. Only statistical errors are shown [66].

By April 2012 Daya-Bay Collaboration performed a measurement of  $\sin^2(2\theta_{13}) = 0.089 \pm 0.010(\text{stat}) \pm 0.005(\text{syst})$  [67], see Figure 1.11, verifying a non-zero  $\theta_{13}$  at more than  $5\sigma$  level.

## 1.5. Neutrino Oscillation Experiments

After this result was published, the RENO collaboration measured the same angle by an inde-

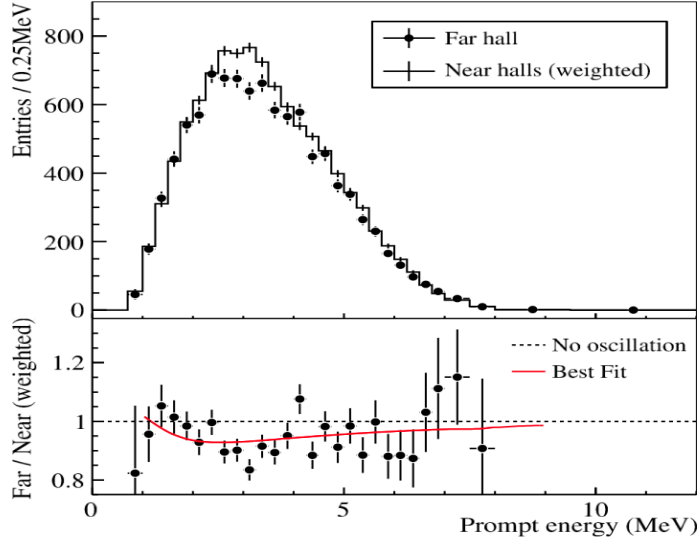


Figure 1.11 – Measured prompt energy spectrum in the Far hall compared to extrapolation of the Near halls detected flux assuming no oscillation (top) and their ratio (bottom). If there were no oscillation the Far/Near ratio should always be 1 (dashed line in the bottom plot). The red line shows the best  $\nu e$  disappearance fit. Only statistical errors are shown [68].

pendent measurement of  $\sin^2(2\theta_{13}) = 0.113 \pm 0.013(\text{stat}) \pm 0.019(\text{syst})$  [69] that is compatible with the result of Daya-Bay, see Figure 1.12.

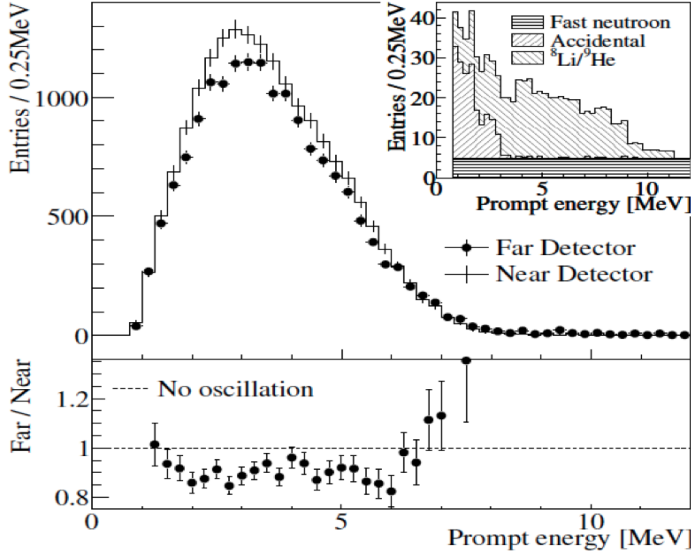


Figure 1.12 – The ratio of the measured spectrum of far detector to the no oscillation prediction [70].

### 1.5.4 Summary of neutrino oscillation parameters

Neutrino oscillation experiments measure the squared mass differences ( $\Delta m^2$ ) of neutrinos but not the absolute mass of them. Furthermore, the order of masses is not known yet, i.e. we don't know whether the masses are defined as normal hierarchy (NH),  $m_3 \gg m_2 > m_1$ , or inverted hierarchy (IH),  $m_3 \ll m_1 < m_2$ , see Figure 1.13. The best global fit results of neutrino oscillation parameters for NH and IH are summarized in Table 1.1.

Parameter	Hierarchy	$3\sigma$ range	Best fit
$\delta m^2/10^{-5} eV^2$	NH or IH	6.99–8.18	7.54
$\sin^2 \theta_{12}/10^{-1}$	NH or IH	2.59–3.59	3.07
$\Delta m^2/10^{-3} eV^2$	NH	2.19–2.62	2.43
$\Delta m^2/10^{-3} eV^2$	IH	2.17–2.61	2.42
$\sin^2 \theta_{13}/10^{-2}$	NH	1.69–3.13	2.41
$\sin^2 \theta_{13}/10^{-2}$	IH	1.71–3.15	2.44
$\sin^2 \theta_{23}/10^{-1}$	NH	3.31–6.37	3.86
$\sin^2 \theta_{23}/10^{-1}$	IH	3.35–6.63	3.92

Table 1.1 – Summary of best global fit of neutrino oscillation parameters, taken from [71].  $\Delta m^2$  is defined herein as  $m_3^2 - (m_1^2 + m_2^2)/2$ , with  $+\Delta m^2$  for NH and  $-\Delta m^2$  for IH.

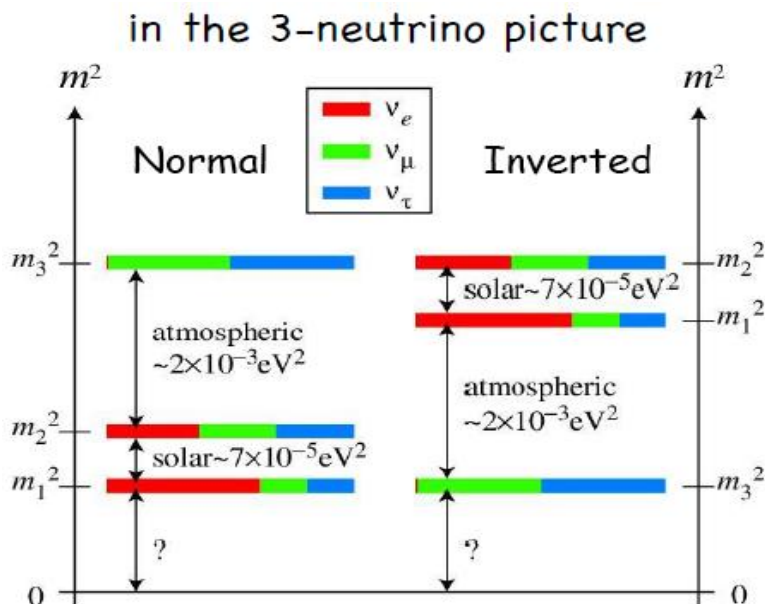


Figure 1.13 – Three neutrino  $\Delta m^2$  Pattern of squared neutrino mass and flavor components: Normal and inverted hierarchies [72].

Summarizing the present knowledge about neutrinos, we can state that [73]:

- The solar electron neutrinos produced inside the sun oscillate into muon and tau neutrinos;
- In the KamLand range of L/E,  $\nu_e \rightarrow \nu_\mu$  and  $\nu_\tau$  oscillations have been detected;
- In the atmospheric sector just pure  $\nu_\mu \rightarrow \nu_\tau$  oscillation has been detected; however no  $\nu_e \rightarrow \nu_\mu$  and  $\nu_\tau$  oscillations.

All the results in the form of allowed regions in oscillation parameter space are illustrated in Figure 1.14.

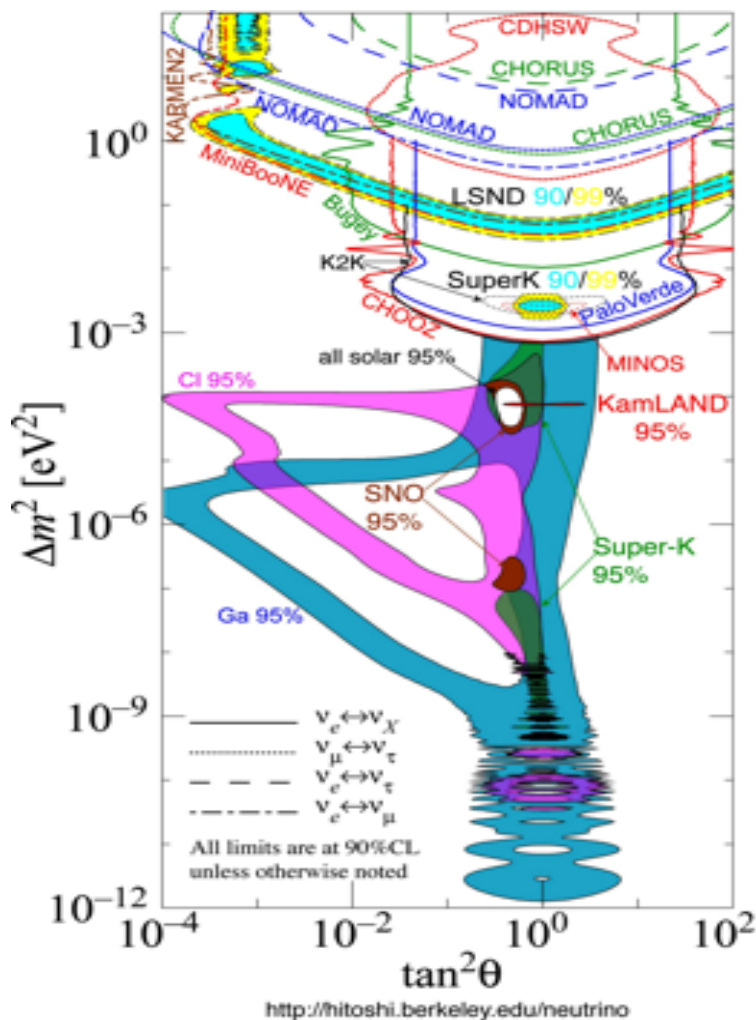


Figure 1.14 – Limits on oscillation parameters inferred from data of oscillation experiments. One can see the allowed region for atmospheric sector (upper-middle part, conjunction of Super-Kamiokande and K2K allowed regions) and for solar sector (middle part, SNO and KamLand). LSND and MiniBoone results in the upper part of the plot [74].



## 2 The OPERA Experiment

The disappearance of atmospheric muon neutrinos was assessed in the late 90's and then confirmed with artificial neutrino beams in the first years of this millennium. However, the direct detection of its oscillation through the appearance of a new neutrino flavor still is an important issue in the oscillation sector.

The OPERA experiment was designed, at Gran Sasso Laboratory (LNGS), to perform a conclusive prove of the  $\nu_\mu \rightarrow \nu_\tau$  oscillation hypothesis. Since it was triggered by the results of atmospheric neutrino experiments; the sensitivity of this experiment covers the  $\Delta m^2$  region allowed by atmospheric neutrino data [75]. The aim of OPERA is to detect the appearance of tau neutrinos in an almost pure beam of muon neutrinos.

The experimental setup and the physical performance of OPERA are described in this chapter.

### 2.1 The CNGS Neutrino Beam

The CNGS neutrino beam [76] was designed and optimized to observe tau neutrinos produced by  $\nu_\mu \rightarrow \nu_\tau$  oscillations [77]. CNGS beam is generated by a 400 GeV proton beam and has been extracted from the CERN SPS by hitting a target. The proton beam is transported through the transfer line TT41 to the target T40 [78]. The target is made of 13 graphite rods for a length of two meters, well encompassing the proton beam. The positively charged pions and kaons are energy-selected and directed towards Gran Sasso by using two focusing lenses, called "horn" and "reflector" as it's shown in Figure 2.1.

Most of the pions and kaons decay inside a long decay-pipe, 1000 meters length, and produce the  $\nu_\mu$ s and  $\mu$ s. An 18 meters hadron stopper, made of graphite and iron, is located downstream of decay-pipe in order to absorb the remaining hadrons, like produced protons or those pions and kaons that do not decay inside the decay-pipe. After the hadron stopper two sets of detectors are located to monitor the muons. While neutrinos continue traveling towards Gran Sasso, muons are absorbed in the rock after monitoring [79].

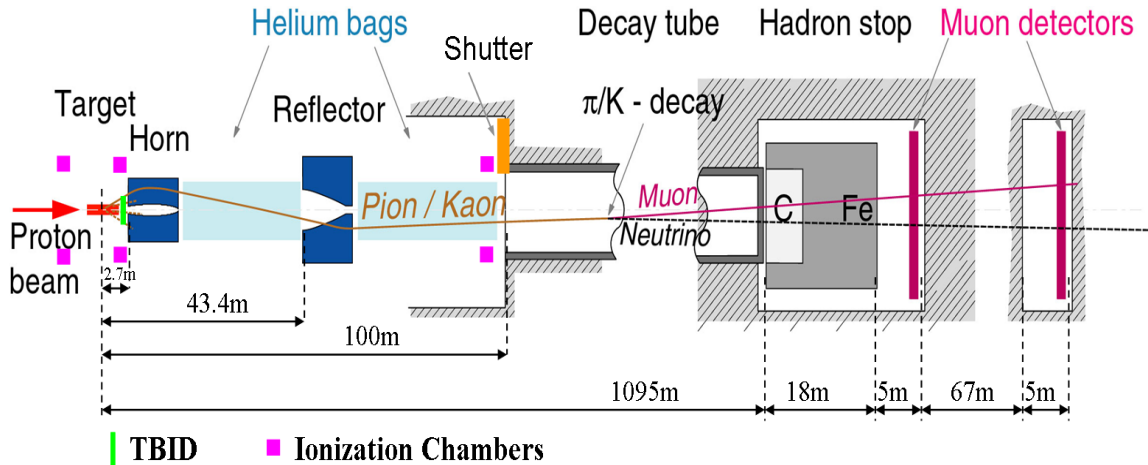


Figure 2.1 – Main components of the CNGS beam line [80].

The average energy of neutrinos arriving at the LNGS is around 17 GeV, see Figure 2.2, and the average ratio of  $\frac{L}{E_\nu}$  is 43 km  $GeV^{-1}$ . The energy was optimized to increase the probability of tau-neutrino interactions and so far increase the probability of detecting tau particles inside the detector.

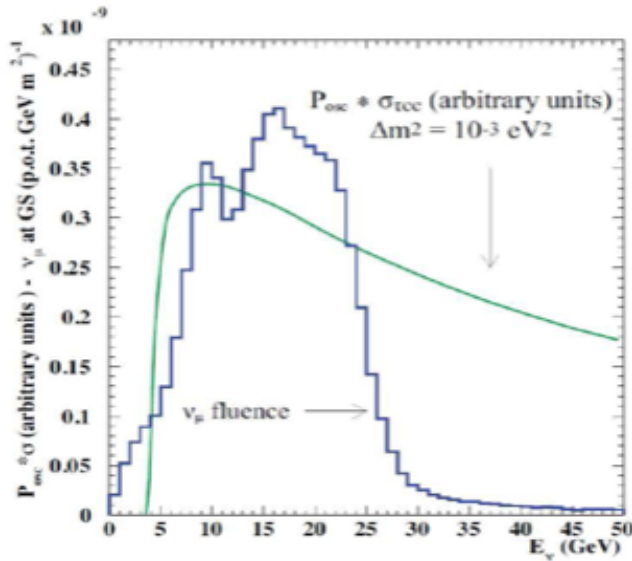


Figure 2.2 – The energy of CNGS beam spectrum and oscillation probability multiplied by the  $\nu_\tau$  cross section [81].

CNGS  $\nu_\mu$ -beam is slightly contaminated by other neutrino flavors where the contamination of  $\bar{\nu}_\mu$  interactions is around 2.1% and the contaminations of  $\nu_e$  and  $\bar{\nu}_e$  are in total around 1%.

## 2.1. The CNGS Neutrino Beam

The main features of the beam are summarized in Table 2.1.

L	730 km
$\langle E \rangle$	17 GeV
$L / \langle E_\nu \rangle$	43 km/GeV
$\bar{\nu}_\mu / \nu_\mu$	2.1 %
$\nu_e + \bar{\nu}_e / \nu_\mu$	0.87 %
$\nu_\tau$ prompt	negligible

Table 2.1 – CNGS beam features [75].

In addition, the low contamination of  $\nu_e (\bar{\nu}_e)$  allows searching for subleading  $\nu_\mu \rightarrow \nu_e$  oscillation looking for an excess of  $\nu_e$  charged-current (CC) interactions. The systematic error related with the  $\nu_e$  contamination has an important role for the  $\nu_\mu \rightarrow \nu_e$  oscillation search. This uncertainty depends on the knowledge of the kaons output. It can be assumed  $\sim 5\%$  systematic uncertainty on the overall  $\nu_e$  flux [82].

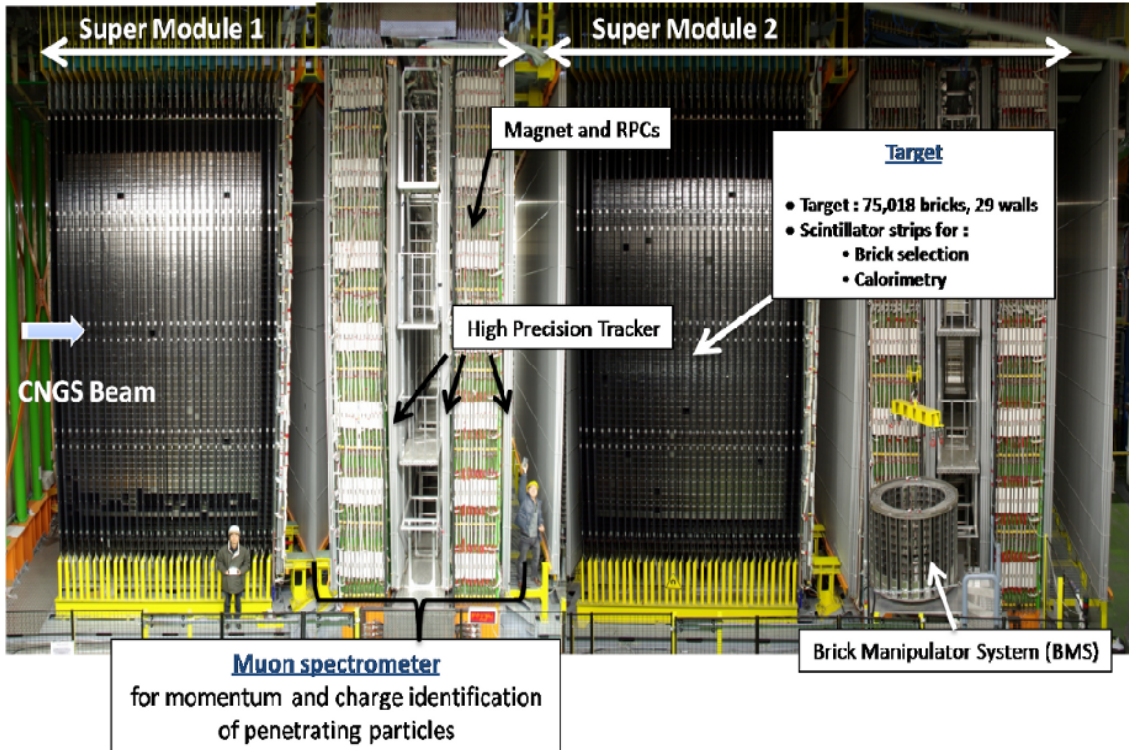


Figure 2.3 – Overview of the OPERA detector [83].

## 2.2 The OPERA Detector

The OPERA detector is a hybrid detector composed of two identical parts, so called super-modules (SM). Each super-module contains a target section and a magnetic spectrometer. The target is composed of 31 brick walls, transversal to the direction of beam, interleaved by 31 target tracker walls. A magnetic spectrometer is located downstream of the target section. It is a dipolar iron magnet equipped with Resistive Plate Chambers (RPC). The intensity of the magnetic field is 1.53 T, in the direction of vertical axis, shown in Figure 2.3. The OPERA detector dimensions are: 20 m in length and a cross section of  $10 \times 10 m^2$ , for a total weight of around 4 kton. OPERA is based on the Emulsion Cloud Chamber (ECC) technique, which provides a micrometric spatial resolution by using photographic emulsions.

## 2.3 Emulsion Target

The ECC, or so-called brick, is the basic unit of the OPERA target. ECC brick consists of 57 emulsion films interleaved by 56 lead plates, packed together in a box with transverse dimensions of  $10.2 \times 12.7 cm^2$  and thickness of  $\sim 7.5$  cm (corresponding to about  $10 X_0$ ) and a total weight of 8.3 kg [84, 85].

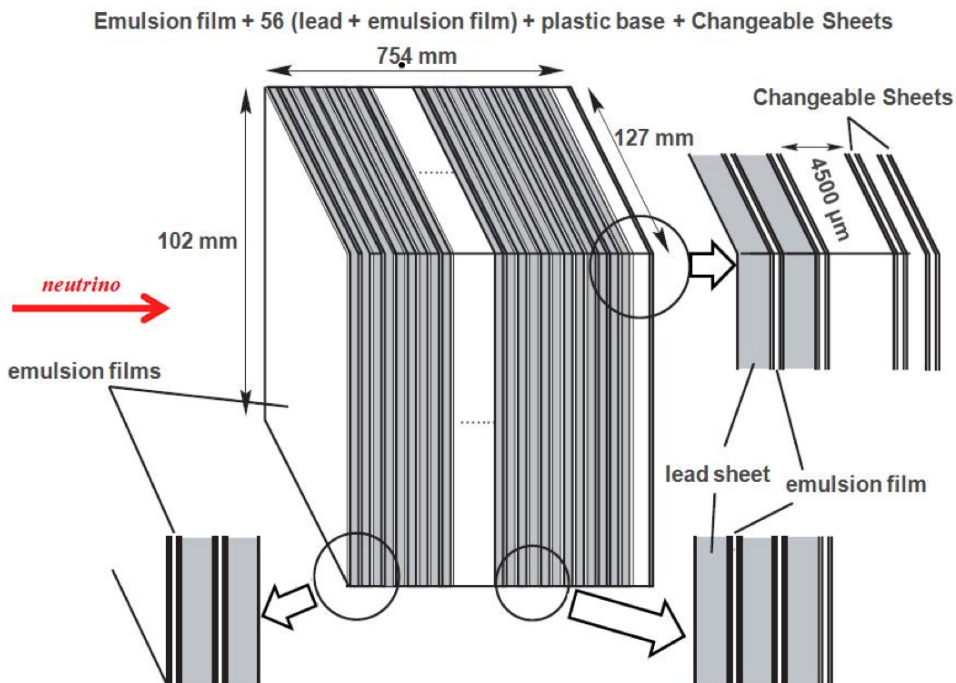


Figure 2.4 – Schematic structure of an ECC brick.

The size of bricks is designed by different requirements; for example the thickness of brick should be large enough to measure the momentum of hadrons through multiple Coulomb scattering method and also to identify and reconstruct the electron and its electromagnetic

(EM) shower. Multiple Coulomb scattering method for hadrons requires  $5-10 X_0$  and EM showers need  $6-7 X_0$ . Therefore, with  $10 X_0$  it is possible to do such measurements for half of the events within the same brick where the interaction took place, however for the other half it is needed to use also the information of their downstream brick.

## 2.4 Target Tracker

A Target Tracker (TT) wall follows each brick wall to provide time resolution to the emulsions. The TT is used to identify the brick where the neutrino interaction took place and in case of hadronic showers provide a calorimetric measurement of their energy. Target tracker is made up of two scintillator planes, each made of 256 plastic scintillator strips oriented along the X and Y-axis respectively, covering a total surface of  $6.7 \times 6.7 m^2$  defined by a brick wall. Each strip is 1.06 cm thick with a cross section of  $6.7 m \times 2.62$  cm. The scintillator strips of each plane are read out by optical fibers connected to a photomultiplier of 64 pixels, in a way that 8 photomultiplier are needed for each TT plane [86].

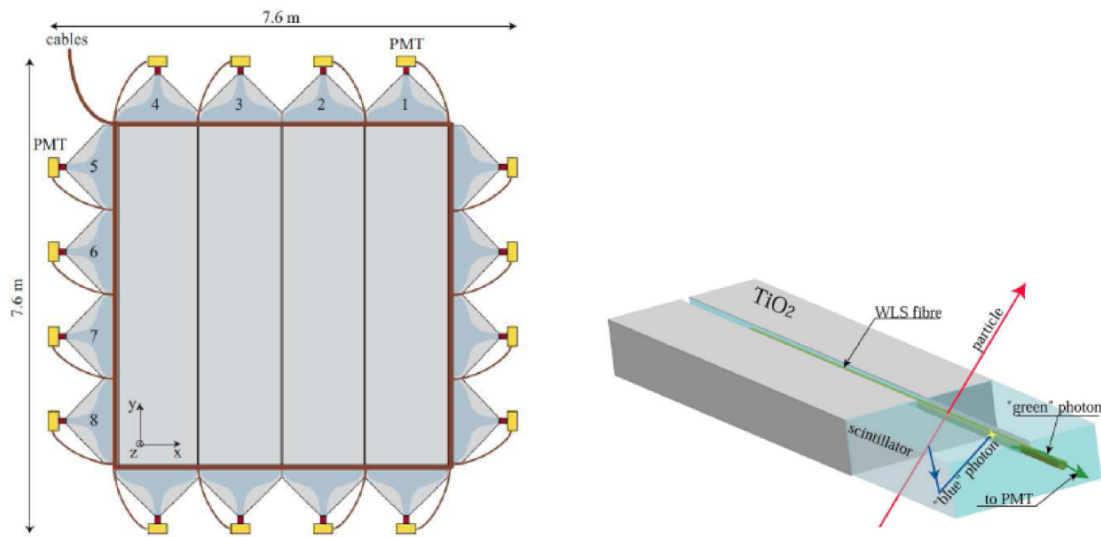


Figure 2.5 – Schematic view of the two scintillator planes of a TT wall on the left, and a scintillator strip with the wave length shifting fibers on the right [87, 88].

Before scanning the emulsion films to locate the neutrino interaction, the relevant region where films have to be analyzed is selected by the signals of the Target Tracker strips. In order to decrease the brick scanning, Changeable Sheets (CS) doublets [89] are used. CS doublets are a pair of nuclear emulsion films attached to the downstream side of each brick. They can be removed without opening the brick and be analyzed independently.

When there is a neutrino interaction inside the brick, the produced charged particles pass through the CS doublet and generate a trigger in the TT. After receiving the produced triggers

at TT, the brick is extracted and its CS doublet, after developing, is analyzed in the CS scanning laboratories at LNGS and Japan; if charged particles inside the CS are found in good agreement with TT triggers, the brick will be developed and analyzed in ECC scanning laboratories. The CS information is used for a precise prediction of the charged tracks position inside the brick in order to find and locate the neutrino vertex point.

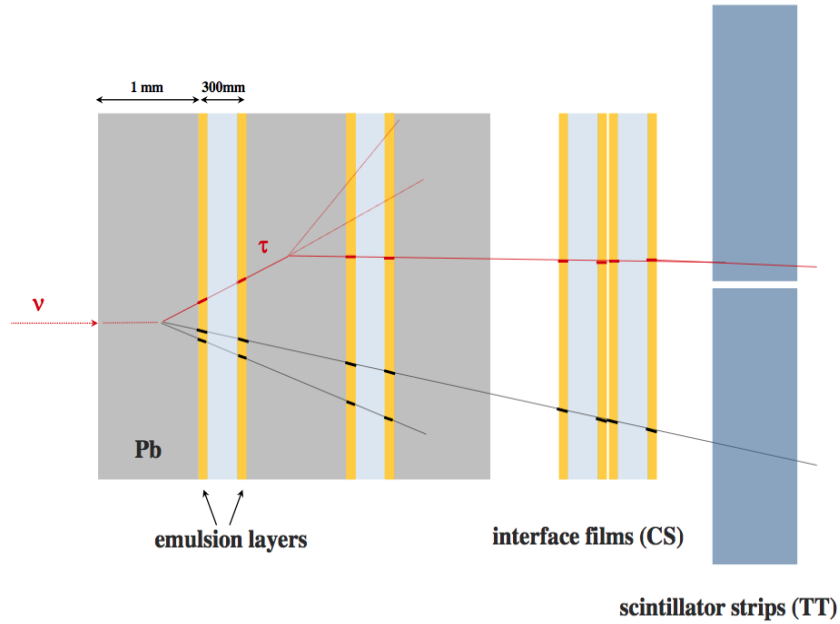


Figure 2.6 – Schematic view of a  $\nu_\tau$  CC interaction and the decay of its final state  $\tau$  lepton as it would appear inside the brick, in the CS emulsion films and in the TT strips [90].

## 2.5 Muon Spectrometers

A muon spectrometer [91] is located downstream of the target in each SM and is designed to identify muons and measure their momentum and charge. The spectrometer is made up of a dipolar magnet [92] that consists of two iron arms and has a magnetic field intensity of 1.53 T. In order to provide a gross tracking inside the magnet, Resistive Plates Chambers (RPCs) [93, 94] planes are placed between the iron planes of the arms.

Also six drift tubes are interleaved between the two arms to precisely measure the bending of the muon, see Figure 2.7. They constitute the High Precision Tracker (HPT) and are used, with the other parts of the muon spectrometer, to measure the momentum of muons and determine the sign of their charge. Two arms of the magnet with opposite magnetic field direction deflect muons.

RPCs are made up of electrode plates where each electrode plate consists of a 2 mm thick high resistivity plastic laminate painted with graphite to reconstruct the muon tracks inside the

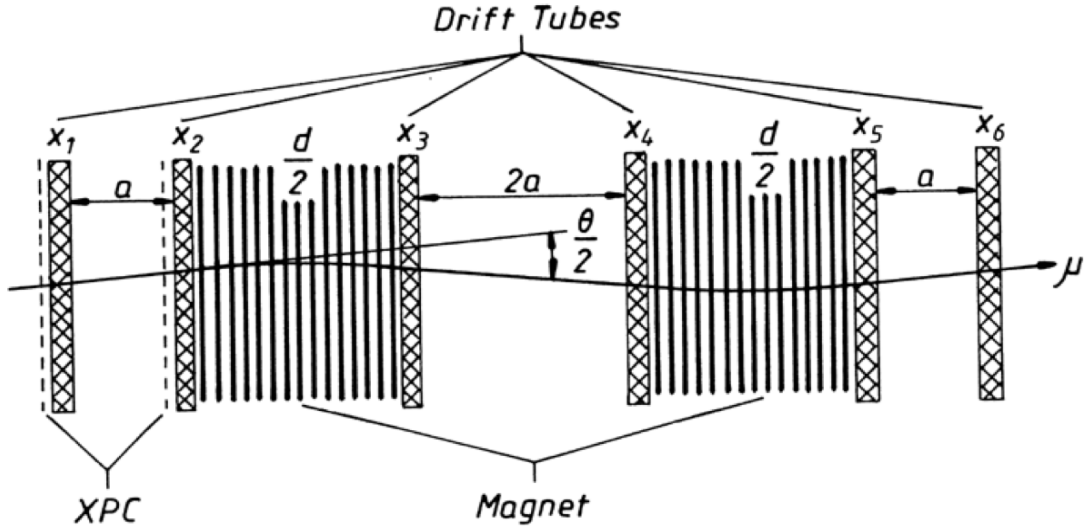


Figure 2.7 – Drift plane arrangement in the muon spectrometer. Also shown are two planes of RPC's with inclined strips (XPC's) [95].

spectrometer. Each of the two drift tube planes of the HPT, upstream of the dipole magnet, is accompanied by an RPC plane with two  $45^\circ$  crossed strip-layers called XPC to solve ambiguities in track spatial reconstruction. RPCs and XPCs aim is at giving an accurate trigger signal to the HPTs.

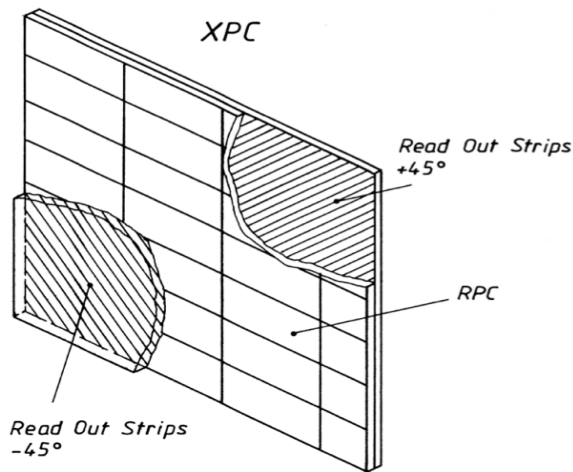


Figure 2.8 – Schematic view of a XPC detector plane [96].

## 2.6 VETO System

The CNGS beam also may interact in the rock before reaching the OPERA detector, during its travel to LNGS; therefore the secondary particles produced in this kind of events can enter the detector and generate false triggers. This signal may wrongly be associated with a brick and resulting in its extraction. For this reason a VETO system is located in front of the OPERA detector in order to reject this kind of events. The VETO consists of two glass RPC planes, where each RPC layer is made of 8 rows, each made of four units [97].

## 2.7 Automated Scanning System

In the OPERA experiment, the emulsion scanning is a quasi-online data processing. It is performed by fully automated scanning systems. There are two kinds of scanning systems: the S-UTS (Super-Ultra Track Selector) [98], developed in Japan and the ESS (European Scanning System) developed by a joint effort of several European laboratories. The ESS [99, 100] can work at a speed of  $20 \text{ cm}^2/\text{h}/\text{layer}$ .

The main components of the ESS microscope mentioned above, shown in Figure 2.9, are:

- A support table (MICOS), which has high quality mechanics.
- Computer driven horizontal and vertical stages.
- A granite arm as a supporting frame for CCD camera and objective.
- A mega-pixel CCD camera (CMOS with a resolution of  $1280 \times 1024$  pixels) mounted on the vertical plate on the granite arm. It is interfaced with a frame-grabber and vision processor.
- Optics and light system (NIKON) located below the scanning table.

The microscope is a Cartesian robot, holding the emulsion film on a horizontal stage (movable in X-Y coordinates). A CMOS camera mounted on the vertical optical axis (Z), along which it can be moved to vary the focal plane with a step equal to the focal depth of about  $3 \mu\text{m}$  (see Figure 2.9).

During the scanning, objective focuses at different depths of emulsion film and take tomographic images. In total 15 tomographic images are taken over  $44 \mu\text{m}$  thick emulsion layer while the camera is moving in the Z direction. These images are sent to Odyssey board for processing. The camera has a capability of working with a rate of 660 MB/s. In addition, OPERA uses the frame rate of 376 frames per second, which corresponds to 496 MB/s [101].

The first step of image tracking is to reconstruct micro-tracks using aligned clusters of dark pixels. The position assigned to a micro-track is its intercept with the nearest plastic base

## 2.7. Automated Scanning System

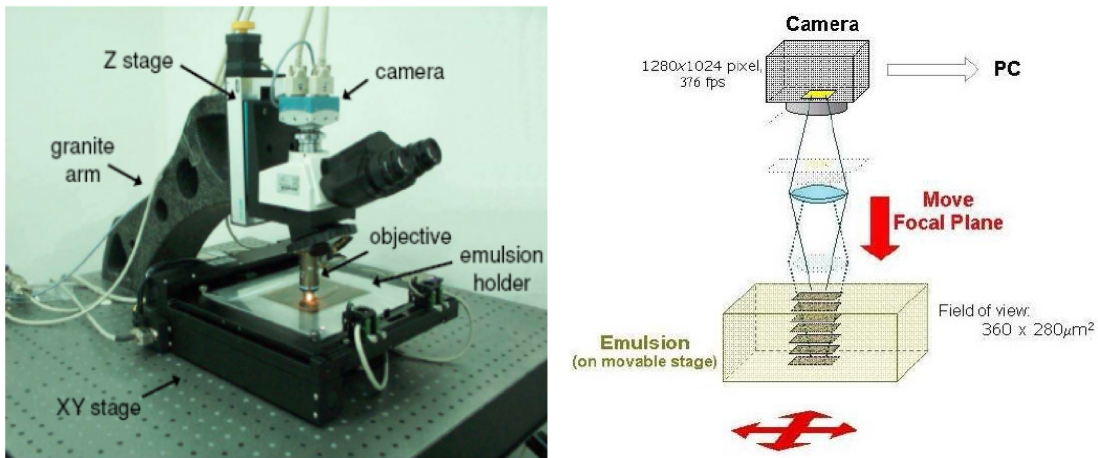


Figure 2.9 – A schematic view of the ESS microscope (left); Taking a series of successive images in different depths of the Emulsion (right).

surface. Then micro-tracks at both sides of plastic base are connected to form the base-tracks (Figure 2.10).

The final step of processing is to reconstruct particle tracks by connecting the base-tracks in consecutive emulsion films. In order to define a global reference system a set of affine transformations relating track coordinates have to be computed to account for scanning data taken plate by plate in different reference frames, relative misalignments and deformations.

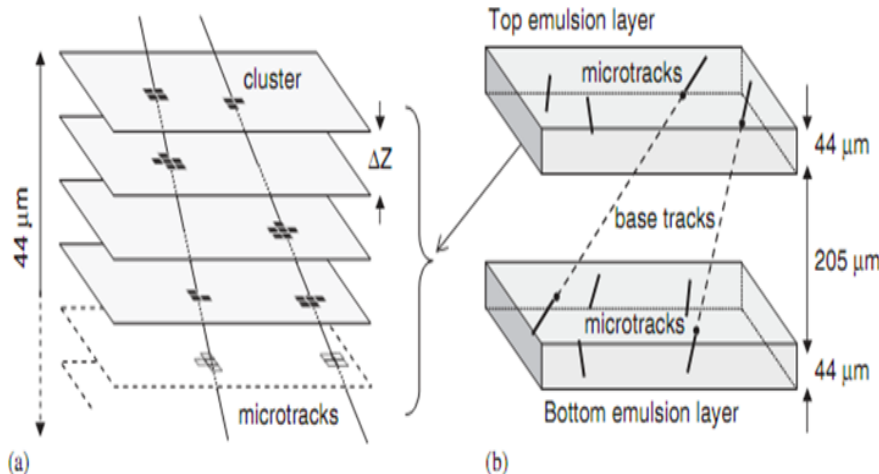


Figure 2.10 – Micro-track reconstruction in one emulsion layer by combining clusters belonging to images at different levels (left); micro-track connections across the plastic base to form base-tracks (right).

## 2.8 Physics Performances

### 2.8.1 Tau detection and signal efficiency

The signal produced in  $\nu_\mu \rightarrow \nu_\tau$  oscillations is a  $\nu_\tau$  CC interaction occurring inside the detector,  $\nu_\tau N \rightarrow \tau^- X$ , with the subsequent  $\tau$  decay. A summary of the different decay channels of  $\tau$ , the electron, muon and hadron channels, and their branching ratios (BR) is shown in Table 2.2.

$\tau$ decay channels	BR
$\tau^- \rightarrow e^- \nu_\tau \bar{\nu}_e$	17.8 %
$\tau^- \rightarrow \mu^- \nu_\tau \bar{\nu}_\mu$	17.7 %
$\tau^- \rightarrow h^- \nu_\tau (n\pi^0)$	49.5 %
$\tau^- \rightarrow h^- h^- h^+ \nu_\tau (n\pi^0)$	15 %

Table 2.2 – The  $\tau$  decay channels investigated by OPERA [97].

The decay length distribution of  $\tau$  particles that appear in detector through the  $\nu_\mu \rightarrow \nu_\tau$  interactions is shown in Figure 2.11, with an average decay length of about 600  $\mu m$ .

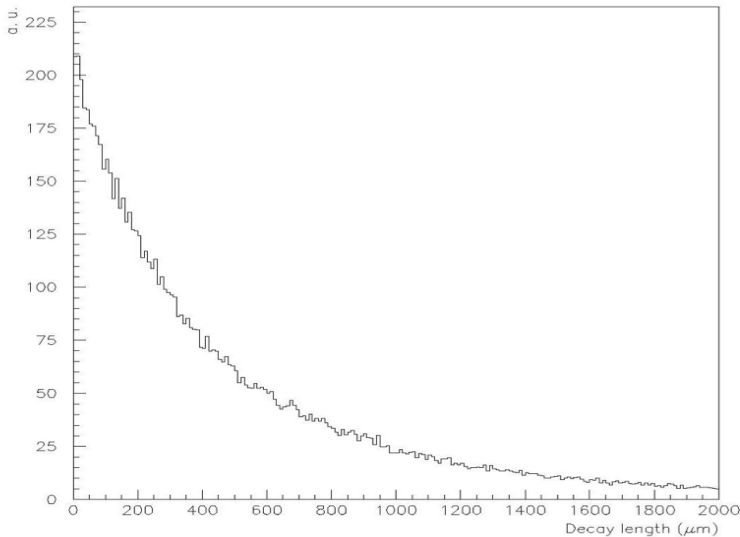


Figure 2.11 –  $\tau$  decay length distribution.

When a  $\tau$ -decay occurs inside the brick, it could be classified in two categories as shown in Figure 2.12:

- **Short-decay** corresponds to the events where the neutrino interaction occur in the same lead plate of the  $\tau$  decay.
- **Long-decay** corresponds to those events where  $\tau$ -decays take place in the first or second lead plate downstream of the neutrino interaction.

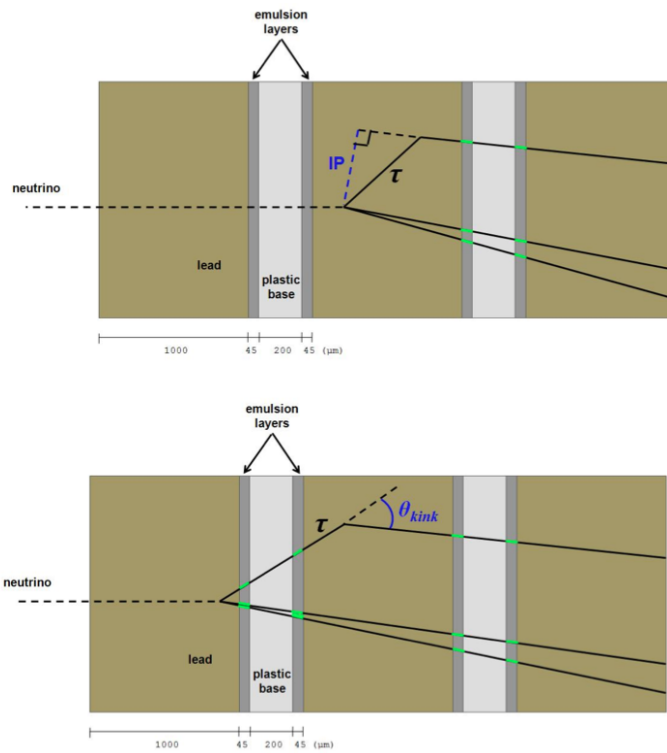


Figure 2.12 – Schematic picture of the  $\tau$  detection technique in the ECC cell for short (top) and long (bottom) decays [102].

In case of short decays,  $\tau$  candidates are identified by measuring the impact parameter (IP) of the daughter track with respect to the interaction vertex,  $IP < 20 \mu m$ . However for long decay cases, the identification of  $\tau$  particles is based on the large kink angle,  $\theta_{kink}$ , between  $\tau$  candidates and their daughter track,  $20 < \theta_{kink} < 500$  mrad, see Figure 2.12.

The analysis of tau decay in  $\tau \rightarrow e$  channel profits of the dense ECC structure that allows recognizing the electron through its shower development in the downstream emulsion films. The ECC technique is well suited to identify electrons and their showers. The energy of electrons can be estimated by measuring the density of track segments of electron showers produced in the brick.

The detection of the  $\tau$  decay for the muonic decay channel is based on the observation of a muon attached to the secondary decay vertex.

Tau decays into hadronic modes show the largest branching ratio,  $\sim 64\%$ . This channel is affected by the hadronic interactions background. In order to reduce the hadronic background, several kinematical cuts are applied.

The momentum of charged hadrons can be measured by using multiple coulomb scattering in the lead plates.

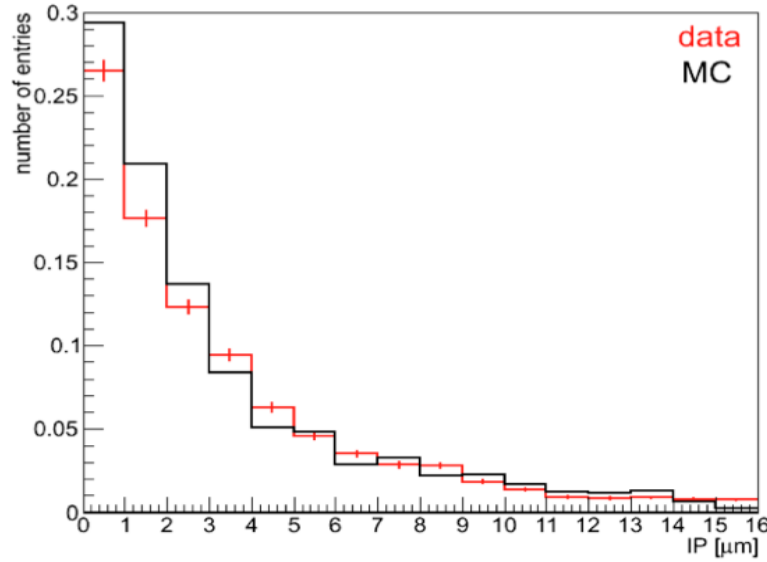


Figure 2.13 – Impact parameter measured in data and compared with simulation.

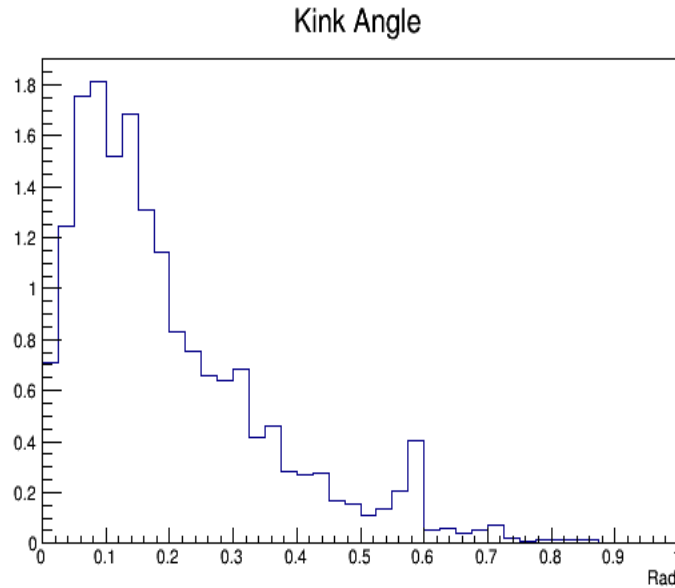


Figure 2.14 –  $\tau$  kink angle distribution for the  $\tau \rightarrow e$  decay mode.

### 2.8.2 Background

About 3 tau neutrino events, with CC interaction, was expected to be detected in the detector with less than one background event, assuming full mixing and  $\Delta m^2 = 2.44 \times 10^{-3} eV^2$ , for a total  $1.8 \times 10^{20}$  p.o.t. (protons on target). After 5 years of data taking about 19500 neutrino interactions were collected.

The background for  $\tau$  detection has different contributions:

**Decay of charmed particles:** Tau particles and charmed mesons show very similar lifetime and masses. As shown in Figure 2.15, if muon is not detected in the primary vertex, when a charm meson is produced, in a  $\nu_\mu^{CC}$  interaction ( $\nu_\mu N \rightarrow \mu^- cX$ ), the event is background.

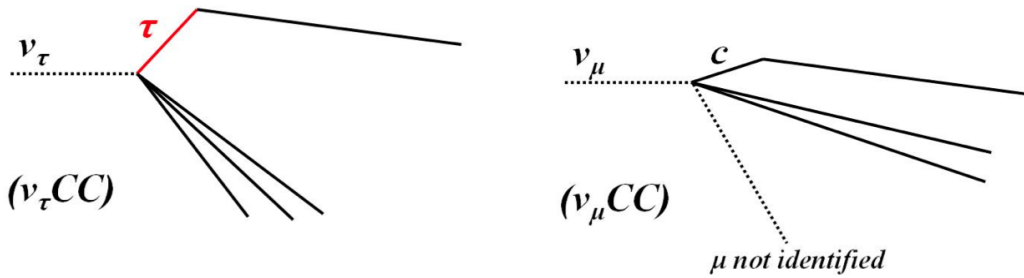


Figure 2.15 – Tau decay topology in the  $\nu_\tau^{CC}$  and the corresponding background from one prong decay of charmed particles when the produced muon is missed.

**Large angle muon scattering:** The other background is related to the large angle scattering of muons, produced in  $\nu_\mu^{CC}$  interactions, in lead for the  $\tau \rightarrow \mu$  decay channel. The background contribution is around  $5 \times 10^{-6} \times N_{CC}$  (Figure 2.16).

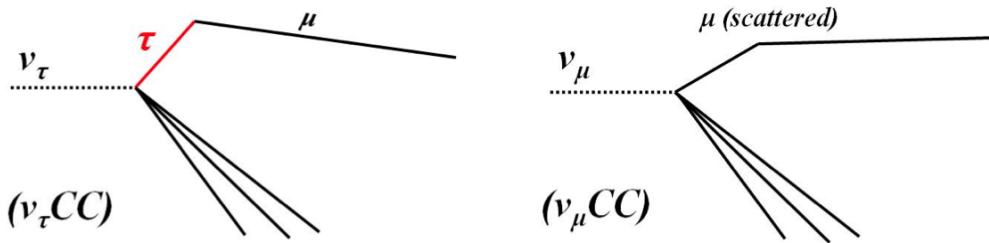


Figure 2.16 – Schematic view of the background from large angle muon scattering. A scattered muon could be as same as the decay of  $\tau \rightarrow \mu$  channel.

## Chapter 2. The OPERA Experiment

---

**Hadronic re-interactions:** In  $\nu_\mu^{NC}$  and  $\nu_\mu^{CC}$  interactions if the primary muon is not recognized, an important source of background for the  $\tau \rightarrow h$  channel is given by hadronic re-interactions. In Figure 2.17 a hadronic re-interaction is compared with a tau decay to show the similarity of these two topologies.

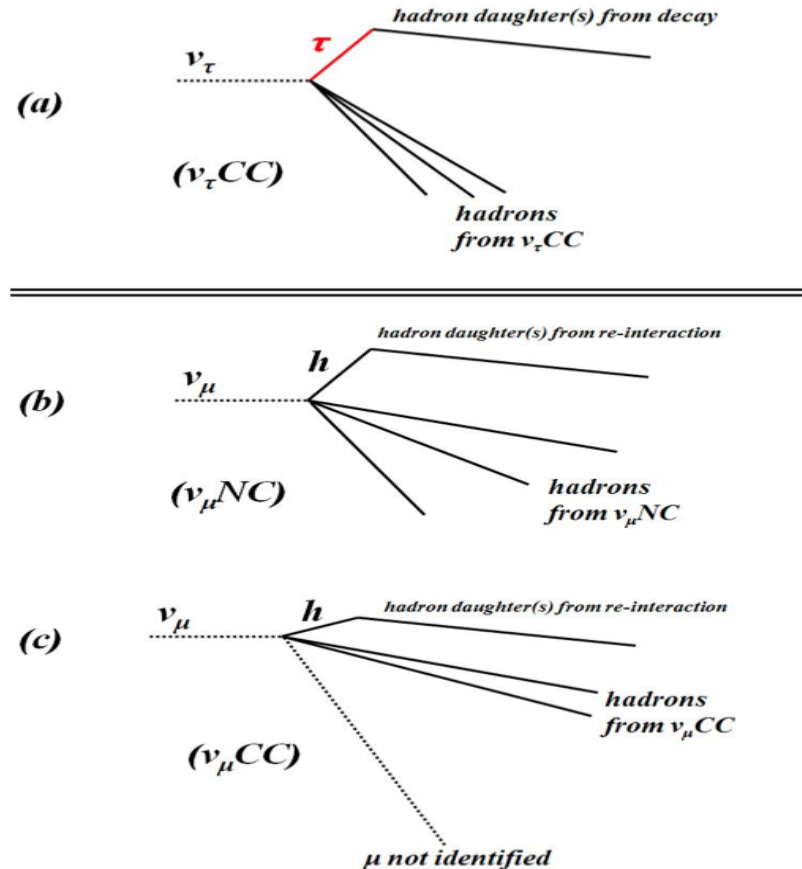


Figure 2.17 – Topologies of the  $\nu_\tau$  signal (a), background from hadron re-interactions from  $\nu_\mu^{NC}$  (b) and  $\nu_\mu^{CC}$  (c).

The contribution of these background sources is different for each decay channel. The summary of total number of background events for each  $\tau$  decay channel after 5 years of OPERA data taking is given in Table 2.3.

	$\tau \rightarrow e$	$\tau \rightarrow \mu$	$\tau \rightarrow h$	$\tau \rightarrow 3h$	Total
Charm	$0.027 \pm 0.005$	$0.003 \pm 0.001$	$0.015 \pm 0.003$	$0.152 \pm 0.030$	$0.198 \pm 0.040$
Muon scattering	0	$0.014 \pm 0.007$	0	0	$0.014 \pm 0.007$
Hadronic re-interactions	0	0	$0.018 \pm 0.005$	$0.002 \pm 0.001$	$0.021 \pm 0.006$

Table 2.3 – The total number of background events for each  $\tau$  decay channel.

### 2.8.3 Sensitivity to $\nu_\mu \rightarrow \nu_\tau$ oscillation

The OPERA detector has been exposed from 2008 to 2012 to the high-energy CNGS beam after two years of technical and low-intensity runs in 2006-2007. The detection of the first  $\nu_\tau$  candidate event satisfying the kinematical selection criteria was reported in 2010 [103, 104], using a sample corresponding to  $1.9 \times 10^{19}$  protons on target (pot). CNGS completed its operation on December 3, 2012. After five years data taking, a sample corresponding to  $17.97 \times 10^{19}$  pot has been registered by the detector since the beginning of the program in 2008 [105]. A summary of the collected data samples and the contained events is given in Table 2.4. Moreover, the present data analysis status of OPERA experiment is shown in Figure 2.18.

Year	p.o.t ( $10^{19}$ )	Contained events
2008	1.74	1931
2009	3.53	4005
2010	4.09	4515
2011	4.75	5131
2012	3.86	3923
Total	17.97	19505

Table 2.4 – Summary of the collected data samples and the contained events.

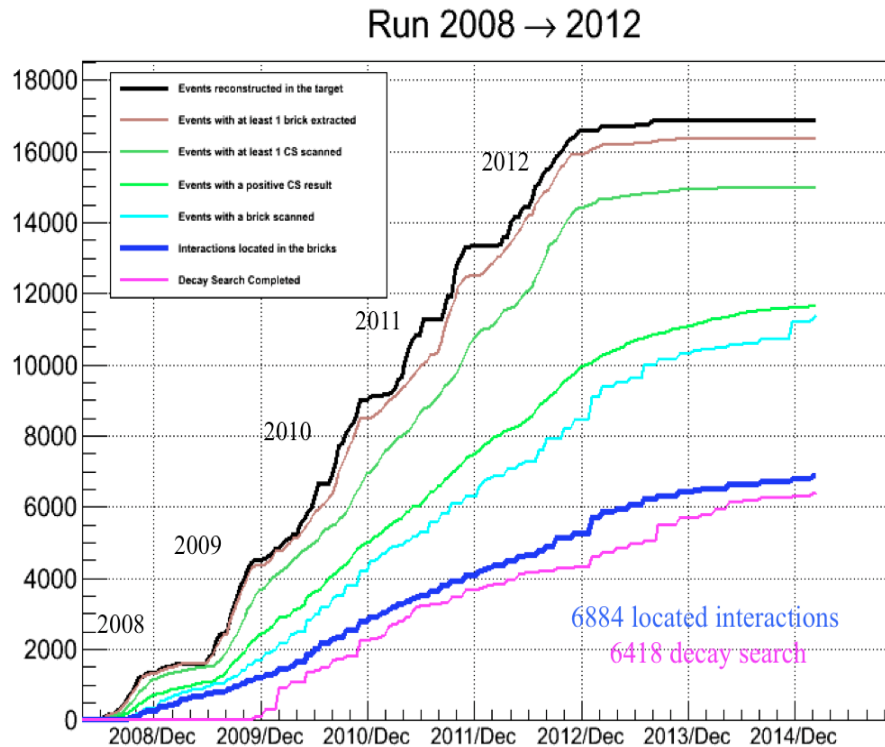


Figure 2.18 – The present data analysis status of OPERA.

## Chapter 2. The OPERA Experiment

---

Also a summary of the expected number of  $\tau$  signal events and their expected backgrounds for each decay channel is shown in Table 2.5.

$\tau$ decay channels	BR	Signal ( $\Delta m^2 = 2.32 \times 10^{-3} eV^2$ )	All Backgrounds	Observed
$\tau \rightarrow e$	17.8 %	$0.62 \pm 0.12$	$0.027 \pm 0.005$	0
$\tau \rightarrow \mu$	17.7 %	$0.52 \pm 0.10$	$0.018 \pm 0.007$	1
$\tau \rightarrow h$	49.5 %	$0.41 \pm 0.08$	$0.033 \pm 0.006$	2
$\tau \rightarrow 3h$	15 %	$0.57 \pm 0.11$	$0.155 \pm 0.030$	1
Total	100 %	$2.11 \pm 0.42$	$0.233 \pm 0.041$	4

Table 2.5 – Summary of the signal and backgrounds expectations for the analysed sample [106].

So far, four  $\nu_\tau$  candidate events have been observed with a total expected background of  $(0.233 \pm 0.041)$  events. OPERA has observed the  $\nu_\tau$  candidates for the following channels: one event in the  $\tau \rightarrow \mu$  decay channel, two events in the  $\tau \rightarrow 1h$  decay channel and one event in the  $\tau \rightarrow 3h$ . However, no observation for the  $\tau \rightarrow e$  decay channel at the moment. OPERA is enlarging the data samples and improving the analysis in order to improve the search for  $\nu_\tau$  candidates. Therefore, it was the motivation of this work to develop an algorithm for the search of  $\nu_\tau$  candidates in the  $\tau \rightarrow e$  decay channel. The fourth  $\nu_\tau$  candidate event will be briefly reported in the following.

Given the all analyzed samples,  $\nu_\mu \rightarrow \nu_\tau$  oscillations are established at the  $4.2\sigma$  level. The forth  $\nu_\tau$  candidate event was found in the new analysis sample and is reported here.

### 2.8.4 The fourth $\nu_\tau$ candidate event

The fourth neutrino interaction is registered on 9 September 2012 in the OPERA detector, ten brick walls upstream of the second muon spectrometer. It has been classified as  $0\mu$  event due to its electronic detectors display as shown in Figure 2.19.

The primary vertex of this event is made by four tracks, one of them decaying soon after. The primary vertex was located, 18 plates from the downstream face of the brick. Two electromagnetic showers given by conversions of  $\gamma$ -rays have been found where both pointing to the primary vertex as illustrated in the Figure 2.20. Momentum of the reconstructed tracks is calculated by using the Multiple Coulomb Scattering (MCS) method in the bricks [107]. An extra search by a special scanning procedure with a larger angular acceptance,  $\tan\theta = 3.5$  (where  $\theta$  is the angle of each track with respect to the z axis), confirmed that there is no nuclear fragment associated with the decay vertex [108].

None of the charged particles at both vertices is identified as an electron due to the absence of electromagnetic showers.

The  $\tau$  candidate track (Track1 in Figure 2.20) has a kink topology with an angle of  $\sim 137$  mrad.

## 2.8. Physics Performances

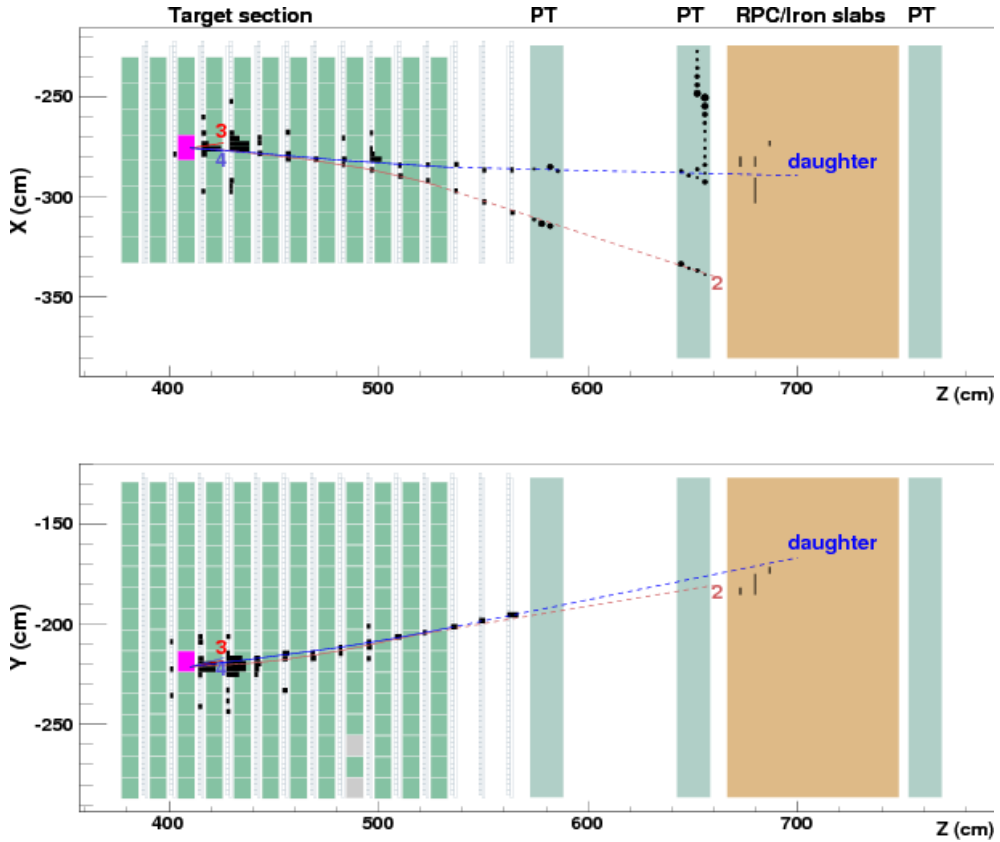


Figure 2.19 – Display of the  $\nu_\tau$  candidate event as seen by the electronic detectors in the x-z projection (top) and y-z projection (bottom). The brick containing the neutrino interaction is highlighted in magenta. Solid lines show the position of tracks measured in the primary and downstream bricks. Dashed lines show the linear extrapolation of the tracks using positions and slopes at the last measured point in the bricks [106].

Its flight length is also calculated as  $\sim 1100 \mu m$ . The longitudinal coordinate of the decay vertex with respect to the downstream face of the lead plate containing the primary vertex ( $z_{dec}$ ) is  $(406 \pm 30) \mu m$ . These two parameters satisfy the topological selection for the  $\nu_\tau$  interaction search (see Table 2.6).

The kink daughter track has a momentum of about 6.0 GeV/c. Its impact parameter with respect to the primary vertex is *sim*  $150 \mu m$ . It was followed in the downstream bricks till the end of the target. And it stopped in the spectrometer after leaving a signal in three RPC planes.

None of the charged particles at both vertices is identified as a muon due to result of a discriminating variable,  $D_{TFD}$ , to separate muons from hadrons [105]. A track is classified as a muon if  $D_{TFD}$  is above 0.8. Moreover, none of them is identified as an electron due to the absence of electromagnetic showers.

The scalar sum of the momentum of all particles measured in the emulsion films ( $p_{sum}$ ) is  $\sim 14.5$  GeV/c. The momentum of the daughter track ( $p_{2ry}$ ) is  $6.0^{+2.2}_{-1.2}$  GeV/c, well above the cut

## Chapter 2. The OPERA Experiment

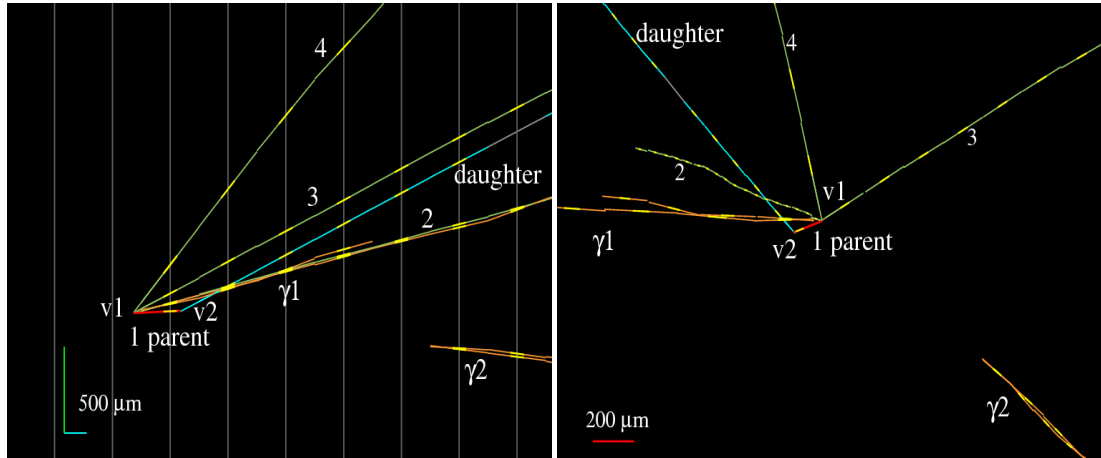


Figure 2.20 – Event display of the fourth  $\nu_\tau$  candidate event; Left: the y-z projection longitudinal to the neutrino direction, Right: the view transverse to the neutrino direction. The primary and decay vertices are indicated as "v1" and "v2" respectively [106].

value of 2 GeV/c [105]. The transverse momentum at the decay vertex,  $p_T^{2\gamma}$ , is  $0.82_{-0.16}^{+0.30}$  GeV/c that is above the lower cut of 0.6 GeV/c. The missing transverse momentum at the primary vertex ( $p_T^{miss}$ ) is  $0.55_{-0.20}^{+0.30}$  GeV/c, thus below the maximum allowed value, which is set at 1 GeV/c. The angle between the  $\tau$  candidate direction and the sum of the transverse momenta of the other primary particles is  $\sim 166$  degrees (see Figure 2.21), well above the lower cut at 90 degrees. The values of the kinematical variables for this event are summarized in Table 2.6. The measured values are well within the expected signal region.

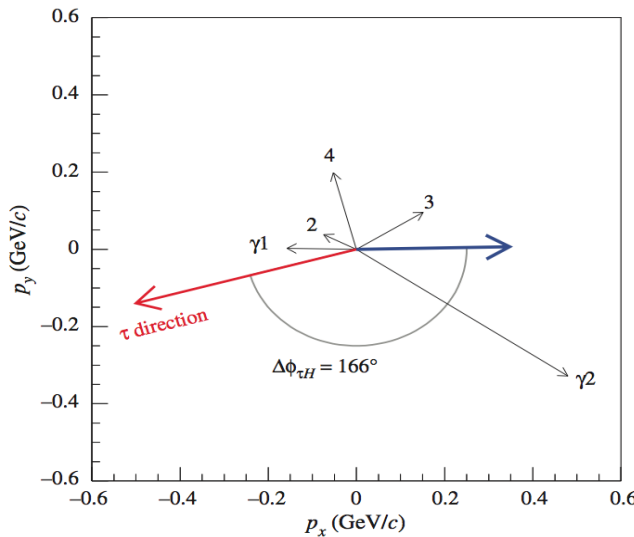


Figure 2.21 – The  $\tau$  direction (red arrow) and the other primary particles (black arrows) in the plane transverse to the beam. The blue arrow shows the vectorial sum of the primary particles except the parent..

## 2.8. Physics Performances

---

Variable	Selection	Measured value
$\theta_{kink}$ (mrad)	>20	137
$z_{dec}$ ( $\mu m$ )	<2600	406
$p^{2ry}$ (GeV/c)	>2	6.0
$p_T^{2ry}$ (GeV/c)	>0.6	0.82
$p_T^{miss}$ (GeV/c)	<1	0.55
$\Delta\phi$ (degrees)	>90	166

Table 2.6 – Selection criteria for the  $\nu_\tau$  interaction search in the  $\tau \rightarrow 1h$  decay channel and the values measured for the fourth  $\nu_\tau$  candidate event [106].



# 3 Search For $\nu_\tau$ Interactions in $\tau \rightarrow e$ Decay Channel

This work is focused on the study of the detection of  $\nu_\tau$  interactions in the  $\tau \rightarrow e$  decay channel and electron neutrino interactions. The aim of this study is to develop an improved algorithm to identify and reconstruct the electron shower inside the OPERA brick and to improve the energy resolution for electrons produced in  $\nu_e$  interactions and in case of tau decaying to an electron through their showers.

Analyzing a neutrino interaction in OPERA requires several steps; a flow diagram for the analysis chain of neutrino interactions is shown in Figure 3.1. The electronic detectors care about the first two steps, the electronic detector trigger and brick finding, in order to define the position of the neutrino interactions in the detector and to identify the brick where the interaction occurred. The next step is locating the neutrino interaction vertex in emulsion by the changeable sheets analysis and the scan-back method. After finding the neutrino interaction vertex, a decay search is applied in order to reconstruct the all possible tracks attached to the vertex and find a decay vertex.

In this chapter all above steps are explained in details and the efficiencies of the different steps are calculated for  $\nu_e$  interactions as well as for those  $\nu_\tau$  interactions where the tau lepton decays into an electron. The use of the brick as a calorimeter and the energy measurement of the electron for both  $\tau \rightarrow e$  decay channels and  $\nu_e$  interactions will be reported in the next chapter.

## 3.1 Monte Carlo Event Simulation

The OPERA software framework, so called OpRelease, is based on the Object Oriented Data Analysis Framework (ROOT) [109] and it is written in C++. Furthermore, a Configuration Management Tool (CMT) [110] is used in order to set the environment variables and to create the execute files. The OpRelease is managed by the Concurrent Versions System (CVS) [111] and stored on the OPERA CVS repository at CERN.

The OPERA software chain for data simulation is starting by the event generator NEGN (Neu-

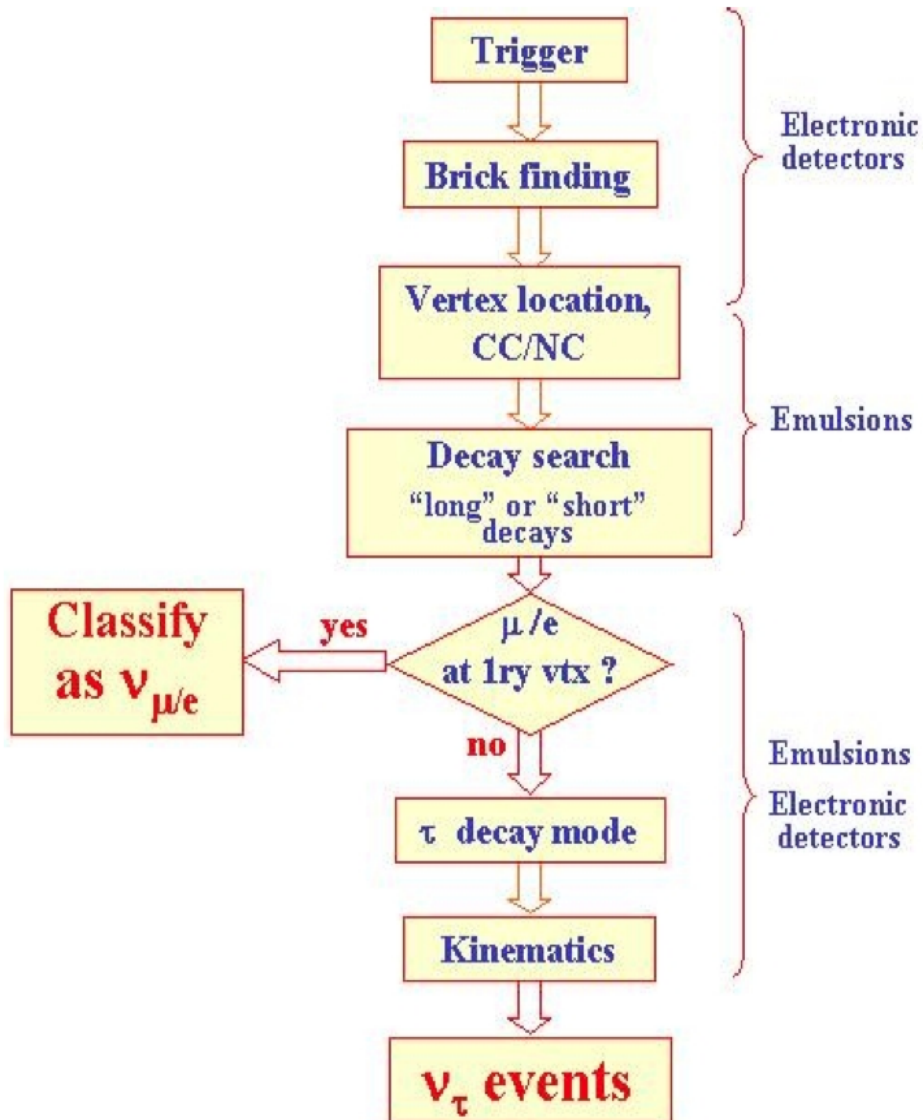


Figure 3.1 – Flow diagram of the analysis chain to search for neutrino interactions [113].

trino Event Generator for NOMAD) [112] and its output is converted into a ROOT file format through OpConverter. The geometry of the detector is defined in OpGeom package and afterward, the OpSim package simulates the Hits of particles produced when crossing the detector. In the following, the different steps of the simulation chain will be explained.

**OpNegrn** package is the neutrino event generator for OPERA experiment. It is based on the NEGN, which benefits from the experience earned at NOMAD experiment. For OPERA some modifications were needed regarding the description of the beam-line, the neutrino energy spectrum and the CNGS target.

**OpGeom** is based on the ROOT geometry and the class TGeoManager that defines the full geometry of all detector parts. In addition, the major objects surrounding the detector like the BOREXINO experiment just upstream of the OPERA detector and the surrounding rock are also simulated.

**OpSim** simulates the hits of particles that propagate inside the detector. OpSim package is based on the ROOT Virtual Monte Carlo (VMC). The output of OpSim is a ROOT file including the information about the particle propagation (the hits) in the detector.

**OpDigit** simulates the detector response for all subdetectors.

**OpRData** is the package describing the data format. The data structure is managed by the TreeManager and it is saved by ROOT. The TreeManager produce and read the OPERA format files.

**OpRec** package manages the kinematical reconstruction and identification of particles for both simulated and real data. Other tasks of this package are event energy evaluation; event time tagging and muon identification.

**OpCarac** is meant to classify the OPERA events detected and reconstructed by OpRec. Each event is categorized as one of the following classes: CONTAINED (if the interaction vertex lies inside the OPERA target), SPECTRO (if the interaction is inside the spectrometer), SIDEMUON (if the interaction particles entering the detector from the sides for example when the CNGS neutrino beam interacts in the surrounding rock around detector), FRONTMUON (same as the SIDEMUON where the neutrino interactions are take place inside the BOREXINO detector or upstream rock and UNKNOWNTYPE if none of the above appears).

**OpBrickFinding** is to identify the brick where the neutrino interaction occurred, for those flagged as CONTAINED by OpCarac package. It provides a probability map for each brick to contain the neutrino interaction.

**OpEmuIO** package is to simulate the scanning system and also to build track segments in the emulsion films. OpEmuIO applies the efficiencies of the scanning system and a Gaussian smearing on the micro-track positions and slopes according to the measured errors.

**OpEmuRec** analyzes the emulsion data and it is the tool used for the data analysis. Some algorithms, used both for Monte Carlo and data, are meant for the event reconstruction and data analysis; other algorithms are used to simulate the location chain.

## 3.2 Electronic Detector Analysis

The data acquisition trigger is used to select only those events on time with the beam, by checking the CNGS beam and OPERA event time coincidence. Afterward, the electronic detector trigger defines the existence of hits in the X and Y projections. Moreover, it reconstructs 3D tracks in the electronic detector.

### 3.2.1 Event Classification

As mentioned before, the OpCarac package classifies whether events are CONTAINED in the OPERA detector or not. The major component of external events is classified as SIDE MUON or FRONT MUON. Events with a relatively modest energy deposition only in the edge part of the detector are classified as BORDER SOFT NC. They can either be due to low energy neutrino interactions occurring at the edge or to interactions outside the detector with a leak inside [114, 115]. In order to have a high efficiency, BORDER SOFT NC events are added to the CONTAINED ones in the data analysis.

### 3.2.2 MuonID Classification

According to electronic detector response these events are categorized as  $1\mu$  or  $0\mu$  events, shown in Figure 3.2. To classify an event as  $1\mu$  event one of the following conditions should be satisfied: either a 3D track with a "length  $\times$  density" value greater than  $660 \text{ g/cm}^2$  is reconstructed; or the number of TT and RPC planes containing at least one hit has to be larger or equal to 19. The complementary sample is defined as  $0\mu$ .

The momentum of muon tracks is calculated through their bending in the muon spectrometer. The momentum of muon is determined as the momentum of the longest 3D track. This 3D track is provided by a Kalman Filter [116].

### 3.2.3 Brick Finding

A probability map based on the track reconstruction and the energy deposit in the electronic detector is evaluated to find the bricks with high probability of having the neutrino interactions. OpEmulIO algorithm allocated a probability to each brick in a cube made of  $3 \times 3 \times 3$  bricks, as shown at Figure 3.3, around the brick that contains the neutrino interaction.

The bricks are ranked according to their probability such as first probable brick, second probable brick and so on. A Brick Manipulator System (BMS) is used to extract the most probable bricks. After the brick is extracted, their CS is sent to the CS scanning laboratory and, as shown in Figure 3.4, the found CS tracks are superimposed with the electronic detector hits to confirm that the found tracks are correlated with the neutrino interaction.

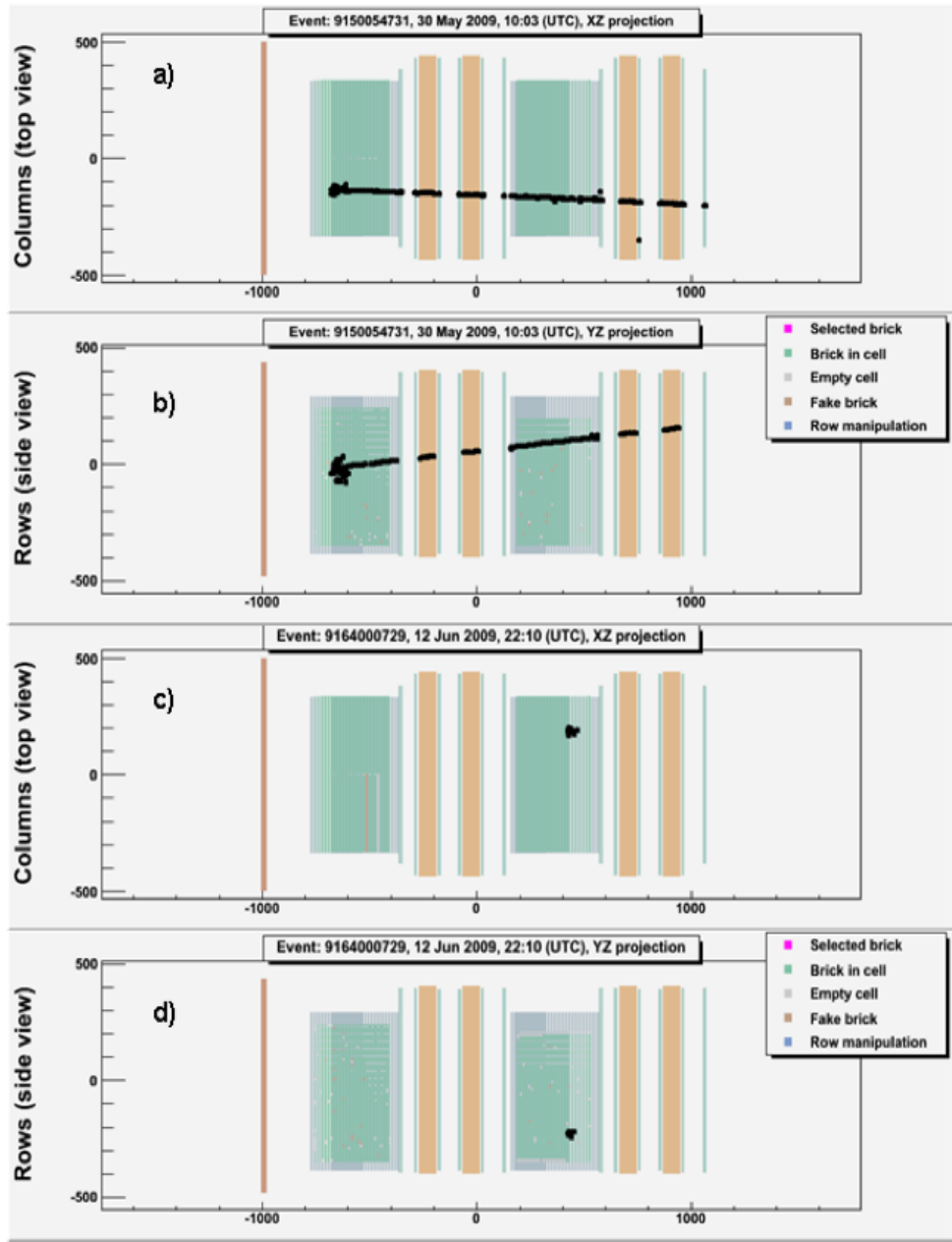


Figure 3.2 – Whole detector display in (a) x-z and (b) y-z projections for an event classified as  $1\mu$ ; and (c) and (d) show x-z and y-z projections respectively, for a  $0\mu$  event.

### 3.3 Emulsion Analysis Chain

In the following, the different steps of OPERA bricks analysis such as Changeable Sheet (CS) analysis, CS to brick connection, Scan-back, Volume Scan and vertex reconstruction, Vertex Definition and Decay Search will be briefly explained.

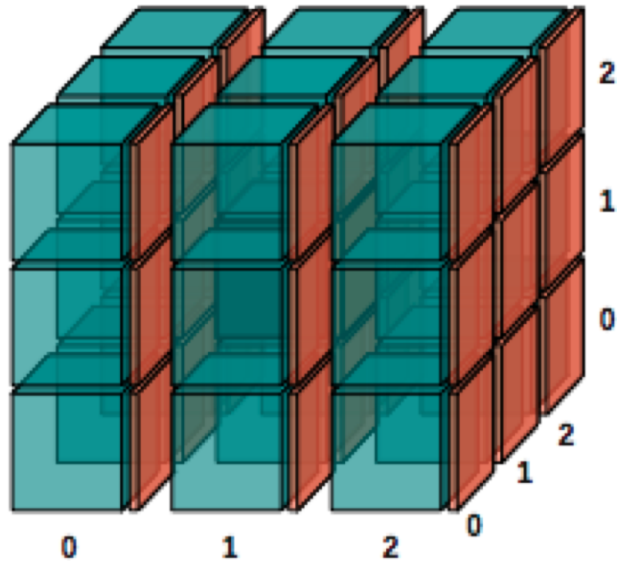


Figure 3.3 – The  $3 \times 3 \times 3$  matrix where the brick identification algorithm is applied. The true brick where the interaction occurred is the 111.

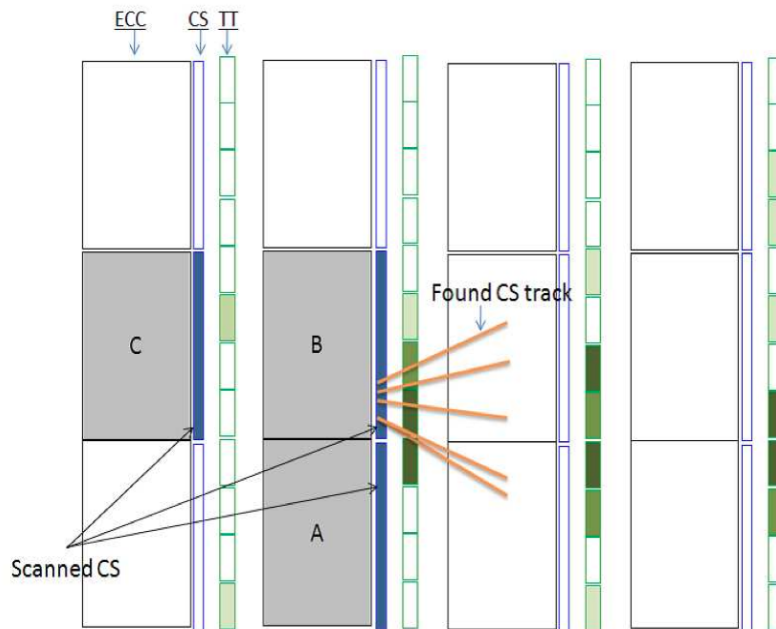


Figure 3.4 – After the bricks are extracted, the CS scanning result is superimposed to a zoom of the TT display. Clearly brick B contains the event and it is thus developed.

### 3.3.1 Changeable Sheet Analysis

When a neutrino interaction is detected by OPERA detector, first is triggered by electronic detectors and is classified as a  $1\mu$  or  $0\mu$  event, according to the presence of the muon track

reconstructed by electronic detectors. Using the electronic detector data a probability map is calculated to find the most probable brick in which the neutrino interaction took place. Then, its CS doublet are detached, developed and scanned.

The scanned area of CSs will be selected differently for the  $1\mu$  and  $0\mu$  neutrino interaction. The scanned area for CC interactions is an area of  $6 \times 4 \text{ cm}^2$  per emulsion around the predictions provided by the ED hits. However, for the NC interactions this area is  $8 \times 6 \text{ cm}^2$ . Inside the scanned area of CSs only a few tracks related to the event are expected, and they will be all checked and confirmed by an eye-check procedure when needed.

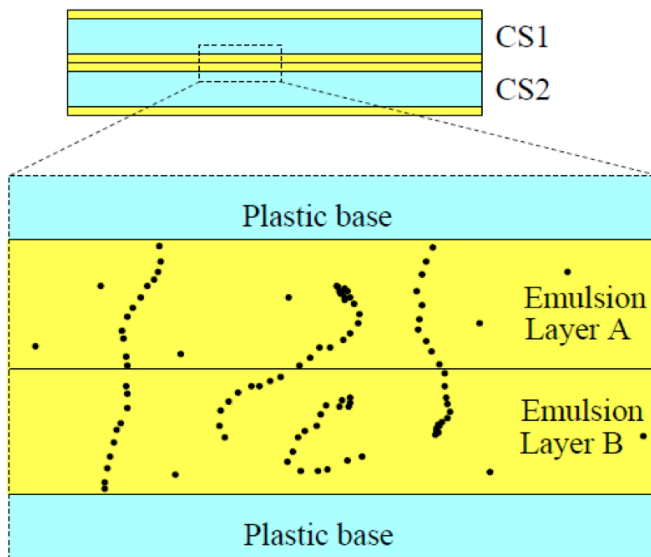


Figure 3.5 – The alignment between the two layers is done by matching the Compton- electron tracks [117].

To connect the two CS doublets, the position marks of the X-ray grid are used. As shown in Figure 3.5 a better matching can be provided by the alignment of the Compton-electron tracks found in both CSs. Afterwards a "3 out of 4" search can be performed. The "3 out of 4" is the case that from the four micro-tracks of both CS doubles only three of them are found. If after the Compton-alignment and the 3 out of 4 search no CS track candidate was found, the second probable brick is extracted and its CSs will be scanned. A new CS doublet will be attached to the original extracted brick and it will be re-inserted in the OPERA target.

#### 3.3.2 CS to Brick Connection

If the CS analysis validates the brick, its films will be developed at LNGS laboratories. After that, the ECC films are sent to the scanning sections to be analyzed. The electronic detector reconstruction information and CS scanning results are stored in a central database accessible by all scanning laboratories.

The "CS to brick connection" procedure is then applied in the scanning laboratories. This procedure is intended to associate the found CS tracks with the corresponding tracks inside the brick. CSs are  $4500 \mu\text{m}$  far from the brick and its tracks are projected to the most downstream emulsion film of the brick in order to obtain the nominal position, see Figure 3.6.

For the search around each prediction, an area of  $3 \times 3 \text{ mm}^2$  is scanned. All the tracks within  $300 \mu\text{m}$  around the prediction that having a slope within 30 mrad are visually checked to discard fake tracks. If a track is confirmed, its new prediction is projected to next most downstream film to check whether they are compatible with the CS predictions or not. All candidate tracks selected will be the input of the scan-back procedure.

### 3.3.3 Scan-back

The "scanback" procedure is the process to locate the neutrino interaction inside the brick. After the "CS to brick connection", the candidate tracks are followed up plate by plate, as shown in Figure 3.6, until they disappear. The scanback starts from the most downstream film and it proceeds in the upstream plates using the extrapolated position of found segments. The accuracy of extrapolation from one plate to the adjacent one is around  $10\text{-}20 \mu\text{m}$ .

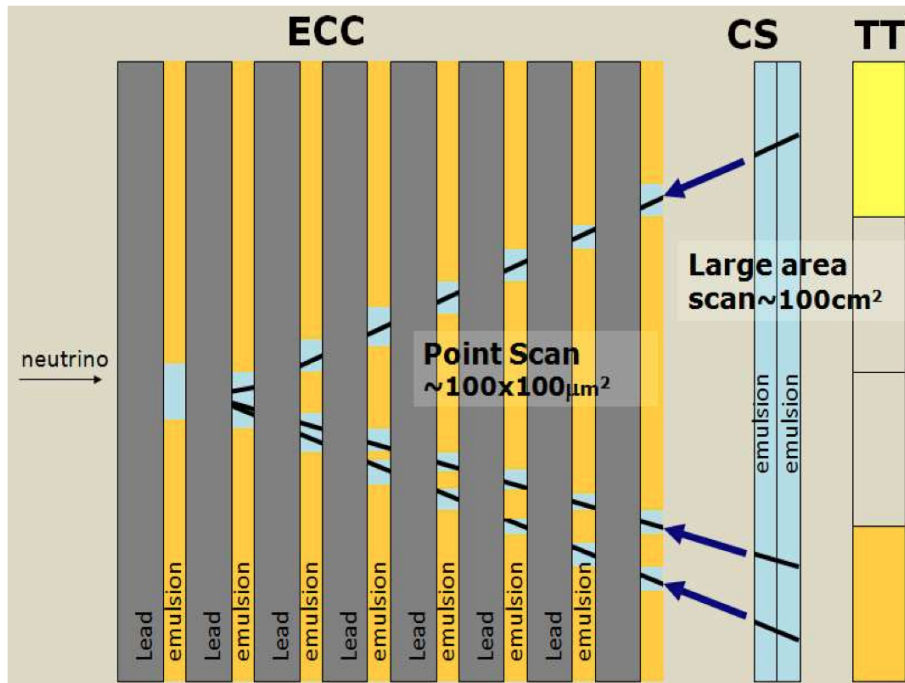


Figure 3.6 – Schematic representation of the "scanback" procedure. When the track disappear for 5 consecutive plates the interaction point is located [117].

The scanback process is continued until one of the following conditions occurs:

**No segments are found in at least five consecutive plates.** The last plate that the followed track is found is called the stopping point. The scanning of at least 5 plates upstream the stopping point is due to avoid the fake scanback stopping point. It could happen due to reconstruction algorithm or the acquisition inefficiencies.

Sometime it may happen that the stopping point of the followed track is reconstructed with wrong parameter or a background track is selected as a stopping point. Therefore, the stopping point will be confirmed by eye-check of the predicted position in the five consecutive films upstream.

**The followed track exits the brick; it is so called passing-through.** The passing-through means the neutrino interaction has not taken place inside the current brick. The interaction could be found inside the upstream brick or inside a neighbor brick. Some of the neutrino interactions take place in the target frame, or in the target tracker detector; this kind of events cannot be used for neutrino oscillation search where the vertex region cannot undergo the topological analysis.

#### 3.3.4 Volume Scan

After the scanback process finds a stopping point, a scan of the volume around the stopping point is performed. The scan volume consists of 15 consecutive plates with an area of  $1\text{cm}^2$  for each plate, 10 plates downstream of the stopping point and 5 upstream, as shown in Figure 3.7.

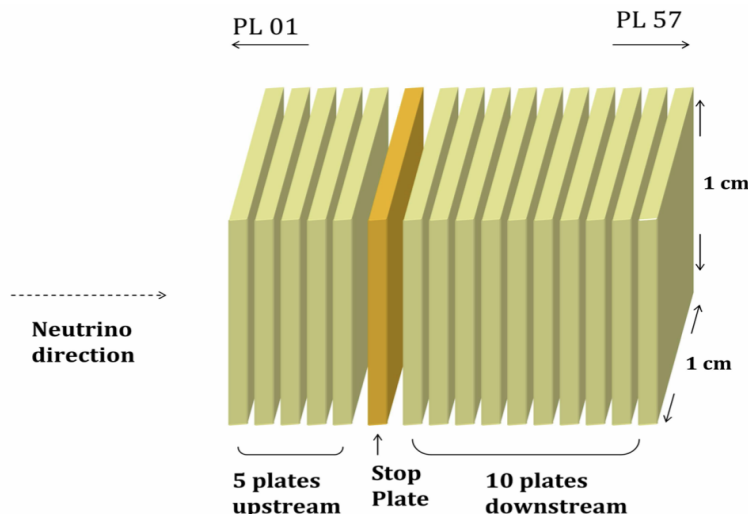


Figure 3.7 – Schematic drawing of the volume scan. Scanning 10 plates downstream of the stopping point and 5 upstream prepare this volume.

The five upstream plates act as a confirmation of the stopping point, while the ten downstream plates are used to reconstruct the neutrino interaction (and possible secondary vertices) and to classify the event as located. The angular acceptance used in the scanning is 0.6 rad wide with respect to the perpendicular direction to emulsion films. After scanning each film the base-tracks are reconstructed in each emulsion films. The alignment between the films is performed with high penetrating cosmic ray tracks accumulated during a dedicated exposure just before the development.

An automatic software is used to reconstruct the tracks and vertices. In this reconstruction, only volume tracks with at least two base-tracks are considered. This track selection makes the identification of the electromagnetic showers very difficult because in this way the single base-tracks, related to the low momentum tracks, are discarded. In this thesis, a new method is developed to reconstruct electromagnetic showers using single base-tracks to increase the efficiency of the electromagnetic showers reconstruction and improve the energy estimation.

### 3.3.5 Vertex Reconstruction

After confirming the stopping point and reconstructing the neutrino interaction vertex in the volume scan, a procedure is applied in order to define the neutrino interaction point more precisely. The information of the tracks found in the last film, immediately downstream of the neutrino interaction, is important to improve the accuracy of the vertex position. When needed, those track segments are visually inspected to reject fake tracks and to re-compute the vertex position. Sometimes the track segments in very downstream film, after the vertex, could be missing in the reconstruction because of tracking inefficiency. In addition,  $e^+e^-$  pairs coming from the conversion of gammas produced in  $\pi^0$  decays and pointing to the vertex can spoil the accuracy. At the end, the neutrino interaction vertex position is calculated as the average position of all tracks connection points.

All tracks having an impact parameter less than  $10 \mu m$  are accepted in the primary vertex. However for those tracks with an impact parameter grater then  $10 \mu m$ , a further study is needed to understand if its origin is due to multiple scattering in the traversed lead thickness or it is just due to a background track; to figure out this, an estimation on the momentum of particle is performed.

The momentum of particle is measured by applying the Multiple Coulomb Scattering (MCS) algorithm. The particles having a momentum less than  $1 GeV/c$  are defined as "low momentum particles" and will be disconnected from the vertex in order to have a more accurate determination of the vertex position.

Figure 3.8 shows the impact parameter distribution of the tracks in  $\nu_\mu^{CC}$  interactions with respect to the reconstructed vertex position both for data and simulation. Only less than 5% of the tracks have an impact parameter larger than  $10 \mu m$  and it is due to low-energy particles.

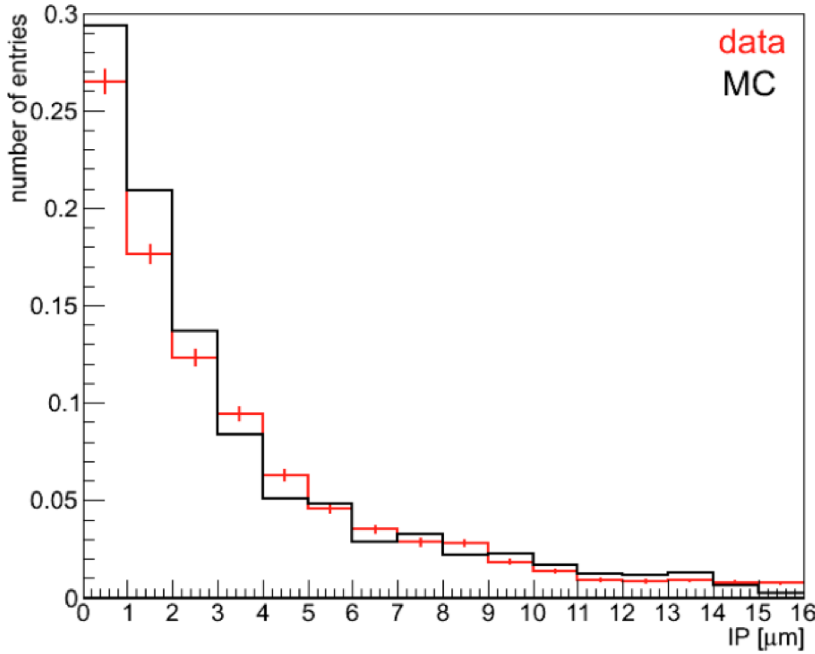


Figure 3.8 – Impact parameter distribution of the primary tracks in  $1\mu$  events with respect to the reconstructed vertex, after the primary vertex definition. The distribution is normalized to unity.

### 3.3.6 Decay Search

Once the primary vertex is defined, all tracks with an impact parameter that cannot be explained through the scattering effect have to be clearly investigated to check for the presence of a possible short decay. In fact, the decay search procedure looks for short-lived particle decays, such as tau and charmed particles.

Tracks reconstructed inside the analyzed volume that are not attached to the primary vertex are potential decay daughters and are called "extra-tracks". The extra-tracks selection is based on three different criteria:

- the longitudinal distance between the neutrino interaction and the most upstream segment of the track ( $\Delta Z$ ) should be smaller than  $3.6\text{ mm}$ ;
- the impact parameter with respect to the primary vertex should be smaller than  $300\text{ }\mu\text{m}$  if  $\Delta Z \leq 1\text{ mm}$ , and smaller than  $500\text{ }\mu\text{m}$  if  $\Delta Z \geq 1\text{ mm}$ ;
- the reconstructed track should have at least three segments.

Extra-tracks are also considered to filter out the electron-positron pairs produced from  $\gamma$  conversion coming from  $\pi^0$ , particles not originating in the volume scan (typically, low momentum particles reconstructed as shorter tracks due to MCS) and fake tracks due to the

failure of the reconstruction program. The surviving extra-tracks originating in the interaction vertex will be analyzed to check if they have a low momentum or not.

In addition, to detect long decays a dedicated procedure, so called "parent search", is applied to the extra-tracks starting downstream of the vertex position. It means searching for a track that connects the selected extra-track to the reconstructed vertex. For that, the impact parameter of this track should not be larger than  $10 \mu m$  with respect to the reconstructed vertex and the minimum distance from the extra-track (the daughter track) should be smaller than  $20 \mu m$ , see Figure 3.9. Any candidate parent track selected according to these criteria is confirmed by a visual inspection.

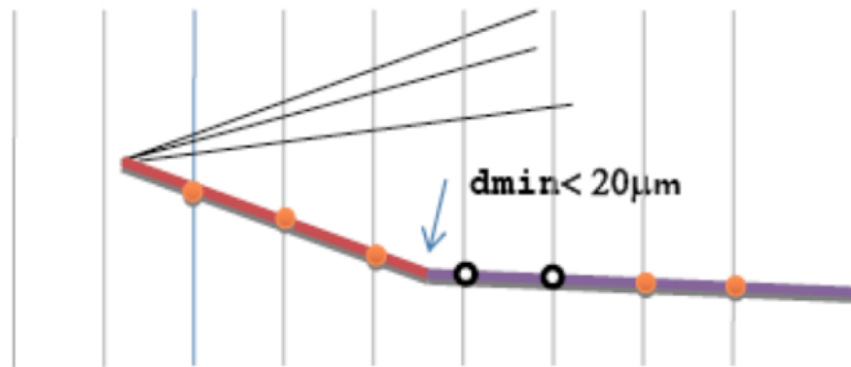


Figure 3.9 – The parent search procedure consists of searching for segments connecting an extra-track to the primary vertex.

## 3.4 Event Location and Decay Search Efficiency Assessment

### 3.4.1 Efficiency Assessment with Monte Carlo Simulations

Monte Carlo (MC) simulation is used to estimate the detector performance. Many analyses in this thesis is done using MC samples to estimate the event location efficiency, electromagnetic shower reconstruction and measuring the energy of the electromagnetic showers. Table 3.1 shows the information related to all these MC samples processed through the entire OpRelease 5.0 reconstruction. They contain the neutrino interactions in ECC bricks randomly distributed in the whole detector.

The MC samples have been analyzed by OpRelease framework combined with OpEmuRec packages in order to calculate the event location and DS efficiencies in all different process of event reconstruction such as Brick Finding (BF), Changeable Sheet (CS) analysis, Scan Back

### 3.4. Event Location and Decay Search Efficiency Assessment

File name	Channel	# of interactions
nue-events-8k	$\nu_e$ from the beam contamination	8000
oscillated-nue-3k	Oscillated $\nu_e$ generated with $\nu_\mu$ energy spectrum	3000
taue-5k	Oscillated $\nu_\tau$ in $\tau \rightarrow e$ mode	5000
numunc-5k	$\nu_\mu^{NC}$ interactions	5000
numucc-5k	$\nu_\mu^{CC}$ interactions	5000

Table 3.1 – MC samples used in the analyses of this work.

(SB) and Decay search (DS) procedure, as described in section 3.2 and 3.3.

An event is classified as  $1\mu$  if either it contains at least one track tagged as a muon or the total number of fired TT or RPC planes is larger than 19. The complementary sample is defined as  $0\mu$ . The data set used in the present analysis consists of  $0\mu$  and  $1\mu$  events with a muon momentum smaller than 15 GeV/c. During the OPERA runs two different data selections are defined:

**2008 and 2009 data selection:** in order to gain confidence on OPERA data, for the first two years no kinematical cut was applied. The highest and second probable bricks of the event have been analyzed.

**2010, 2011 and 2012 data selection:** once a good description of the data was achieved, a kinematical selection for  $1\mu$  events was applied in order to speed-up the analysis without reducing the  $\tau$  signal;  $1\mu$  events with the muon momentum smaller than 15 GeV/c have been analyzed ( $|p_\mu| < 15$  GeV/c). The analysis of the most probable bricks was performed at first for all the events. The analysis of second bricks is in progress.

Table 3.2 and Table 3.3 give the summary of event location (and DS efficiency) step-by-step for all MC samples: prompt  $\nu_e$ , oscillated  $\nu_e$ ,  $\nu_\mu \rightarrow \nu_\tau$  in  $\tau \rightarrow e$  mode and  $\nu_\mu^{NC}$ . In addition, the event location for  $\nu_\mu^{CC}$  events that are misidentified as  $\nu_\mu^{NC}$  is given in Tables 3.4 and 3.5. This effect is due to misidentification of the muon track for  $\nu_\mu^{CC}$  events. The efficiency of this samples are very low compared to other samples.

Table 3.2 shows that for 2009 and 2010 data samples all channels with an electron in the final state have a location efficiency larger than 45%. The  $\nu_\mu^{NC}$  channel is significantly lower and difference is in the muon identification. However, energetic NC-like events present long hadronic tracks that can be misidentified by the muon identification algorithm or by electronic detector. It is also true for the 2010, 2011 and 2012 data selections. The efficiency of this selection, starting from the brick finding, is slightly lower for each channel compare to the previous selection due to the analyzing only most probable bricks at first for all the events. The Decay Search is applied only to  $\tau \rightarrow e$  decay channel having a decay in its final state.

### Chapter 3. Search For $\nu_\tau$ Interactions in $\tau \rightarrow e$ Decay Channel

---

	prompt $\nu_e$	oscillated $\nu_e$	$\nu_\mu^{NC}$	$\tau \rightarrow e$ (Long)	$\tau \rightarrow e$ (Short)
ED Trigger	$0.984 \pm 0.001$	$1 \pm 0$	$0.995 \pm 0.001$	$1 \pm 0$	$1 \pm 0$
Event Classification	$0.885 \pm 0.008$	$0.86 \pm 0.01$	$0.903 \pm 0.006$	$0.911 \pm 0.009$	$0.898 \pm 0.009$
OpCarac	$0.841 \pm 0.008$	$0.82 \pm 0.01$	$0.829 \pm 0.007$	$0.854 \pm 0.009$	$0.844 \pm 0.010$
BF	$0.673 \pm 0.009$	$0.703 \pm 0.011$	$0.592 \pm 0.008$	$0.714 \pm 0.010$	$0.704 \pm 0.011$
CS	$0.533 \pm 0.009$	$0.655 \pm 0.011$	$0.323 \pm 0.008$	$0.586 \pm 0.011$	$0.578 \pm 0.012$
SB	$0.473 \pm 0.009$	$0.584 \pm 0.011$	$0.275 \pm 0.008$	$0.481 \pm 0.011$	$0.489 \pm 0.012$
DS	-	-	-	$0.227 \pm 0.009$	$0.178 \pm 0.009$

Table 3.2 – The summary of event location and DS efficiency for each reconstruction step for 2008 and 2009 data selection. The efficiency of each step is cumulative with respect to previous steps. The uncertainties are due to statistical errors.

	prompt $\nu_e$	oscillated $\nu_e$	$\nu_\mu^{NC}$	$\tau \rightarrow e$ (Long)	$\tau \rightarrow e$ (Short)
ED Trigger	$0.984 \pm 0.001$	$1 \pm 0$	$0.995 \pm 0.001$	$1 \pm 0$	$1 \pm 0$
Event Classification	$0.885 \pm 0.008$	$0.86 \pm 0.01$	$0.903 \pm 0.006$	$0.911 \pm 0.009$	$0.898 \pm 0.009$
OpCarac	$0.841 \pm 0.008$	$0.82 \pm 0.01$	$0.829 \pm 0.007$	$0.854 \pm 0.009$	$0.844 \pm 0.010$
BF	$0.532 \pm 0.009$	$0.583 \pm 0.011$	$0.446 \pm 0.008$	$0.574 \pm 0.011$	$0.550 \pm 0.012$
CS	$0.430 \pm 0.009$	$0.543 \pm 0.011$	$0.260 \pm 0.007$	$0.48 \pm 0.01$	$0.463 \pm 0.012$
SB	$0.378 \pm 0.009$	$0.485 \pm 0.011$	$0.227 \pm 0.007$	$0.391 \pm 0.011$	$0.392 \pm 0.011$
DS	-	-	-	$0.188 \pm 0.009$	$0.146 \pm 0.009$

Table 3.3 – The summary of event location and DS efficiency for each reconstruction step for 2010, 2011 and 2012 data selection. The efficiency of each step is cumulative with respect to previous steps. The uncertainties are due to statistical errors.

Table 3.4 and Table 3.5 show the location efficiency of those  $\nu_\mu^{CC}$  events that misidentified as  $\nu_\mu^{NC}$  events. The location efficiency for these events is very small having the advantage of the muon identification.

#### 3.4.2 Efficiency Assessment Base on Data

The location efficiencies calculated by MC simulation are checked with the OPERA data. A sample of 19505 contained neutrino interactions corresponding to  $17.97 \times 10^{19}$  protons on target (pot) have been registered by the OPERA detector after 5 years data tacking.

The numbers of analyzed events are summarized in Table 3.6.  $0\mu$  events contain the signals of  $\tau \rightarrow e$ ,  $\tau \rightarrow 1h$ , and  $\tau \rightarrow 3h$  decay channels.  $1\mu$  events contain the  $\tau \rightarrow \mu$  decay channel. Most of the signal events occur at low muon momentum, thus a muon momentum cut at 15 GeV/c was introduced to accelerate the finding of signal for  $\nu_\mu \rightarrow \nu_\tau$  oscillations.  $1\mu$  numbers are quoted as a reference sample and the  $0\mu$  numbers demonstrate the sample that are interested for electrons.

### 3.4. Event Location and Decay Search Efficiency Assessment

	$\nu_\mu^{CC} \xrightarrow{mis} \nu_\mu^{NC}$
ED Trigger	$1 \pm 0$
Event Classification	$0.097 \pm 0.007$
OpCarac	$0.091 \pm 0.006$
BF	$0.082 \pm 0.006$
CS	$0.076 \pm 0.005$
SB	$0.063 \pm 0.006$

Table 3.4 – Event location and DS efficiency for  $\nu_\mu^{CC} \xrightarrow{mis} \nu_\mu^{NC}$  channel for 2008 and 2009 data selection. It is because of the misidentification of the muon track for  $\nu_\mu^{CC}$  events. The uncertainties are due to statistical errors.

	$\nu_\mu^{CC} \xrightarrow{mis} \nu_\mu^{NC}$
ED Trigger	$1 \pm 0$
Event Classification	$0.097 \pm 0.007$
OpCarac	$0.091 \pm 0.006$
BF	$0.054 \pm 0.005$
CS	$0.048 \pm 0.005$
SB	$0.042 \pm 0.005$

Table 3.5 – Event location and DS efficiency for  $\nu_\mu^{CC} \xrightarrow{mis} \nu_\mu^{NC}$  channel for 2010, 2011 and 2012 data selection. The uncertainties are due to statistical errors.

	2008	2009	2010	2011	2012	Total
0 $\mu$ events found with ED	283	587	434	497	348	2149
Located 0 $\mu$ events	149	251	213	239	165	1017
0 $\mu$ data location efficiency	53%	43%	49%	48%	47%	47%
1 $\mu$ events found with ED	1150	2298	1265	1390	1107	7210
Located 1 $\mu$ events ( $ p_\mu  < 15$ GeV/c)	819	1567	828	814	654	4682
1 $\mu$ data location efficiency	71%	68%	65%	59%	59%	65%
Total located events	968	1818	1041	1053	819	5699

Table 3.6 – The summary of event location for OPERA data.



# 4 Energy Estimation of Electromagnetic Showers

## 4.1 Purposes of this Analysis

The main aim of OPERA experiment is to search for the  $\tau$  leptons produced by oscillated  $\nu_\tau$  interactions. The physics program of OPERA regarding the neutrino oscillations is complemented with the search for  $\nu_\mu \rightarrow \nu_e$  oscillations. Although the experiment is not optimized for that and therefore the sensitivity to this channel cannot compete with dedicated experiments.

A good electromagnetic shower reconstruction is important for the  $\tau$  detection in the  $\tau \rightarrow e$  decay channel and also for the  $\nu_\mu \rightarrow \nu_e$  oscillations study, to detect the electron in the  $\nu_e^{CC}$  interactions.

The work done in this thesis is focused on the study of both  $\tau \rightarrow e$  decay channel and  $\nu_e^{CC}$  interactions. In particular, it is to construct an algorithm with improved performances to evaluate the energy of electrons through the identification of its shower for special events, using the OPERA brick as a calorimeter. The algorithm currently used by the collaboration was developed to reconstruct the electromagnetic shower and to estimate its energy for all events. Because the algorithm is intended for all events, the energy measurement could not benefit of a detailed analysis of the single electrons building up the shower. Thus, it had to be developed in an environment with a worse signal to noise ratio. The previous algorithm selects the tracks of the shower if their positions are inside a structure made of a cone, having the vertex in the primary electron position and with an opening angle of 20 mrad, followed by a cylinder, having a radius of 800  $\mu m$ . This stringent selection is due to the relatively large background given also the absence of any visual inspection of the involved tracks. This method could not perform an energy estimation with a resolution better than 30%.

The algorithm developed in this work uses larger values of the geometrical parameters for the cone definition and the Boost Decision Tree method, by the TMVA toolkit, to get a better Signal/Background separation.

In fact, the OPERA brick can be considered as a electromagnetic calorimeter where nuclear

emulsions inside the brick act as active detector and lead plates as passive target. When an electron is produced in  $\tau \rightarrow e$  decay or by  $\nu_e$  interactions, its electromagnetic shower will be detected in the emulsions. Accordingly, the electromagnetic shower produced inside the brick will be detectable through the tracks left by electrons and positrons in the emulsion films downstream of the vertex.

The main idea of this thesis is to develop a tool for estimating the energy of electromagnetic showers using two consecutive ECC bricks and optimizes the energy measurement of electromagnetic showers in one brick. The standard reconstruction of an electromagnetic shower can be applied only to those fully contained in one brick. However, when a shower is initiated in the downstream portion of the brick, the shower will begin in the first brick, pass through the Electronic Detector (ED) and end in the second brick; making normal reconstruction methods unusable. We present a new algorithm aimed to analyze showers involving one or two bricks along the beam direction.

Although each  $\gamma$  particle within the electromagnetic shower produces an electron and a positron but the process to reconstruct the base-tracks in the bricks' emulsion foils and applying the specific cuts (see Section 4.2) rejects the low momentum particles having the energy lesser than 30 MeV. Discarding these low momentum particles gives a linear relationship advantage between the number of tracks related to electromagnetic shower inside the brick and the energy of the electron.

The process of the energy measurement of the electromagnetic showers will be explained in the following sections and it will consist of the following steps:

- the track reconstruction inside the brick;
- definition of the geometrical parameters to reconstruct the electromagnetic shower;
- background estimation;
- development of the energy calibration procedure.

The algorithm has been developed using Monte Carlo simulations of both  $\tau \rightarrow e$  decay channel and  $\nu_e^{CC}$  interactions inside the OPERA detector. Furthermore, this work is performed on a sample of events where the brick containing the neutrino interaction is correctly identified by the brick finding algorithm, as described in section 3.2.3.

## 4.2 Basetrack Construction

After scanning the OPERA emulsions film, the basic unit of output data is a micro-track. In the general scanning mode all micro-tracks within a given angular range are searched for, however in the scanback mode, solely the well-defined positions and angular areas are considered. As

shown in Figure 4.1, a base-track is formed by connecting the two corresponding micro-tracks found in the two emulsion layers. Base-tracks are built when an acceptable agreement in slope and position of micro-tracks is found.

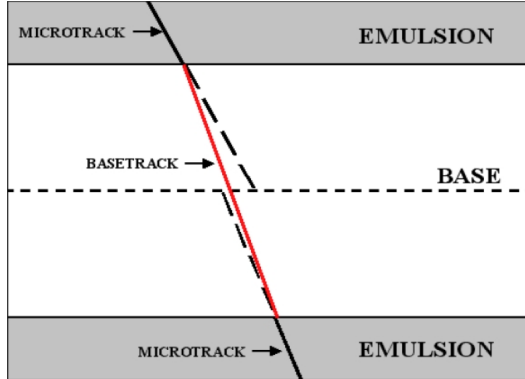


Figure 4.1 – The principle of base-track reconstruction: the micro-tracks matching are obtained when an acceptable agreement in slope and position is found. Joining the two points closer to the base forms the base-track.

The base-tracks produced by low momentum particles have been discarded in order to reproduce what is done in the data. In principle, for low momentum particles the angular and position deviations of the micro-tracks within two emulsion layers are quite large to form the base-tracks. Then, the base-tracks are investigated by a quality estimator of the micro-track angular agreement, so-called  $\chi^2$ , defined as:

$$\chi^2 = \frac{1}{4} \left[ \left( \frac{\Delta S_{tra}}{\sigma_{tra}} \right)_{top}^2 + \left( \frac{\Delta S_{lon}}{\sigma_{lon}} \right)_{top}^2 + \left( \frac{\Delta S_{tra}}{\sigma_{tra}} \right)_{bot}^2 + \left( \frac{\Delta S_{lon}}{\sigma_{lon}} \right)_{bot}^2 \right], \quad (4.1)$$

where  $\Delta S_{tra}$  and  $\Delta S_{lon}$  are the angular differences between the slope of the top (bottom) micro-track and the corresponding base-track calculated in the transverse and longitudinal planes, respectively. The  $\sigma_{tra}$  is the transverse resolution and has a value of 10 mrad for OPERA data analysis, while the longitudinal resolution,  $\sigma_{lon}$ , is given as:

$$\sigma_{lon} = (1 + 4 \tan \theta) \sigma_{tra}, \quad (4.2)$$

where  $\theta$  is the 3D slope of the top (bottom) micro-track. In order to remove the background base-tracks in a more effective way and in the other hand to minimize the signal loss, the cut

$$\chi^2 < 2.5 \quad (4.3)$$

is applied in the measurements reported in the following. As mentioned before, the low momentum particles have large  $\chi^2$  and therefore, this cut discards all particles having the energy lesser than 30 MeV. A typical  $\chi^2$  distribution is shown in Figure 4.2.

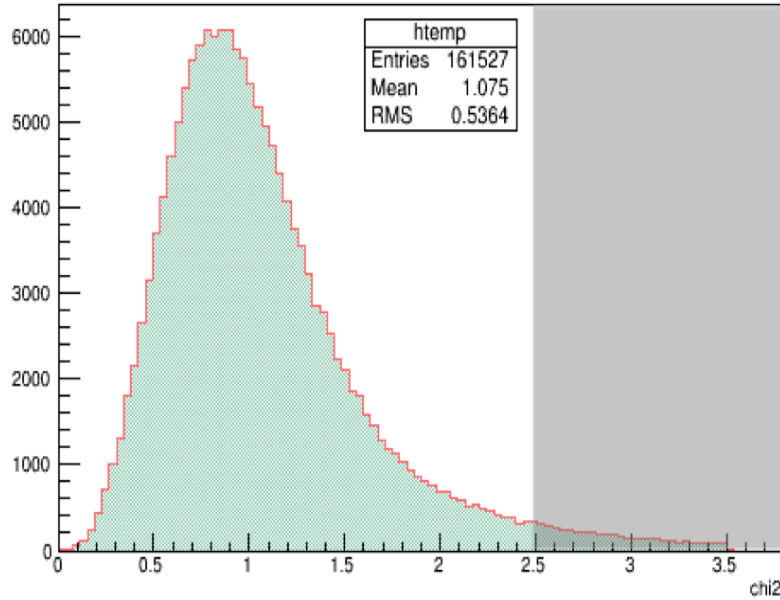


Figure 4.2 – Base-track  $\chi^2$  distribution for the MC signal with the cut  $\chi^2 < 2.5$ .

## 4.3 Shower Reconstruction in ECC Bricks

### 4.3.1 Passage of particles inside the matter

The simplified description of the development of electromagnetic showers was first developed by Heitel and Rossi [119]. There are two high-energy ( $E > 100$  MeV) electromagnetic energy loss mechanisms through which the electromagnetic cascade is propagated. Electrons and positrons lose energy by bremsstrahlung radiation as shown in Figure 4.3, photons degrade by pair production as shown in Figure 4.4.

Figure 4.4 shows photon total cross sections as a function of energy in lead, showing the contributions of different processes:  $\sigma_{p.e.}$  is the atomic photoelectric effect (electron ejection, photon absorption);  $\sigma_{Rayleigh}$  shows the Rayleigh (coherent) scattering-atom neither ionized nor excited;  $\sigma_{Compton}$  is the Compton scattering of an electron;  $\kappa_{nuc}$  shows the pair production for nuclear field;  $\kappa_e$  shows the pair production for electron field.

An electromagnetic shower extends inside the matter both longitudinally and laterally. A two-dimensional model of the electromagnetic shower is shown in Figure 4.5.

### 4.3. Shower Reconstruction in ECC Bricks

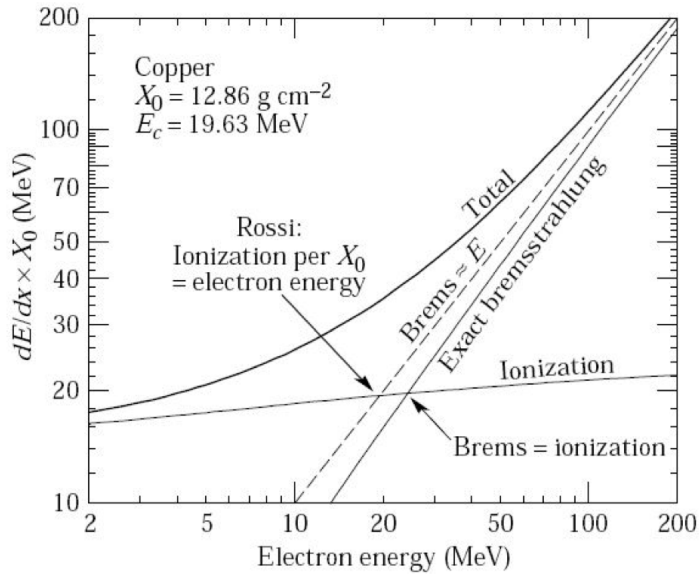


Figure 4.3 – Energy loss mechanism for electrons and positrons in copper. Above the “critical energy” the main mechanism is the emission of bremsstrahlung radiation.

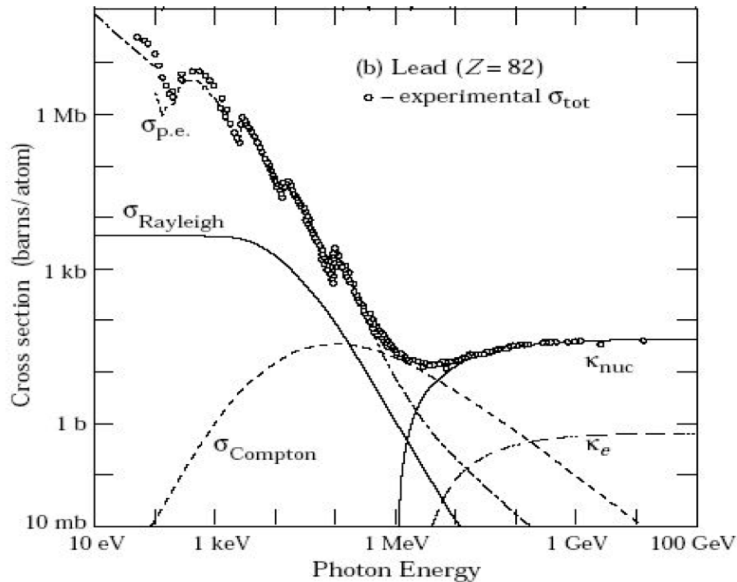


Figure 4.4 – Cross section for the interactions of photons in lead. At high energies ( $> 10 \text{ MeV}$ ) the main contribution is pair production [120].

The mean free path between collisions, or so-called radiation length, defines the longitudinal

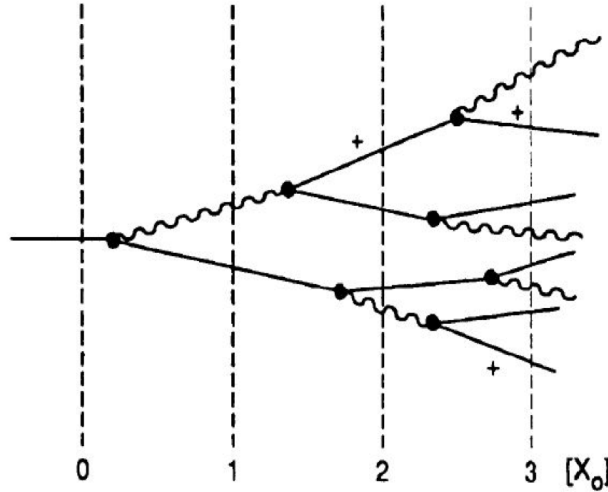


Figure 4.5 – Two-dimensional model of an electromagnetic shower. Two processes, bremsstrahlung and pair production are responsible for the energy degradation and the shower development.

dimension of an electromagnetic shower and describes as

$$E_{radiation} = E \exp^{-X/X_0}, \quad (4.4)$$

where  $X_0$ , the radiation length [121], is the length which the energy reaches the  $1/e$  of its initial value. The maximum propagation of an electromagnetic shower inside the mater, is given by:

$$X_{max} = \frac{\log(E/E_c)}{\log 2} X_0, \quad (4.5)$$

where  $E$  is the energy of parent electron and  $E_c$  is the critical energy. The shower is going on until the energy of the components in the shower reaches the critical energy when further multiplication stops. The value of  $E_c$  [122] for solids and liquids, roughly defines as

$$E_c = \frac{610}{Z + 1.24} \text{ MeV.} \quad (4.6)$$

### 4.3. Shower Reconstruction in ECC Bricks

The lateral dimension of the shower inside the different materials is independent from the energy of parent electron and it's defined with the Moliere radius  $R_M$ , given by [123, 124]

$$R_M = 21.2 \frac{X_0}{E_c} \text{ MeV}, \quad (4.7)$$

expressed in unit of  $X_0$  when  $E_c$  is in MeV. In case of OPERA, where the effective mass is composed of lead,  $E_c = 7.79 \text{ MeV}$ ,  $X_0 = 0.56 \text{ cm}$  and  $R_M = 1.52 \text{ cm}$ .

Each  $\gamma$  particle within the electromagnetic shower produces an electron and a positron. Therefore the number of produced  $e^- e^+$ 's particles increase exponentially for the electrons with higher energies. However, due to the base-track reconstruction procedure in the bricks' emulsion foils (as discussed in the previous Section) the low momentum particles in the electromagnetic shower having the energy lesser than 30 MeV will be discarded. Discarding the low momentum  $e^- e^+$ 's particles gives a linear relationship advantage between the number of base-tracks related to electromagnetic shower and the energy of the electron. A schematic view of an electromagnetic shower inside an OPERA brick is shown in Figure 4.6.

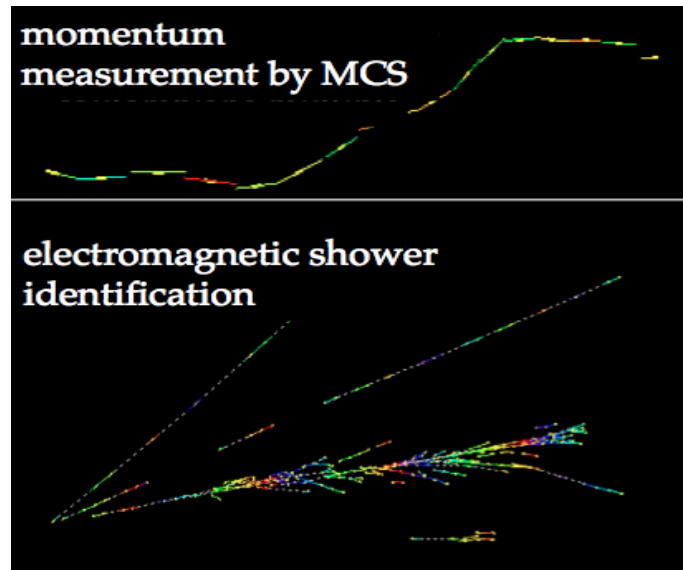


Figure 4.6 – A schematic view of electromagnetic shower reconstruction within the brick.

### 4.3.2 Selection of the signal

To reconstruct an electromagnetic shower inside the ECC brick, the following requirements have to be satisfied:

- a good efficiency in collecting the base-tracks belonging to the shower;
- random matches with background base-tracks must be avoided.

The definition of the geometrical parameters for the electromagnetic shower selection and the background analysis will be explained in the following sections.

The developed algorithm, selects all the base-tracks related to the shower within a cone starting from the decay vertex position of  $\tau$  in the  $\tau \rightarrow e$  decay channel; and with the axis, coincident with the direction of the electron. In principle, the cone will be used as a fixed volume to reconstruct the conical shape of the electromagnetic shower during the propagation.

### 4.3.3 Background Evaluation

When an electromagnetic shower propagates inside the ECC brick, the energy estimation of its shower will be done by counting the number of the produced base-tracks inside the electromagnetic shower. Therefore, the rejection of background is an important task in this analysis. There are two background sources inside the brick: the physical background and the instrumental background.

**The physical background** the  $\pi^0$  production is associated to the presence of 2  $\gamma$ 's from  $\pi^0 \rightarrow \gamma\gamma$ . The two gammas produce electromagnetic showers. When these electromagnetic showers overlap with the shower produced by the electron, they are defined as physical background and spoil the energy resolution.

**The instrumental background** is mainly related to the uncorrelated grains that randomly are produced inside the OPERA emulsion films. These grains create some fake tracks during the base-tracks reconstruction process and behave in a way to hide the real base-track grains. The instrumental backgrounds accumulate a large amount of background due to the ambient radioactivity and cosmic rays, and cannot be distinguished from the real particle tracks.

For the first case, due to the momentum conservation, electromagnetic showers generated by gammas are off-axis with respect to the electron shower. The physical background could be discarded by well defining the value of the  $\alpha_{cone}$ . It is obvious that the number of base-tracks inside the cone is dependent on the angle of the cone. Then, this angle should be large enough

to well select the base-tracks produced in the shower; and it should not be so large to reduce backgrounds.

To optimize the angle of the cone, the efficiency of the selection of base-tracks is calculated as the ratio of the number of selected base-tracks for a specific angle of cone over the total number of base-tracks related to the shower. The efficiency of the base-track selection increases until it reaches a plateau, where more or less all the base-tracks related to the electromagnetic shower are selected, as shown in Figure 4.7.

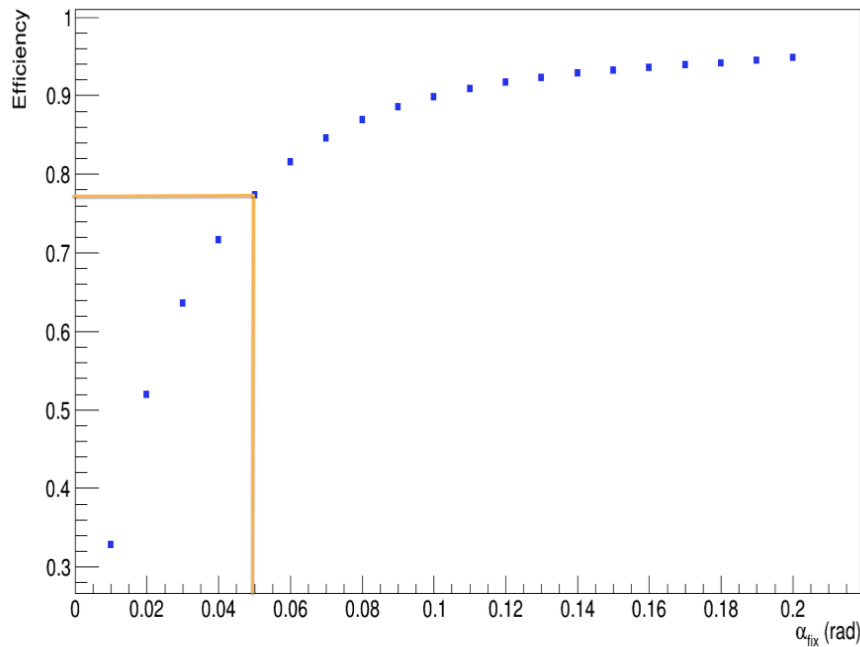


Figure 4.7 – Fraction of selected base-tracks as a function of the opening angle of the cone.

With fixing the angle of the cone as  $\alpha_{cone} = 50$  mrad, the contamination of the electromagnetic showers produced by gammas, physical background, is evaluated to be smaller than 1 %. This allows to select about 80% of tracks related to electromagnetic shower in our selection.

In addition to this, the rejection of the instrumental background in this analysis is extremely important. This background could be discarded by processing an eye-check procedure. However, dealing with a huge amount of background base-tracks inside the ECC brick, makes this procedure very long and sometimes impossible. Thus, to understand the behavior of background base-tracks in this work and to discard them automatically, an in depth study regarding the instrumental background has been done. To discard this background, the Boosted Decision Trees (BDT) method has been used by using the TMVA toolkit. This method is described in details in section 4.3.5.

#### 4.3.4 Variables

As also mentioned before, the OPERA brick acts as a colorimeter. To estimate the background, an empty volume without any neutrino interaction has been scanned and analyzed. The behavior of signal is studied by simulating the electromagnetic showers with the Monte Carlo simulation.

The following variables are separately calculated for the signal and background base-tracks inside the cone opened in the brick.

- 1)  **$\alpha$  angle for each base track:** once the axis of the cone is defined, each base-track inside the cone make an angle with respect to the axis of the cone by connecting the base-track with the cone vertex, as it's shown in Figure 4.8.

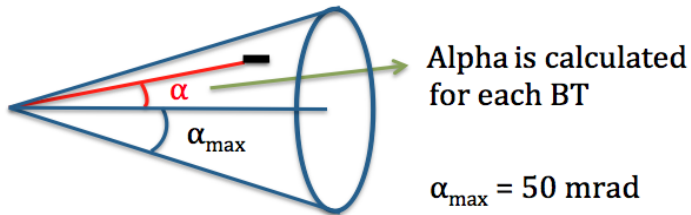


Figure 4.8 – Alpha definition for each base-track inside the cone.

Furthermore, Figure 4.9 shows the  $\alpha$  distribution for the signal. An 1/5 fraction of signal base-tracks is below 50 mrad. Indeed, the produced base-tracks by electron have higher momentum and therefore they propagate mostly around the direction of the electron until they lose their energy. However, the background base-tracks are uncorrelated and thus the fraction of the base-tracks within a given angle increases with the angle.

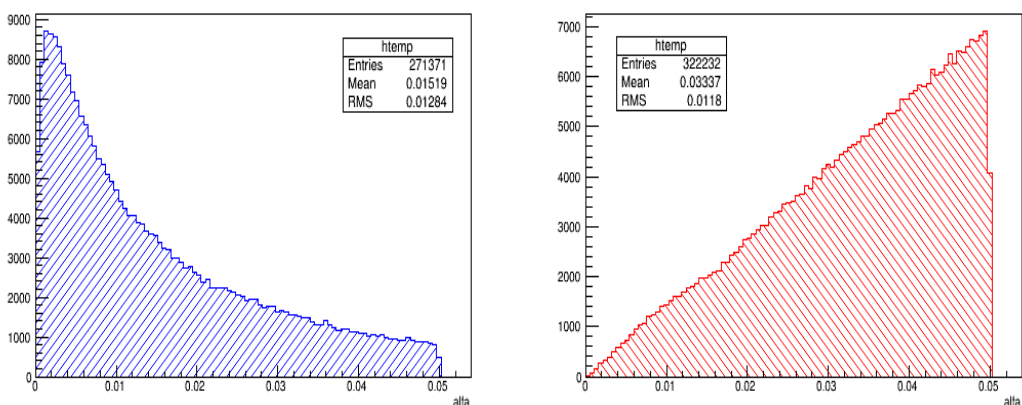


Figure 4.9 – The value of "alpha" angle; Left: Signal, Right: Background.

**2) Impact parameter:** the next parameter, that is used in this work, is the impact parameter, IP, for each base-track. In fact, IP is the distance between the vertex position and the projection of each base-track on the transfer plane of vertex, see Figure 4.10, and is defined as:

$$IP = \sqrt{(X_{ver} - X_{proj})^2 + (Y_{ver} - Y_{proj})^2}, \quad (4.8)$$

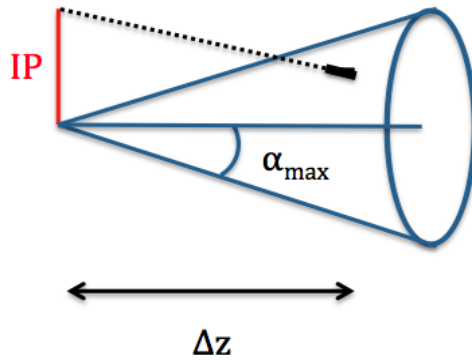


Figure 4.10 – The impact parameter, IP, calculated for each base-track

where  $X_{ver}(Y_{ver})$  is the position of the cone vertex and  $X_{proj}(Y_{proj})$  is the position of the extrapolation of each base-track on the vertex plane, where the shower originates.  $X_{proj}$  and  $Y_{proj}$  are defined as:

$$X_{proj} = X - (\Delta Z \times S_x), \quad (4.9)$$

$$Y_{proj} = Y - (\Delta Z \times S_y), \quad (4.10)$$

where  $X(Y)$  is the position of each base-track,  $\Delta Z$  is the longitudinal distance between the position of related base-track and the cone vertex and  $S_x(S_y)$  is the slope of each base-track in the X (Y) projection.

The calculated IP for each base-track is divided by its distance from the vertex position,  $\Delta Z$ . In case of signal, base-tracks closer to the vertex have smaller IP. However, the IP for the background base-tracks is independent on the distance from the vertex. Therefore, dividing the IP by  $\Delta Z$  gives more power to improve the signal/background separation.

The distribution of impact parameter divided by the  $\Delta Z$  for signal and background base-tracks is shown in Figure 4.11.

Signal base-tracks have smaller  $IP/\Delta Z$  however this value for the background base-tracks increases with the angle. The drop of the  $IP/\Delta Z$  distribution for the background above 0.5 is

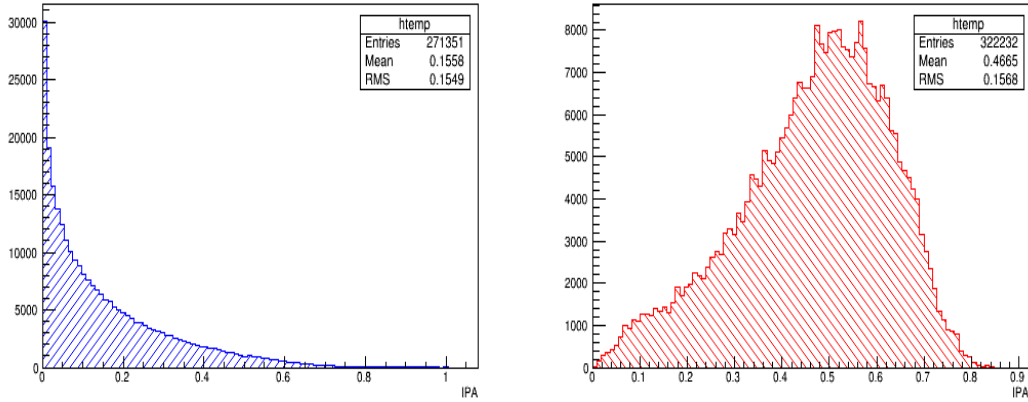


Figure 4.11 – The value of " $\frac{IP}{\Delta Z}$ "; Left: Signal, Right: Background.

due to the acceptance of the brick.

**3, 4) Angular difference of base-tracks in both X and Y projection:** the next parameters that are used in this analysis are the angular difference between the slope of each base-track inside the cone and the slope of the first base-track of electron ( $S_{e_x}$  and  $S_{e_y}$ ) for both X,  $\Delta S_x$ , and Y,  $\Delta S_y$ , projection:

$$\Delta S_x = S_{e_x} - S_x, \quad (4.11)$$

$$\Delta S_y = S_{e_y} - S_y. \quad (4.12)$$

The distribution of  $\Delta S_x$  and  $\Delta S_y$  for the signal and background is shown in Figure 4.12.

For the signal base-tracks the angle of secondary electrons/positrons is correlated to the primary electron, therefore this angular difference for signal base-tracks is small. For the background base-tracks the angular difference in slopes are independent on the electron slopes and is constant.

**5)  $\chi^2$ :** the last parameter used in this analysis is the quality estimator,  $\chi^2$ , in the reconstruction of the base-tracks. As described at Section 4.2, the reconstruction of base-tracks inside the emulsion films depends on their micro-track angular agreement. The low momentum particles have larger  $\chi^2$ .

Figure 4.13 shows the  $\chi^2$  distribution for the signal and background base-tracks.

### 4.3. Shower Reconstruction in ECC Bricks

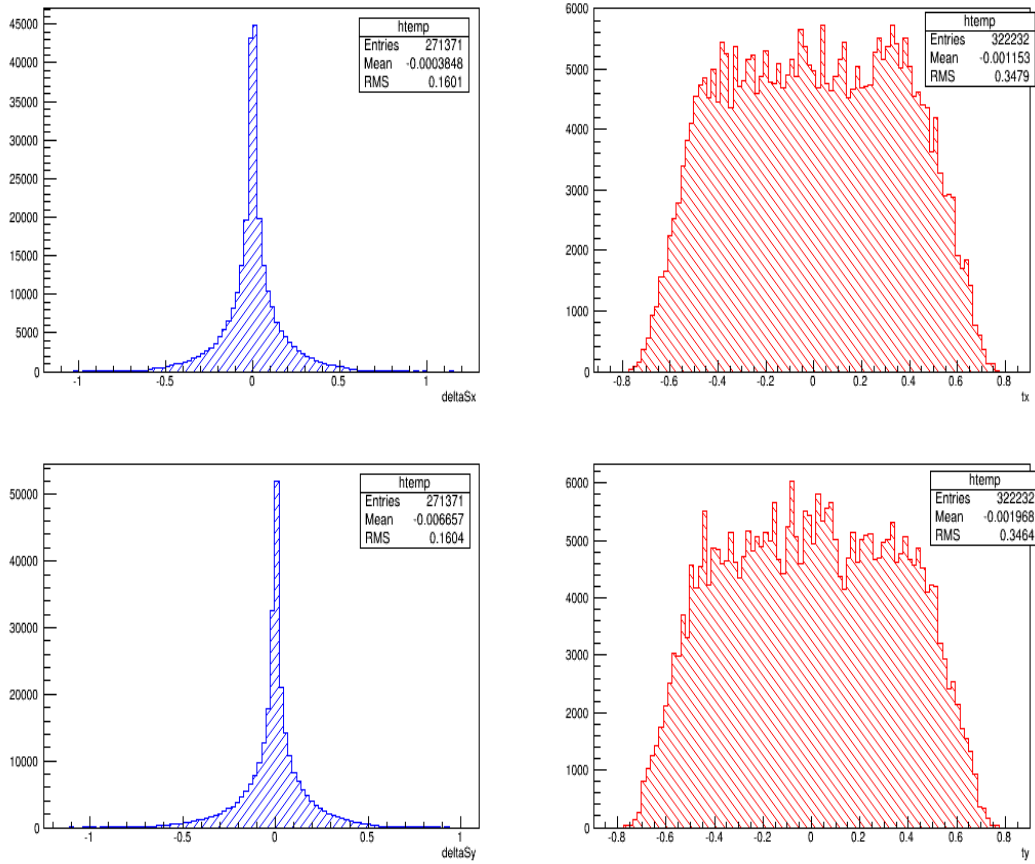


Figure 4.12 –  $\Delta S_x$  and  $\Delta S_y$  distribution; Top Left:  $\Delta S_x$  for Signal, Top Right:  $\Delta S_x$  for Background, Bottom Left:  $\Delta S_y$  for Signal, Bottom Right:  $\Delta S_y$  for Background .

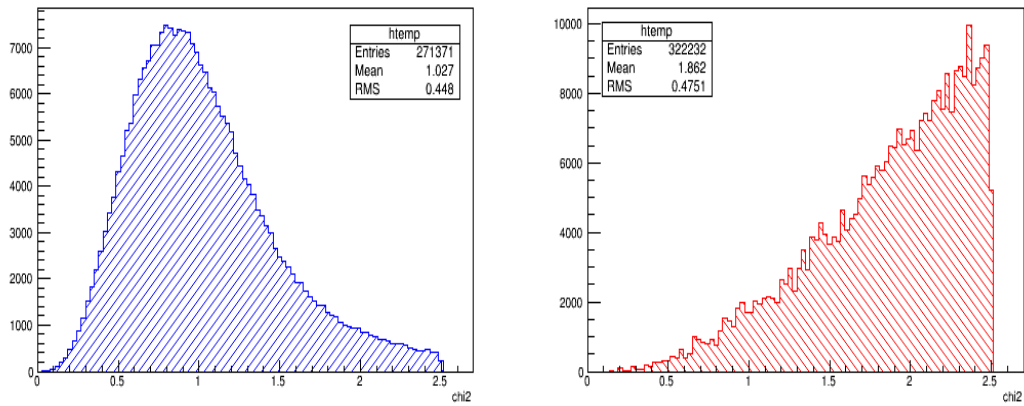


Figure 4.13 – The "χ<sup>2</sup>" distribution in the reconstruction of base-tracks; Left: Signal, Right: Background.

## Chapter 4. Energy Estimation of Electromagnetic Showers

---

By calculating all these variables for both signal and background, we have the possibility to effectively reject the background and also select the signal in a proper way. In the following section, the method used for the signal/background separation in this work is described.

### 4.3.5 Boosted Decision Tree

In order to reconstruct the electromagnetic shower and estimate its energy, a separation between signal and background is needed. Classically, this can be done by “cut-based analysis”. However in a Boosted Decision Tree (BDT) method, a “decision tree” algorithm determines the best-cut value for the variables. A decision tree is a binary tree structured classifier, see Figure 4.14.

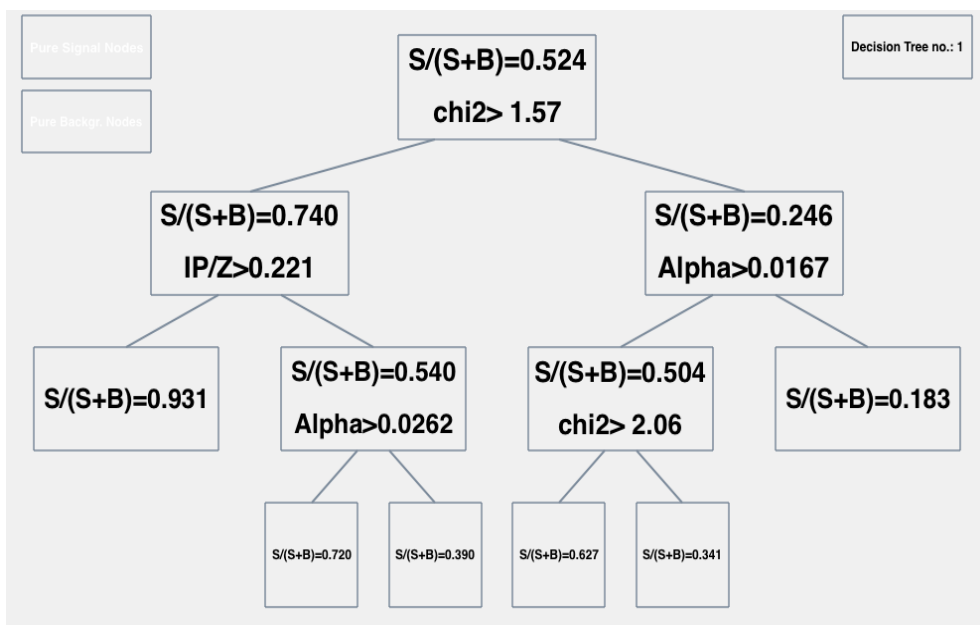


Figure 4.14 – A BDT as obtained from the TMVA toolkit. The tree is grown from a sequence of splits onto variables, to obtain the highest purity; for example in this tree the highest purity is  $P = 0.931$ .

To apply the BDT method, Monte-Carlo samples are equally divided into training and testing samples. This can be set by even/odd separation or it can be done randomly. As shown in Figure 4.14, the tree is grown by repeated true/false decisions until the final decision is taken, for being signal or background. The training sample is divided into many nodes; the split for each node is defined by assessing the cut values for the variables that gives the best signal over background separation. Depending on the majority of events in the final node (leaf), they are categorized as signal-like or background-like. After the training part, the BDT is applied to the testing sample in order to get the BDT response. The BDT response is a value between -1, which defines the background-like events, and +1, that defines the signal-like events.

While a single tree on its own improves upon a simple cut-based analysis, boosting significantly

increases the performance of this single tree. It also helps smooth distributions which may otherwise appear spiky due to features of a specific training sample when limited statistics are used. In general, the boosting process uses the training results of the first tree to increase the weights of candidates that were misclassified. A new tree is then trained using these weights. Boosting effectively re-weights candidates that the previous tree classified incorrectly in order to increase their importance during the next training. Terminal leaves are labelled either background or signal leaves according to a set purity threshold (often 0.5). Misclassification occurs when a candidate of one type (signal or background) terminates on a leaf of opposite classification. Using this boosting method, many trees are then trained with new weights calculated after each retraining. Therefore, the final classifier is given by averaging over all trees.

A decision tree is determined by function  $f(x, a_m)$ . The model response  $F(x, b_m, a_m)$  is a weighted sum (weights  $b_m$ ) over the main functions  $f(x, a_m)$ . The aim is to minimize the loss function

$$L(F, k) = (F(x, b_m, a_m) - k)^2, \quad (4.13)$$

the difference between the true value of  $k$  and the model response, with respect to the  $a_m$  and  $b_m$  parameters.

In the following, the evaluation of BDT method and its graphical and numerical results will be described.

**Input variable distribution:** the normalized distribution of all input variables for signal and background is calculated. An example is shown in Figure 4.15. This helps to understand how a variable could be effectively used for distinguishing between signal and background.

**Correlations between input variables:** TMVA toolkit provides two different ways to display the correlations between variables. One is a correlation matrix between variables, as shown in Figure 4.15 and the other one is a scatter plot. These plots are illustrated separately for signal and background samples.

**Receiver Operating Characteristic (ROC) curve:** the ROC curve describes the efficiency of the BDT method and displays the background rejection versus the signal efficiency, see Figure 4.15. A good ROC curve is in the upper right corner. Moreover, the integral over this curve gives a numerical statement. The BDT is more efficient as much as the numerical statement is closer to one.

**Overtraining check:** in order to understand the response of BDT for signal/background separation and also to know, how well a BDT can model the data, overtraining has to be checked. Overtraining check is done by checking the overlap between the distribu-

## Chapter 4. Energy Estimation of Electromagnetic Showers

tion of classifier for testing and training sample, as shown in Figure 4.15. To have no overtraining, a perfect overlap between testing and training sample is needed.

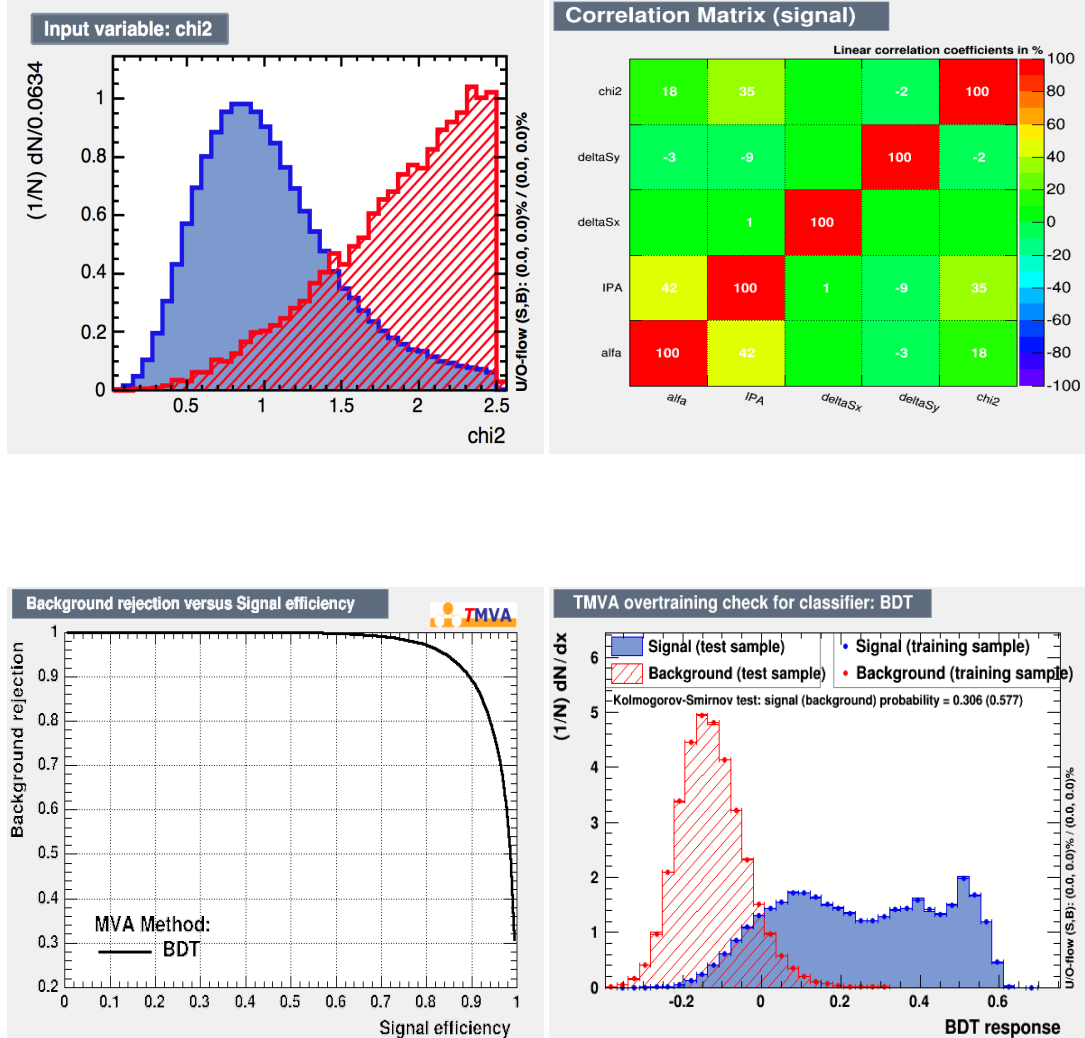


Figure 4.15 – BDT evaluation plots obtained via the TMVA toolkit; Top Left: Input variable distribution, Top Right: Correlation matrix, Bottom Left: ROC curve, Bottom Right: Overtraining check.

## 4.4 Energy Estimation by Using One or Two ECC Bricks

Reconstruction of electromagnetic showers is one of the fundamental tools needed by neutrino experiments and the estimation of their energy is a crucial issue. This is also true for the OPERA experiment where an algorithm has been well developed and tested, in order to evaluate the energy of electron through the identification of its shower for the  $\tau \rightarrow e$  decay channel by using the OPERA bricks. This algorithm could be used as an application for evaluating the

## 4.4. Energy Estimation by Using One or Two ECC Bricks

---

energy of electron in  $\nu_e^{CC}$  interactions as well as the showers produced by  $\gamma$ 's yielded from the  $\pi^0$  particles.

### 4.4.1 Definition of different zones within the Brick

In order to estimate the energy of electron by its shower, it is necessary to provide the relationship between the energy of electron and the number of base-tracks produced within its shower.

The number of base-tracks produced in the electromagnetic shower does not only depend on the energy of the electron but it's also affected by the geometrical position of the decay point of  $\tau$  lepton in the brick. Therefore, if the  $\tau$  lepton decays in the most upstream part of the brick, there is the possibility to reconstruct the electromagnetic shower inside the brick. However, for the decays occurring in the most downstream part of the brick, the electromagnetic shower will not be fully contained inside the brick because the major part of the shower will take place in the downstream brick. Hence, for the most downstream decays, the number of selected base-tracks will be consequently smaller.

This fact is shown in Figure 4.16 where the profile of the number of selected base-tracks related to the electromagnetic shower is plotted as the function of the decay point of  $\tau$  lepton inside each plate, on the longitudinal axis of the brick.

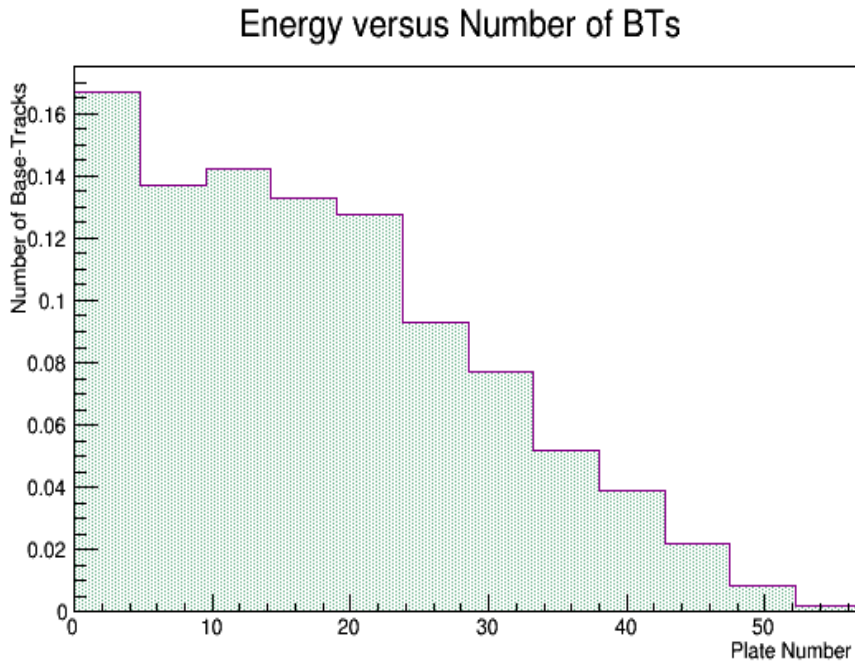


Figure 4.16 – Profile histogram of the number of base-tracks as the function of the decay point of  $\tau$  lepton inside each plate. Each plate corresponds to 1.3 mm thickness with 1 mm of lead. This plot is normalized to 1.

## Chapter 4. Energy Estimation of Electromagnetic Showers

---

Moreover, Table 4.1 gives the maximum length,  $X_{max}$ , of the electromagnetic shower inside the brick for different energies. As described before, OPERA bricks are mostly made of lead, with  $X_0 = 0.56$  cm and  $E_c = 7.79$  MeV.

Energy of parent electron (Gev)	1	2	4	10	20	30
Length (cm)	3.9	4.4	5.0	5.7	6.3	6.6

Table 4.1 – The length of the electromagnetic shower inside the OPERA bricks.

In addition to this, for those events with the  $\tau$  decay close to the lateral edge of the brick, the electromagnetic shower produced by its electron will partially take place in the brick and a part of shower will be inside its neighbor brick.

In the most upstream part of the brick the number of selected base-tracks is originally independent on the  $\tau$  decay point, because the shower is mostly contained in the brick volume. On the contrary, in the downstream part of the brick, this number gradually decreases as the vertex position gets closer to the downstream edge of the brick. The profile of the number of tracks reconstructed on the CS is given in Figure 4.17. The number of CS tracks is small in the most upstream part of the brick since the shower is fully contained in the brick. It achieves its maximum around the center of the brick and then decreases in the downstream part of the brick because the major part of the shower develops in the downstream brick.

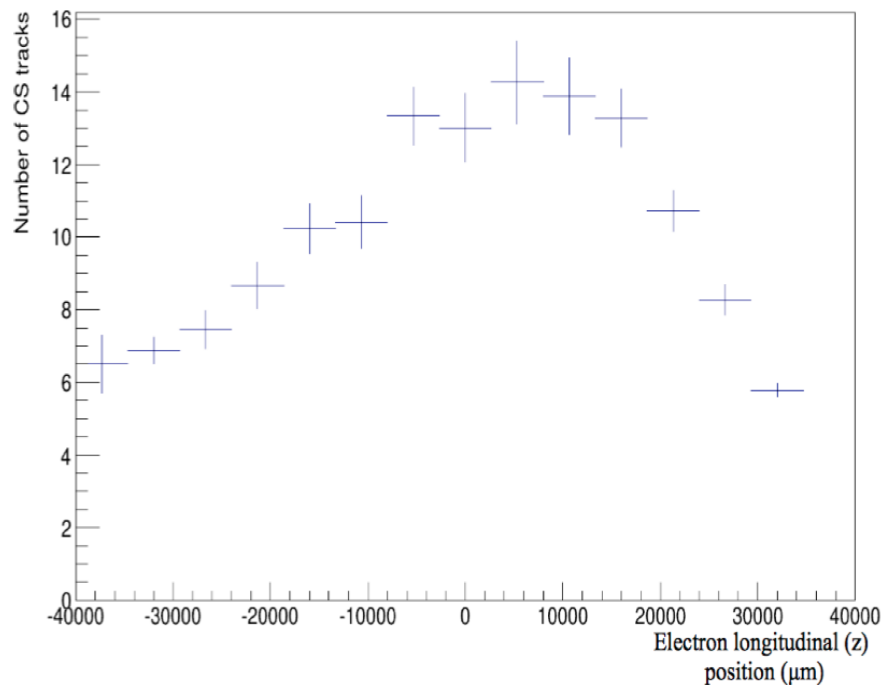


Figure 4.17 – Profile histogram of the number of tracks reconstructed in the CS as a function of the decat point of  $\tau$ .

#### 4.4. Energy Estimation by Using One or Two ECC Bricks

Therefore, in order to estimate the energy of electromagnetic showers, it is needed to first divide the ECC brick in different zones, as shown in Figure 4.18. The first region is defined in the first 21 films of the brick.

The showers occurring in this zone, so-called “Zone1”, have their shower fully reconstructed within the brick. Normal reconstruction of an electromagnetic shower depends upon the shower being contained in one brick. However, when a shower is initiated in the following zone, “Zone2” including 36 films, the shower will begin in the first brick, pass through the Electronic Detector (ED) and will end up in the downstream brick.

Therefore, to estimate the energy of the showers occurring in this zone, it's needed to move to use the downstream brick. In this work, an algorithm has been developed in such a way to analyze the electromagnetic showers within one or two bricks. This is the first time in OPERA experiment that the information of the downstream brick is used to reconstruct and to estimate the energy of electromagnetic showers.

Furthermore, in order to ensure the lateral containment of the shower, an additional requirement on the position of the decay point of  $\tau$  lepton has been defined: the transverse coordinate of the decay point should be at least one centimeter away from the lateral edge of the brick. Hence, this zone, “Zone3”, has been discarded for this analysis.

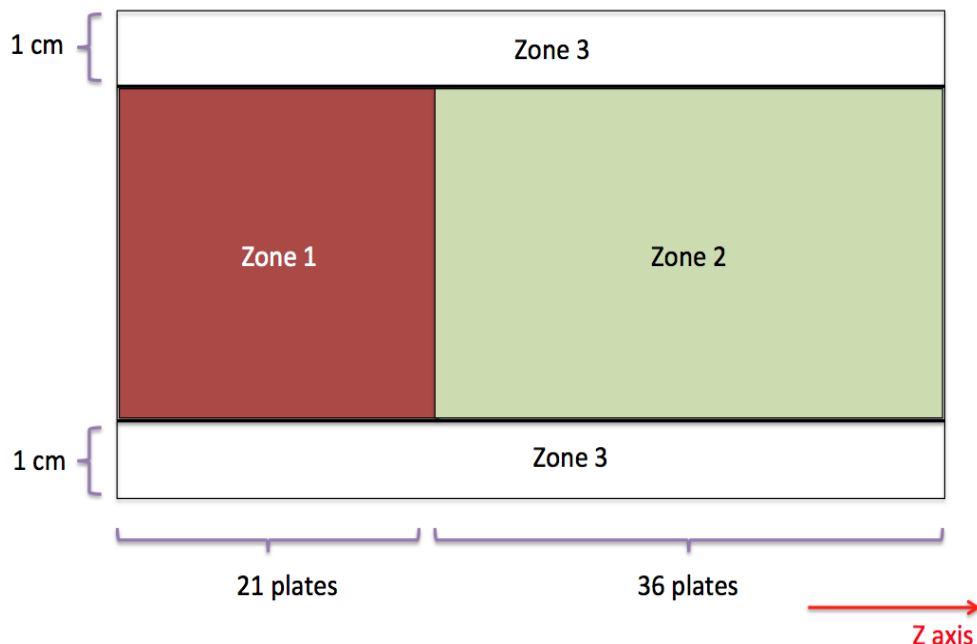


Figure 4.18 – A schematic view of the different regions defined in the brick.

In the following, the analysis of both Zone1 and Zone2 will be reported, separately.

#### 4.4.2 Events in Zone1

The performance of the energy estimation algorithm in this work is evaluated, for the  $\nu_\tau$  events in  $\tau \rightarrow e$  decay channel, on the Monte Carlo samples of 5000 events produced in an energy range from 0 to 60 GeV. Figure 4.19 shows the energy spectrum of electron in  $\tau \rightarrow e$  decay channel before introducing the oscillation probability of neutrinos.

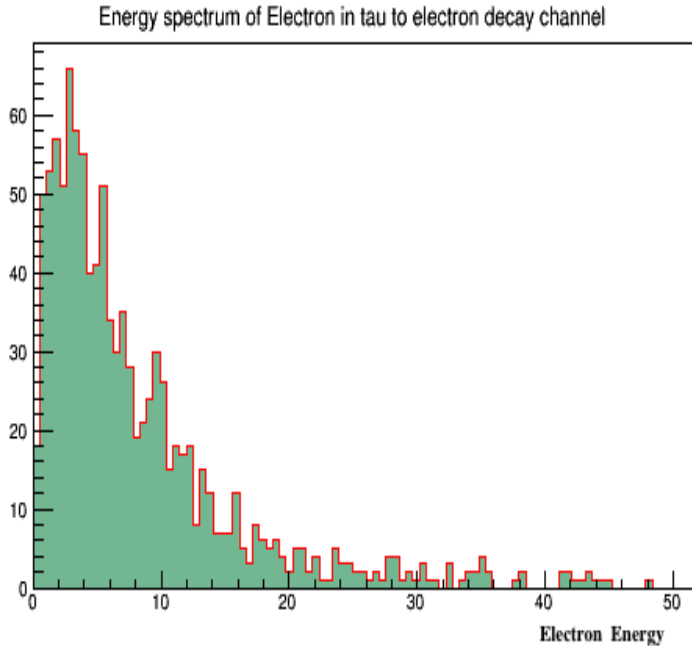


Figure 4.19 – Energy spectrum of electron in  $\tau \rightarrow e$  decay channel.

The first step of the analysis is done by defining a pure sample of electrons and positrons to assess the best performance in energy estimation of this tool. As mentioned before, the electrons and positrons produced in the shower are selected within a cone where its axis corresponds to the direction of electron and having a fixed angle of  $\alpha_{cone} = 50$  mrad. To estimate the background and apply it to Monte Carlo samples, a volume made of 57 OPERA emulsion films with no neutrino interaction inside has been analyzed. Moreover, the base-tracks produced during the transportation of the brick and also the base-tracks of cosmic rays integrated before the development of the brick have been discarded. The same geometrical cone is used for the background.

In order to discard the background, the relevant variables as determined in Section 4.3.4, have been calculated both for Signal and background and a Boosted Decision Tree (BDT) method is used to determine the best-cut value for the variables.

The five input variables is shown in Figure 4.20. These events are from the training sample only, which consists of half the background and half the signal simulation. In these Figures the background is shown in red and the signal in blue. TMVA also provides correlation matrices

#### 4.4. Energy Estimation by Using One or Two ECC Bricks

of all the input variables for signal and background. There is correlation between each set of variables used in the TMVA training. Ideally the correlation between variables is low, so that every variable contributes to the BDT decision without redundancy. The correlation matrix for both Signal and Background is shown in Figure 4.21. These confirm the low correlation between variables for both signal and background.

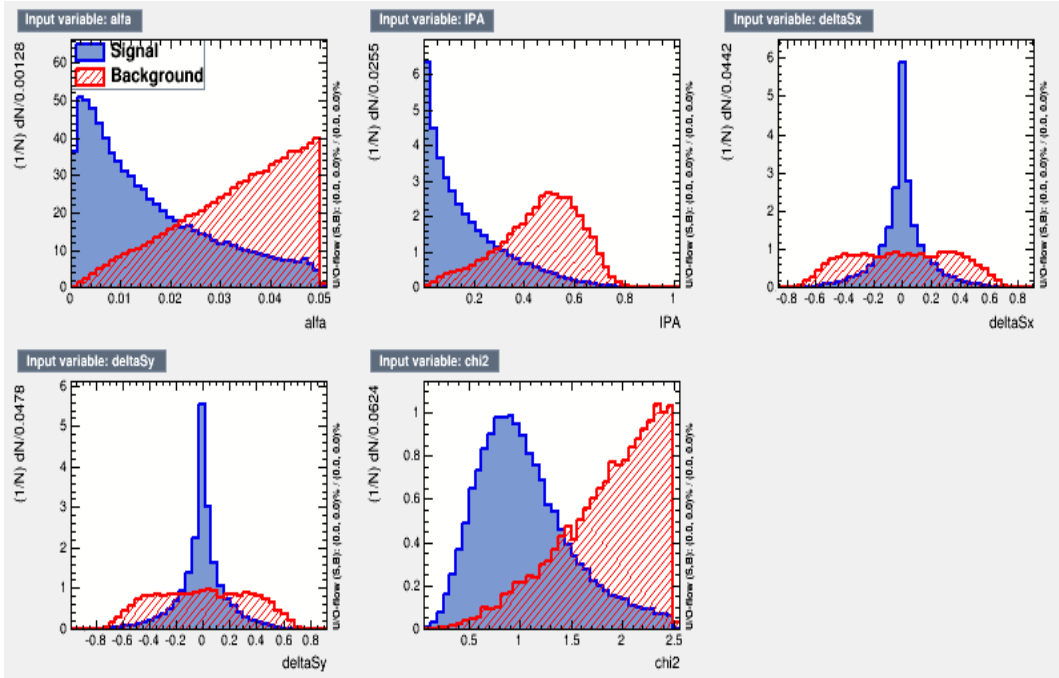


Figure 4.20 – The normalized distribution of the input variables. Signal distribution is shown in blue and the background distributions is in red; Top Left: Alpha distribution, Top Middle: Impact Parameter over  $\Delta Z$  distribution, Top Right: Angular difference in X projection, Bottom Left: Angular difference in Y projection, Bottom Middle:  $\chi^2$  distribution.

Having this information, the pure sample has been defined according to the efficiencies and the optimal cut value given by the BDT algorithm as shown in Figure 4.22. The background rejection is a crucial issue for a better energy estimation. Therefore, by selecting the signal tracks with a BDT response greater than 0.2, the program selects around 160 signal base-tracks and  $\sim 17$  background base-tracks on average per event .

Showers have been reconstructed over the full volume available for each event. Therefore, it is possible to determine the calibration curve between the energy of parent electron and the signal/background number of base-tracks selected by the BDT algorithm, having a BDT response greater than 0.2. The number of electron pairs produced in an electromagnetic shower grows approximately exponentially with the energy. Nevertheless, the request that

## Chapter 4. Energy Estimation of Electromagnetic Showers

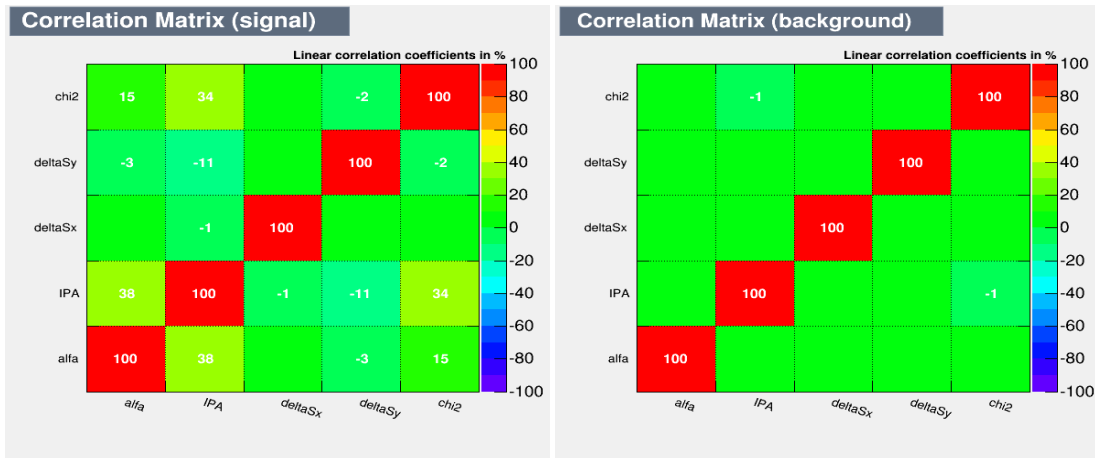


Figure 4.21 – The correlation matrix; Left: Signal, Right: Background.

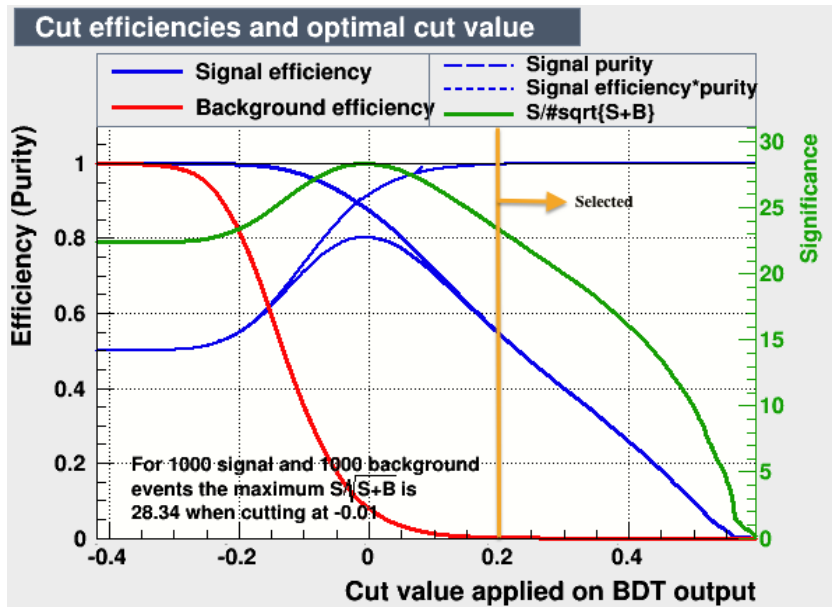


Figure 4.22 – The cut efficiencies and the optimal cut value coming out by BDT algorithm. The signal tracks having a BDT response greater than 0.2 are selected.

these pairs produce base-tracks in all the films implies a 30 MeV threshold which eliminates the very soft component and in turn it produces a rather linear dependence of the reconstructed tracks on the electron energy. Figure 4.23 shows a scatter plot of the linear dependency of the MC true energy as the function of the total number of base-tracks.

The linear relationship of the MC true energy and the total number of base-tracks works well up to 30 GeV, however for the higher energies this linear relationship is a bit spoiled because of the low statistic. This result is very good for our purpose since an upper cut on the neutrino energy at 20 GeV will be used in the analysis reported in chapter 5.

#### 4.4. Energy Estimation by Using One or Two ECC Bricks

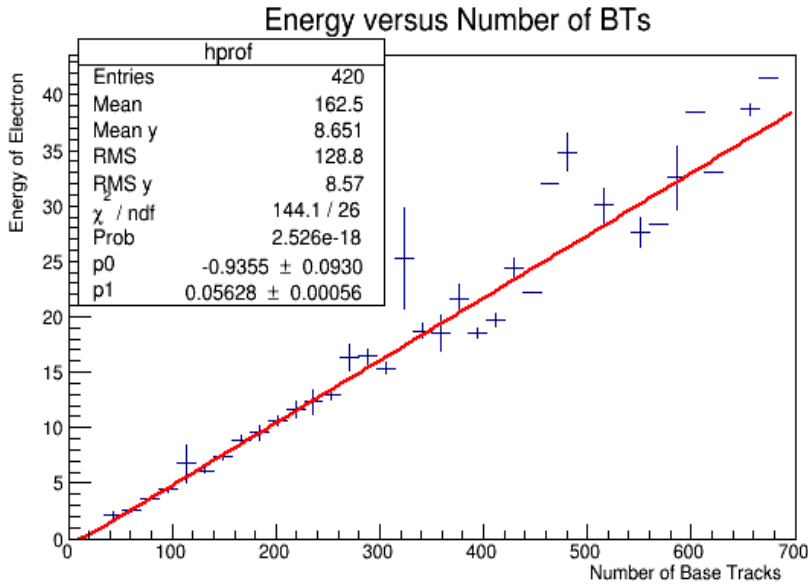


Figure 4.23 – The calibration curve of the energy as a function of the number of base-tracks for the Zone1 region.

The reconstructed energy equation is defined as:

$$E_{REC} = P_0 + P_1 * N_{BT}, \quad (4.14)$$

where  $E_{REC}$  is the reconstructed energy of the shower,  $N_{BT}$  is the number of selected base-tracks within the shower and the  $P_0$  and  $P_1$  are the intercept and the slope of the curve given by the fit, respectively. The parameterization of the reconstructed energy,  $P_0$  and  $P_1$ , for the Zone1 are defined as:

$$P_0 = (-0.9355 \pm 0.093) \text{ GeV}, \quad (4.15)$$

$$P_1 = (0.0563 \pm 0.001) \text{ GeV}, \quad (4.16)$$

consistent with zero within less than  $2\sigma$ .

## Chapter 4. Energy Estimation of Electromagnetic Showers

---

The energy resolution of this method is evaluated as:

$$\frac{\Delta E}{E} = \frac{E_{TRUE} - E_{REC}}{E_{TRUE}}, \quad (4.17)$$

where the  $E_{TRUE}$  is the MC true energy of the electron given by the Monte Carlo simulation.

Figure 4.24 shows the distribution of the reconstructed energy resolution,  $\Delta E/E$ , in the region of Zone1, integrated over the entire energy spectrum.

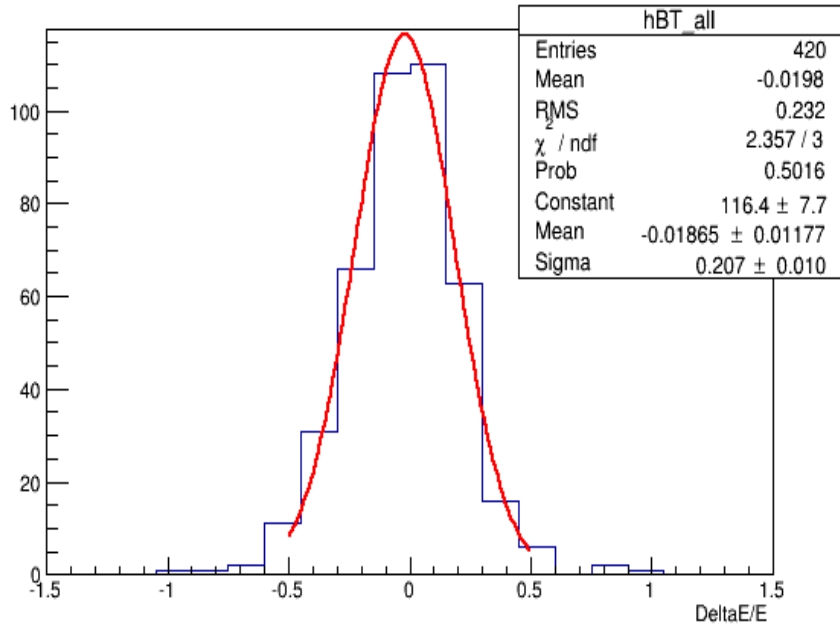


Figure 4.24 – The  $\frac{\Delta E}{E}$  distribution.

The fractional resolution,  $\sigma_E$ , is the sigma of the Gaussian fit of the relative difference:

$$\sigma_E = 0.207 \pm 0.010. \quad (4.18)$$

The energy resolution as a function of energy is shown in figure 4.25. As expected,  $\sigma_E$  improves with the energy. A fit using the relationship

$$\sigma_E = A_1 + \frac{B_1}{\sqrt{E_{REC}}} \quad (4.19)$$

#### 4.4. Energy Estimation by Using One or Two ECC Bricks

---

has been performed, giving:

$$A_1 = 0.28 \pm 0.09, \quad (4.20)$$

$$B_1 = 0.09 \pm 0.04. \quad (4.21)$$

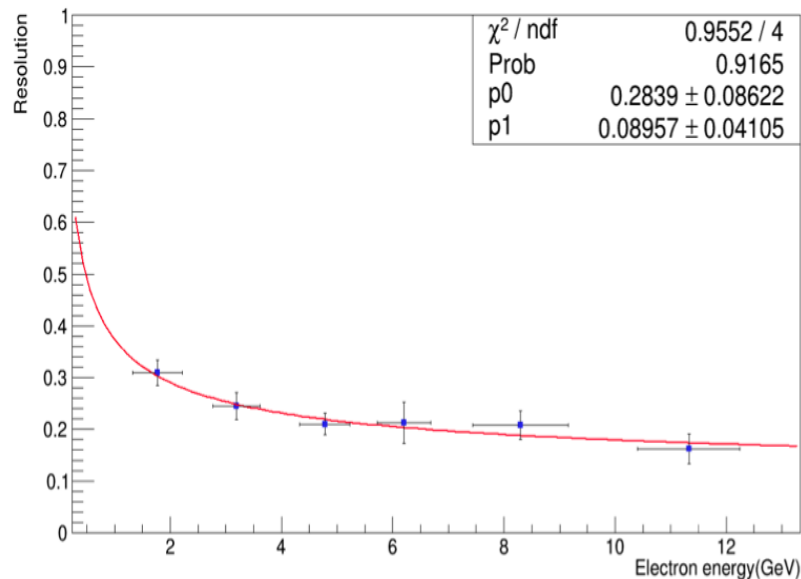


Figure 4.25 – The  $\sigma_E$  as a function of the electron energy.

#### 4.4.3 Events in Zone2

When a shower is initiated in the downstream portion of the brick, Zone2, the shower will develop within two ECC bricks; making the normal reconstruction methods unusable. Nearly half of the electromagnetic shower events detected take place across two bricks, meaning that previously, half of detected events had to be discarded. The algorithm has been expanded in such a way to analyze showers within two bricks, allowing us to include 50 percent more events in our data sets. Without existing the second brick, one should abandon the emulsions and use the target tracker in calorimeter mode with the lower resolution.

The process of selecting a pure sample of electrons and positrons in this zone is quite similar to the Zone1. We enlarge the geometry in the second brick to cover any possible misalignment. Therefore, the base-tracks produced in the shower occurred in Zone2 are selected within the same cone used in the previous zone with a fixed angle of  $\alpha_{cone} = 50$  mrad where its axis corresponds to the direction of the electron extrapolated until it reaches the second brick; 1 mm is added to account for misalignment before extrapolating along the second brick, as shown in Figure 4.26. The same geometrical cone is used for the background.

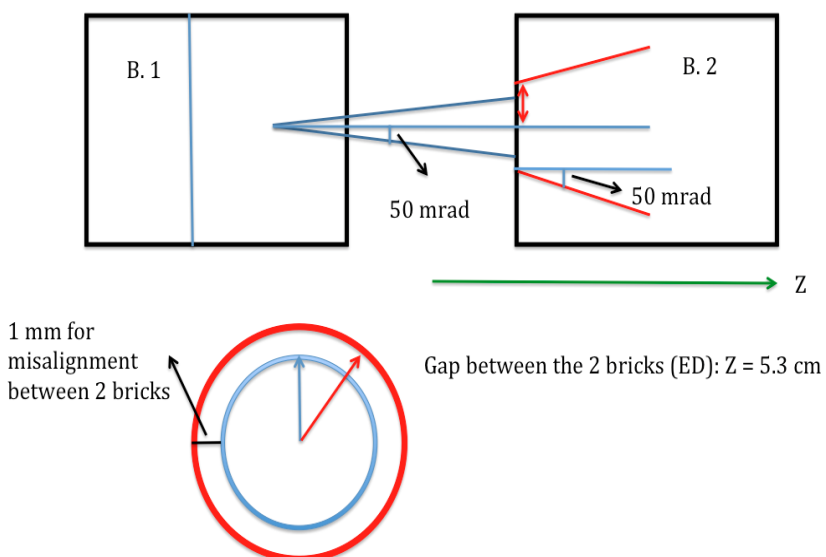


Figure 4.26 – The 2D schematic view of the electromagnetic showers reconstruction within two bricks.

The size of the Electronic Detector between the two bricks is around 5.3 cm and this makes the area to be analyzed larger in the downstream brick. Figure 4.27 shows the number of base-tracks of the showers within the second brick as the function of the number of plates. This plot shows that the number of base-tracks in the showers after around 20 plates is decreasing; however, the number of background base-tracks is strongly increasing. Therefore, Only the first 20 plates of the second brick are used in this work, see Figure 4.28.

#### 4.4. Energy Estimation by Using One or Two ECC Bricks

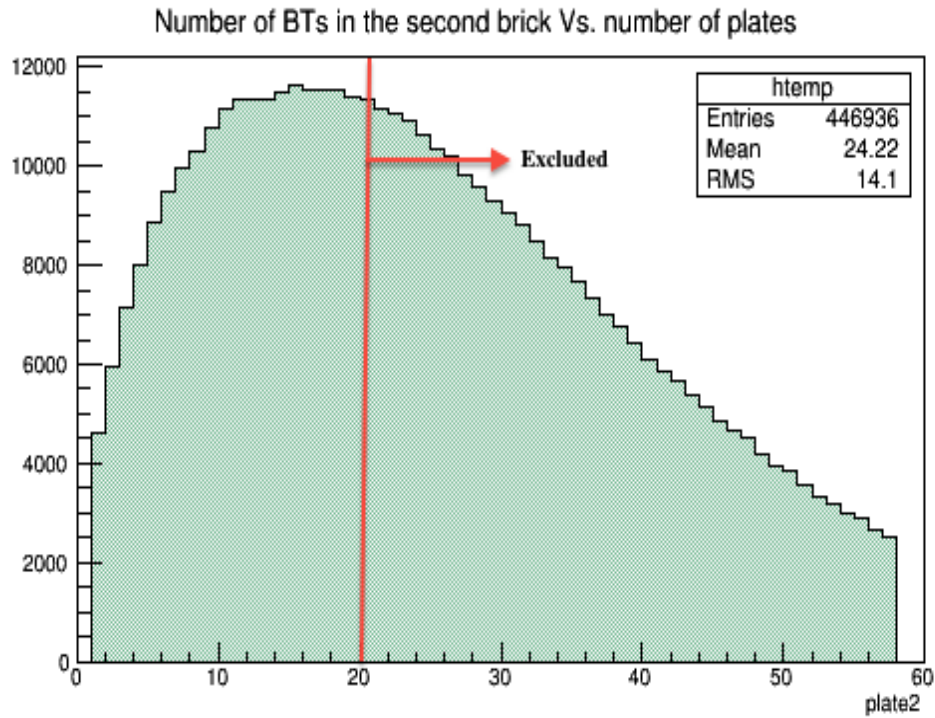


Figure 4.27 – Number of base-tracks of the showers within the second brick as the function of the number of plates.

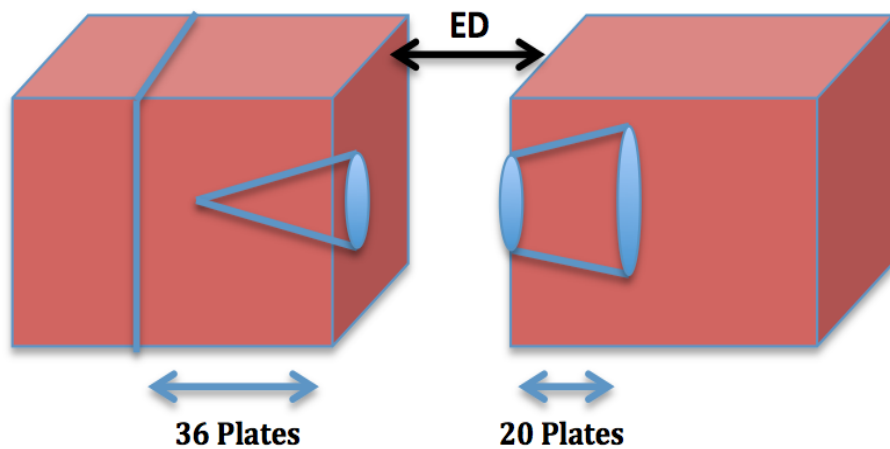


Figure 4.28 – The region used for the Zone2 analysis; only the first 20 plates of the second brick are used in this work.

## Chapter 4. Energy Estimation of Electromagnetic Showers

The same variables used for the Zone1 analysis have been calculated here both for Signal and background. The normalized distribution of the input variables for Zone2 is shown in Figure 4.29. The background and signal are scaled so that they are normalized to each other. In these Figures the background is shown in red and the signal in blue.

The correlation matrix for both Signal and Background is shown in Figure 4.30. There is correlation between each set of variables used in the TMVA training. Ideally the correlation between variables is low, so that every variable contributes to the BDT decision without redundancy. As shown in Figure 4.30, the correlation in both signal and background variables is low and flat over all pairings of the input variables.

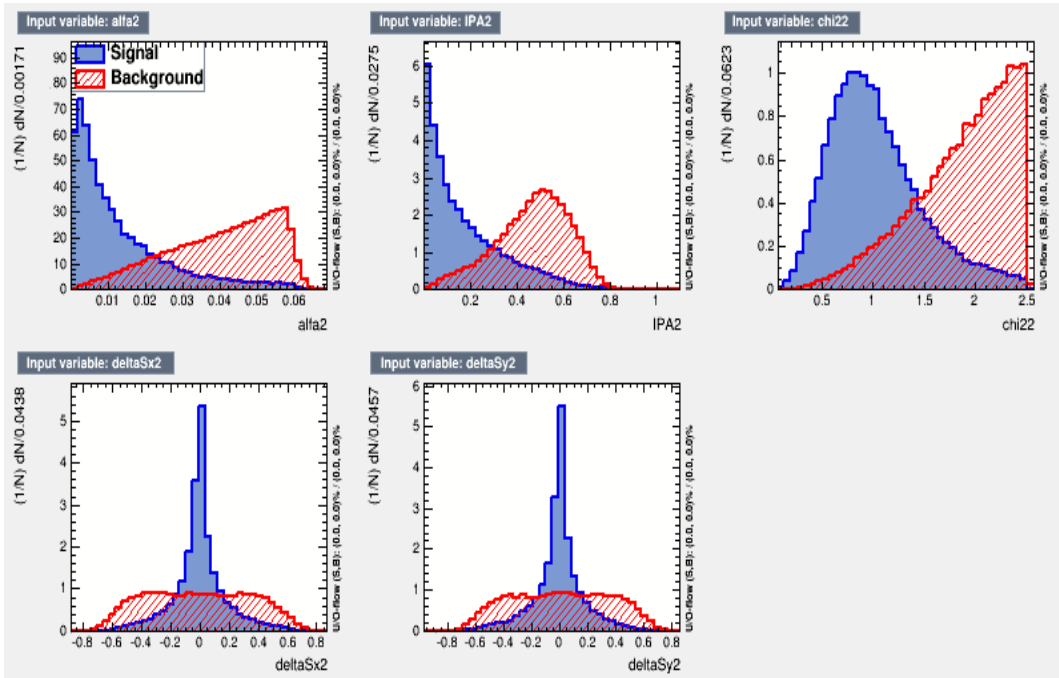


Figure 4.29 – The normalized distribution of the input variables. Signal distribution is shown in blue and the background distributions is in red; Top Left: Alpha distribution, Top Middle: Impact Parameter over  $\Delta Z$  distribution, Top Right:  $\chi^2$  distribution, Bottom Left: Angular difference in X projection, Bottom Middle: Angular difference in Y projection.

The optimal cut value given by BDT algorithm is shown in Figure 4.31. Given the geometry, there is a larger amount of background base-tracks; this effect makes us to apply a stronger cut on the BDT response. Therefore in the second brick, just those signal base-tracks having a BDT response greater than 0.31 are selected. This allows us to accept 19 background base-tracks and about 220 signal base-tracks on average per event.

Figure 4.32 shows a scatter plot of the linear dependency of the MC true energy as the function of the total number of base-tracks.

#### 4.4. Energy Estimation by Using One or Two ECC Bricks

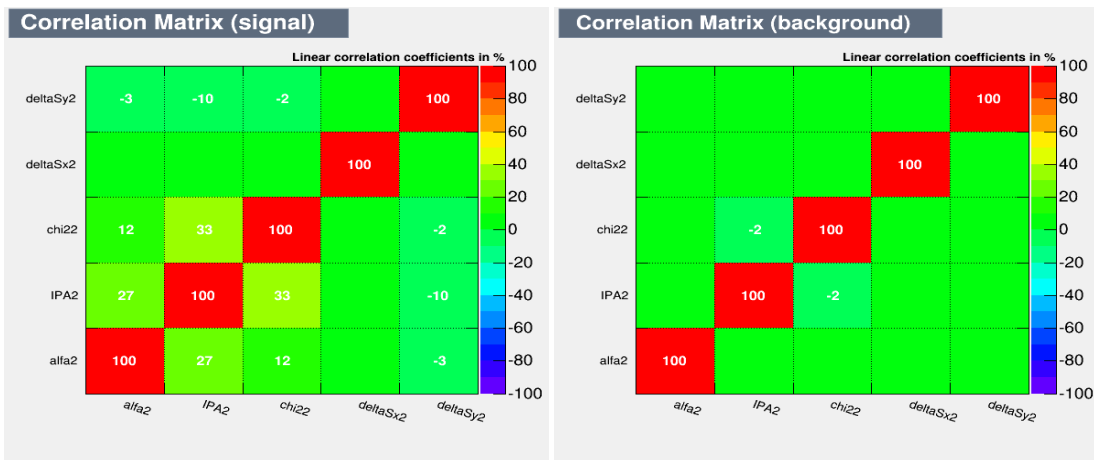


Figure 4.30 – The correlation matrix; Left: Signal, Right: Background.

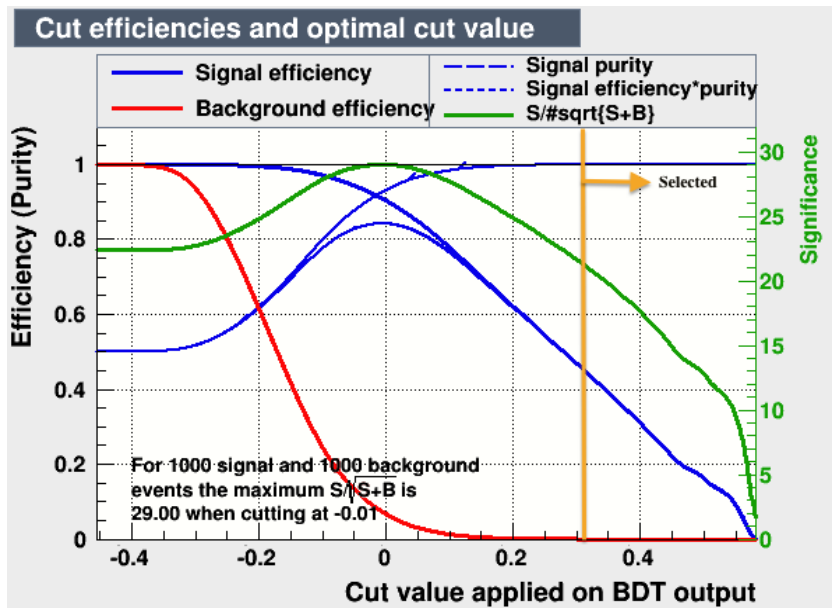


Figure 4.31 – The cut efficiencies and the optimal cut value coming out by BDT algorithm. The signal tracks having a BDT response greater than 0.31 are selected.

The parameterization of the reconstructed energy,  $P_0$  and  $P_1$ , for the Zone2 are given as:

$$P_0 = (0.294 \pm 0.189) \text{ GeV}, \quad (4.22)$$

$$P_1 = (0.048 \pm 0.001) \text{ GeV}. \quad (4.23)$$

Figure 4.33 shows the distribution of the reconstructed energy resolution in the region of Zone2 by using two consecutive bricks, integrated over the entire energy spectrum.

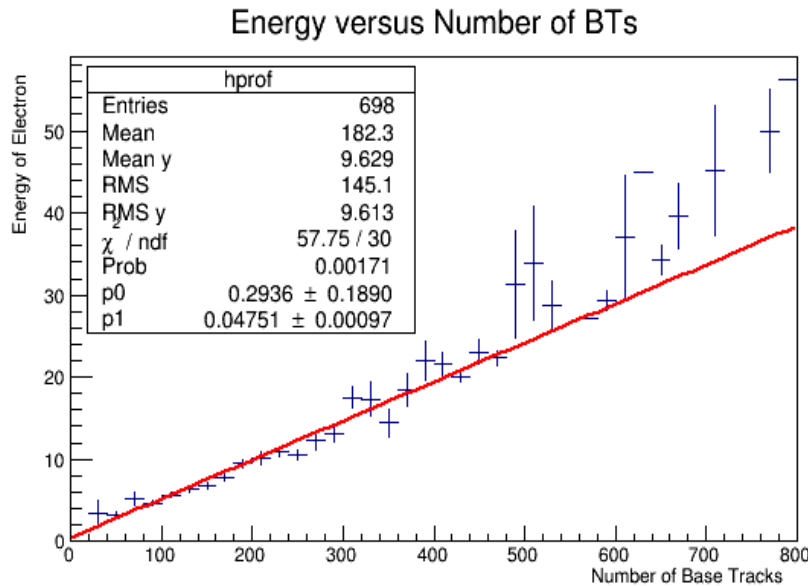


Figure 4.32 – The calibration curve of the energy as a function of the number of base-tracks for the Zone2 region.

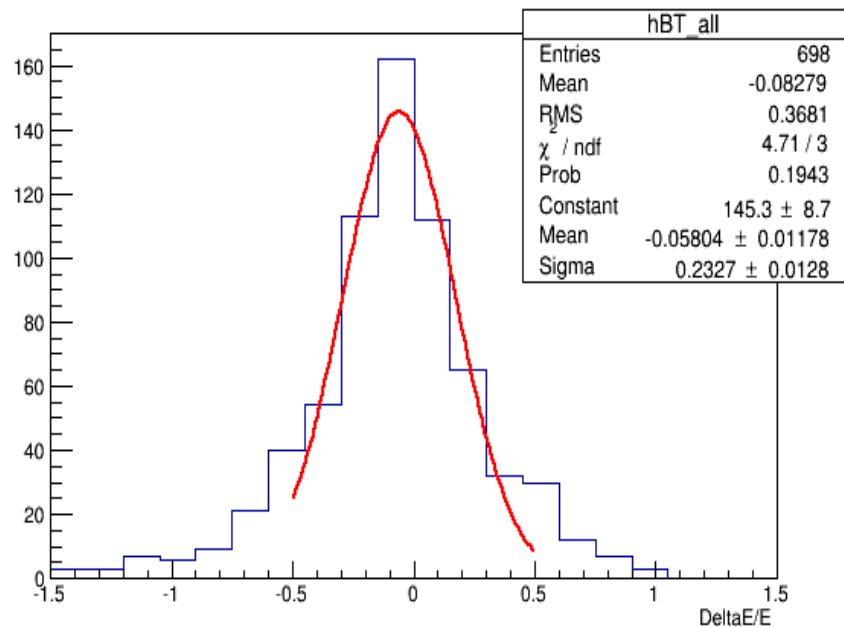


Figure 4.33 – The  $\frac{\Delta E}{E}$  distribution.

The fractional resolution for the events occurring in Zone2 is given by:

$$\sigma_E = 0.23 \pm 0.01. \quad (4.24)$$

The distribution of the resolution as a function of energy is shown in figure 4.34. As expected,  $\sigma_E$  improves with the energy. A fit using the relationship

$$\sigma_E = A_2 + \frac{B_2}{\sqrt{E_{REC}}} \quad (4.25)$$

has been performed, giving:

$$A_2 = 0.202 \pm 0.001, \quad (4.26)$$

$$B_2 = 0.134 \pm 0.007. \quad (4.27)$$

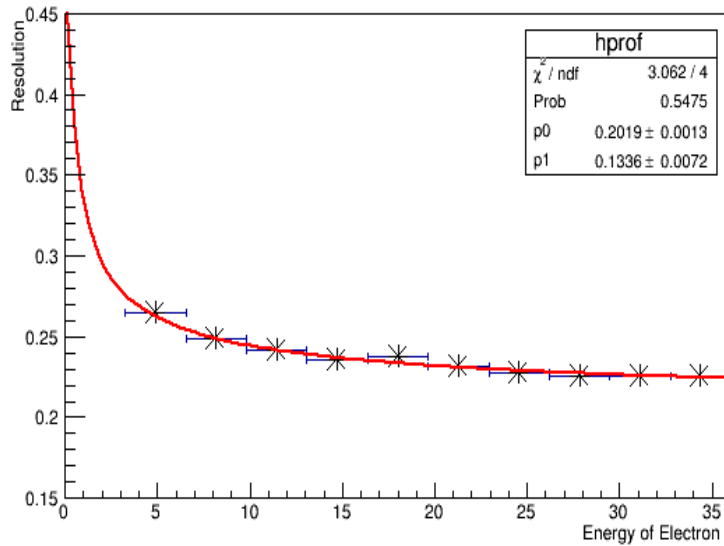


Figure 4.34 – The  $\sigma_E$  as a function of the electron energy.

## 4.5 $\nu_e$ Analysis

By exploiting the electron identification capability for the reconstruction of the  $\tau \rightarrow e$  decay, OPERA is able to perform also  $\nu_\mu \rightarrow \nu_e$  oscillation search. In the CNGS beam the expected  $\nu_e$  contamination is relatively small compared to the dominant  $\nu_\mu$  component ( $\nu_e / \nu_\mu = 0.8\%$ ). Seeking for an excess of  $\nu_e$  charged current events can make the search for  $\nu_\mu \rightarrow \nu_e$  oscillations as well.

## Chapter 4. Energy Estimation of Electromagnetic Showers

---

Therefore, this analysis is also useful for the  $\nu_\mu \rightarrow \nu_e$  oscillation search and the energy will be a key element to discriminate between oscillated events (low energy) and  $\nu_e$  contamination in the beam (high energy).

The performance of the energy estimation algorithm for the  $\nu_e$  events is done on the Monte Carlo samples of 8000 events. The energy of the electron for the  $\nu_e$  events is determined similarly like the  $\tau \rightarrow e$  decay by opening a cone with the axis corresponds to the direction of electron and having a fixed angle of  $\alpha_{cone} = 50$  mrad. The result of this study for the Zone1 and Zone2 are summarized in the following.

### 4.5.1 zone1

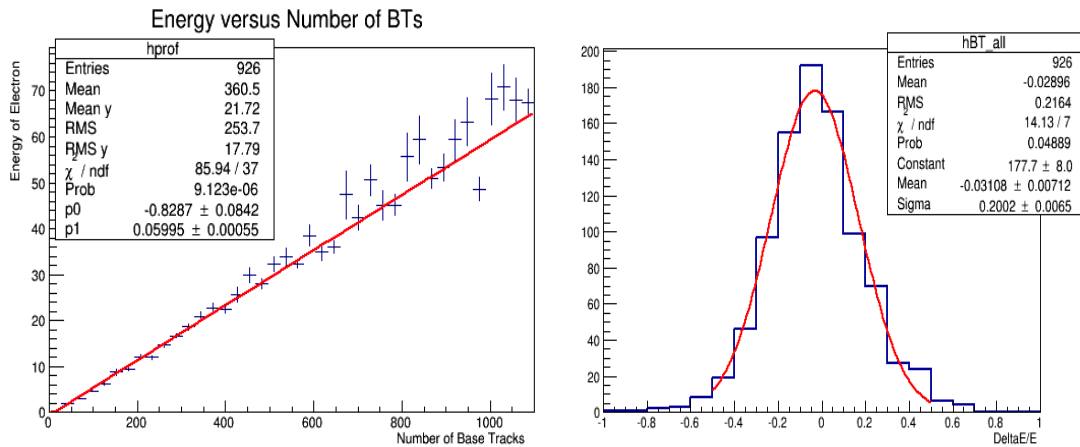


Figure 4.35 – The electron neutrino analysis for the Zone1; Left: The calibration curve of the energy versus the number of base-tracks for the Zone1 region, Right: The  $\frac{\Delta E}{E}$  distribution.

Average number of BTs per event (Signal)	365
Average number of BTs per event (BG)	19

Table 4.2 – The average number of base-tracks in each event

P0	$(-0.829 \pm 0.084)$ GeV
P1	$(0.060 \pm 0.001)$ GeV
$\sigma$	$0.20 \pm 0.01$

Table 4.3 – The P0, P1 and  $\sigma$  given by the fit for  $\nu_e$  events

### 4.5.2 zone2

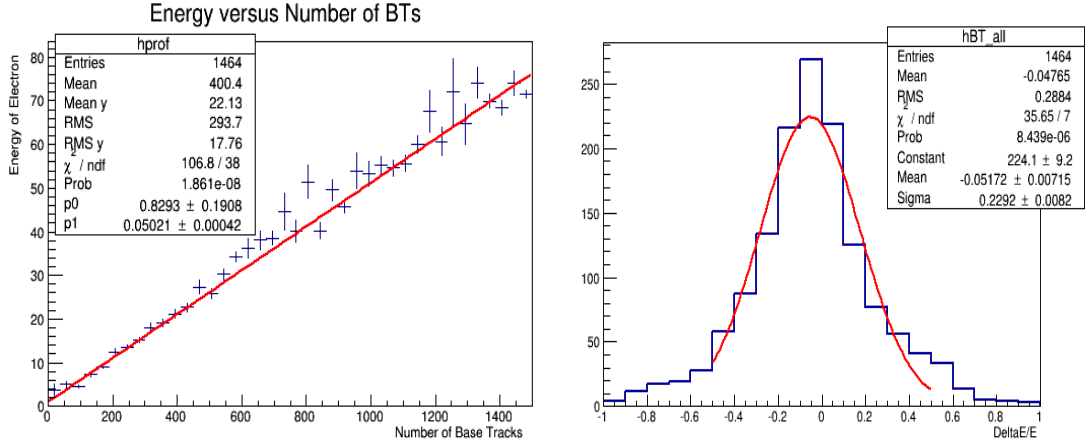


Figure 4.36 – The electron neutrino analysis for the Zone2; Left: The calibration curve of the energy versus the number of base-tracks for the Zone2 region, Right: The  $\frac{\Delta E}{E}$  distribution.

Average number of BTs per event (Signal)	388
Average number of BTs per event (BG)	21

Table 4.4 – The average number of base-tracks in each event

P0	$(-0.829 \pm 0.191)$ GeV
P1	$(0.050 \pm 0.001)$ GeV
$\sigma$	$0.23 \pm 0.01$

Table 4.5 – The P0, P1 and  $\sigma$  given by the fit for  $\nu_e$  events

Figure 4.37 shows the oscillated momentum spectra of electrons produced in  $\tau \rightarrow e$  decays and in  $\nu_e$  interactions. The difference between the two comes from the following: tau neutrinos come from the oscillation of  $\nu_\mu$ 's produced by the decay of  $\pi$ 's thus favoring lower energies; on the contrary, electron neutrinos are produced by  $\kappa$  decays, thus being more energetic.

## Chapter 4. Energy Estimation of Electromagnetic Showers

---

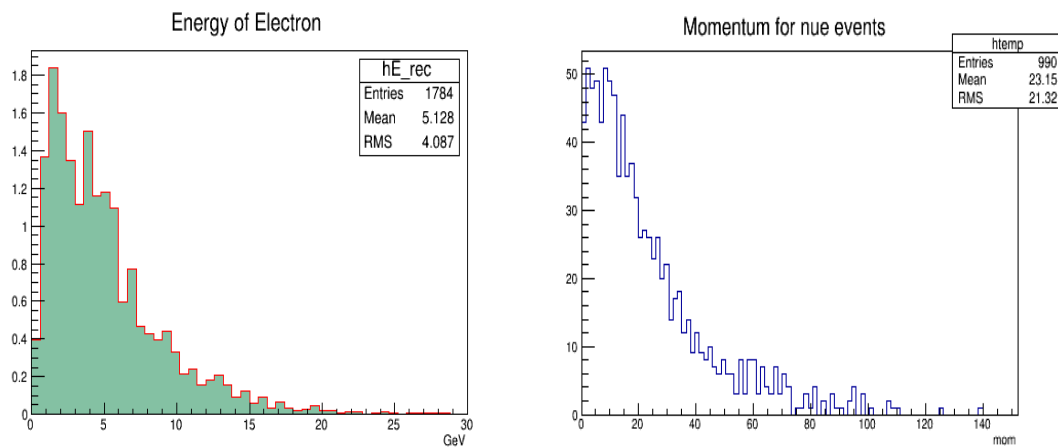


Figure 4.37 – Momentum spectrum of electron; Left: in  $\tau \rightarrow e$  decay channel, Right: for  $\nu_e$  interactions.

# 5 Results

## 5.1 $\nu_e$ Data Analysis

The analysis done in this work is also useful for the  $\nu_\mu \rightarrow \nu_e$  oscillation search in the OPERA experiment. However, in order to discriminate between oscillated events (low energy) and  $\nu_e$  contamination in the beam (high energy), the electron energy will be a key element.

As an application of the algorithm to data, some electromagnetic showers produced by  $\nu_e$  interactions have been studied. In this thesis, two events located in the Napoli scanning laboratory will be presented. The electromagnetic showers of these events were studied in detail.

### 5.1.1 Event 9197043461

This event has been recorded by Electronic Detector on July 2009 and it was located in the Napoli scanning laboratory. The neutrino interaction will be described in the following.

**Event Description:** This event was classified as  $0\mu$  interaction according to the Electronic Detector reconstruction as shown in Figure 5.1.

Figure 5.2 shows a zoom of the target tracker where the neutrino interaction occurred. The green columns in the picture represent the bricks, while the white columns represent the electronic detectors. The spots inside the electronic detectors represent the hits produced by the energy deposited inside the detector. The brick finding algorithm selected the brick number 40009, highlighted in the detector display, as the most probable brick containing the neutrino interaction.

As a first step after the brick selection, the CS doublets of the brick were extracted and analyzed. Figure 5.3 shows the tracks found in the CS doublets. An arrow indicates each track; direction and the magnitude of the arrows are proportional to the track slope and its application point is the impact point of the track on the film.

## Chapter 5. Results

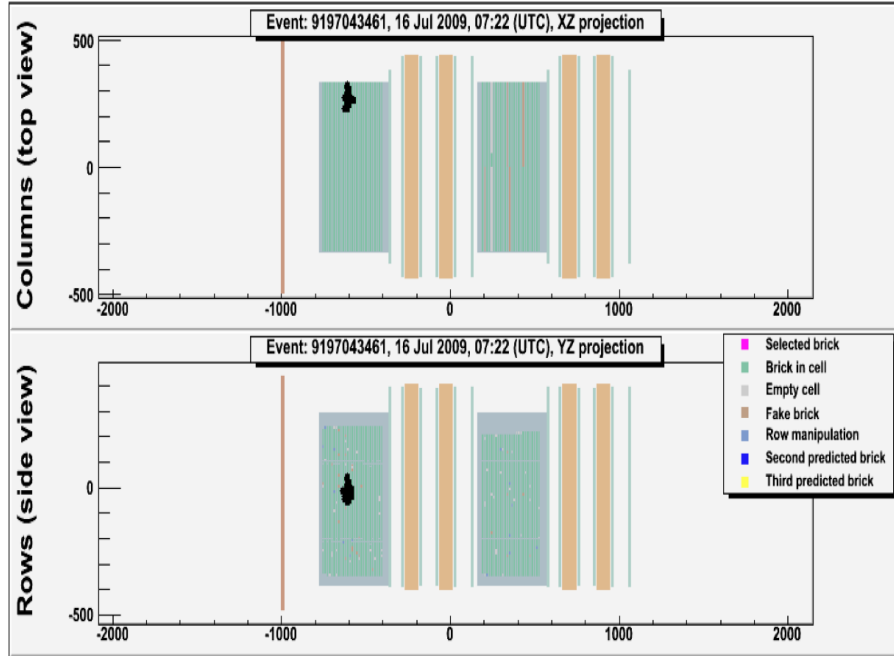


Figure 5.1 – Electronic detector display of the event 9197043461; top: the XZ projection and bottom: the YZ projection.

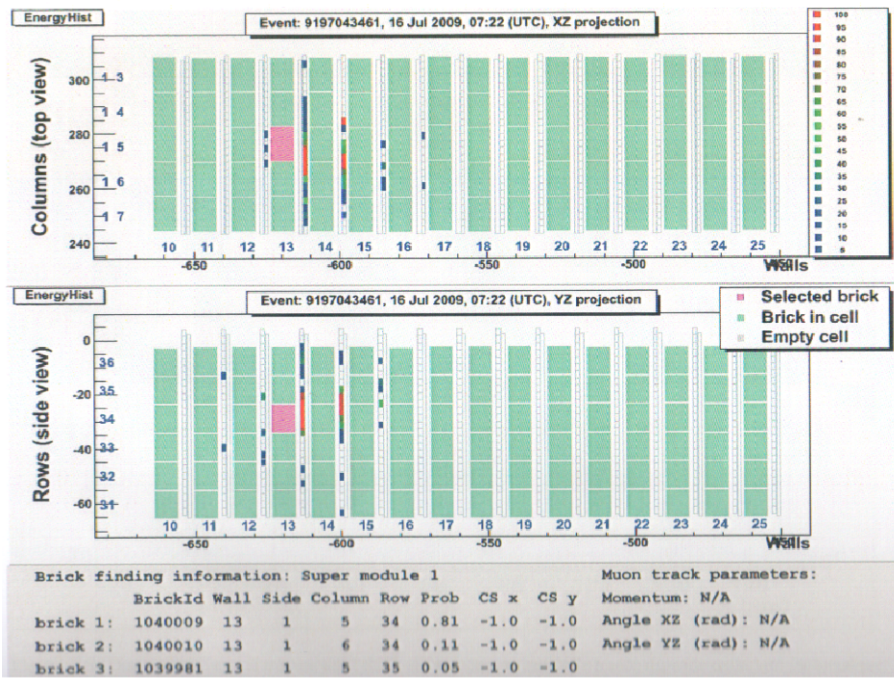


Figure 5.2 – Zoom of the target tracker where the interaction took place (it is highlighted in pink).

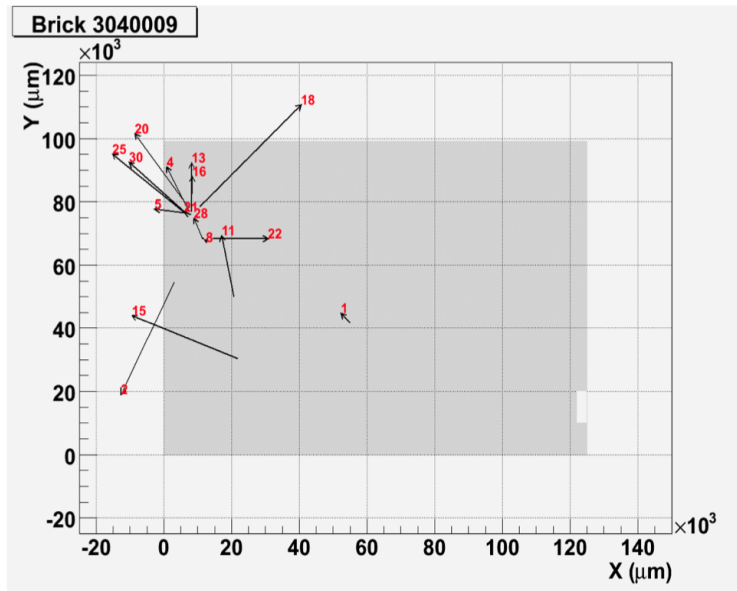


Figure 5.3 – Tracks found in the CS analysis. The lengths of the arrows are proportional to their slopes.

As it is shown in the Figure 5.3, most of the tracks converge in the area around  $X = 1$  cm and  $Y = 7.5$  cm, except a few tracks produced by the passage of cosmic rays. The high number of tracks converging in the CS doublets may indicate the presence of an electromagnetic shower.

The CS-brick connection of this brick is done successfully. In the scan-back procedure, the tracks found in the CS are followed-up. As it's shown in Figure 5.4, some of the tracks converged after crossing a few films. However, only one track was followed up to the most upstream stopping point occurring in plate 27.

The volume-scan around the stopping point, usually done on 15 films, was extended to all the plates downstream of film 27 in order to study the possible shower hint given by the other tracks.

By analyzing the volume-scan data, the electron track was confirmed and the neutrino vertex is located between plates 26 and 27. An additional low momentum particle was confirmed in the primary vertex with the electron. The depth of the vertex in the lead was calculated as  $1094.7 \mu m$ .

The result of the decay search procedure was the selection of two extra tracks; one starting from plate 29 and the other one from plate 30. After applying a visual inspection procedure on these tracks, they were identified as two electron pairs generated by the conversion of photons in the upstream lead. The opening angle between the two photons indicated their common origin from a  $\pi^0$  decay. Therefore, the primary vertex of this event is formed by three particles: an electron, a hadron and a  $\pi^0$ .

## Chapter 5. Results

---

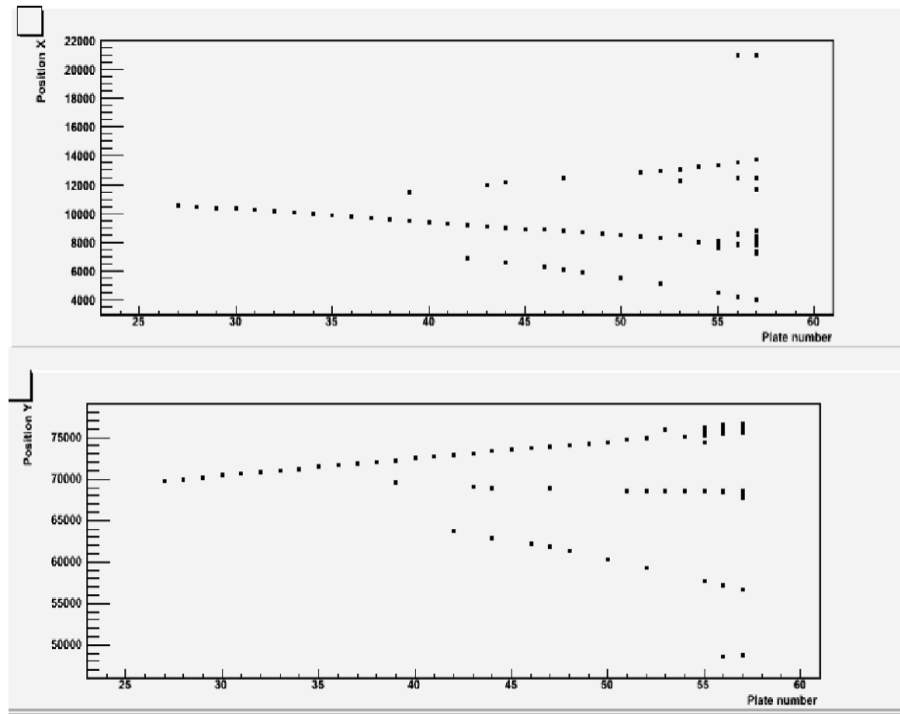


Figure 5.4 – Scan-back tracks in the emulsion films as seen in the projection XZ and YZ. Each plate corresponds to 1.3 mm on the Z axis.

The impact parameters of electron, hadron and the two electron pairs with respect to the common vertex is given in Table 5.1.

Particle	Impact Parameter ( $\mu m$ )
Electron	1.6
Hadron	1.6
First $\gamma$	23.7
Second $\gamma$	31.0

Table 5.1 – Impact parameters of the particles attached to the primary vertex.

The final display of the event reconstruction inside the emulsions is shown in Figure 5.5. As the electron was found at the primary vertex, this event was classified as a  $\nu_e$  interaction.

### Energy Measurement:

In order to reconstruct the electromagnetic shower of this event and to estimate its energy, the algorithm developed in this work was applied. As mentioned before, this event occurred in the very beginning of 2nd zone between plates 26 and 27. However, because at the time of writing this thesis, the information of the downstream brick was not available, the reconstruction and energy estimation of this event was based on the first brick only. Therefore, a volume

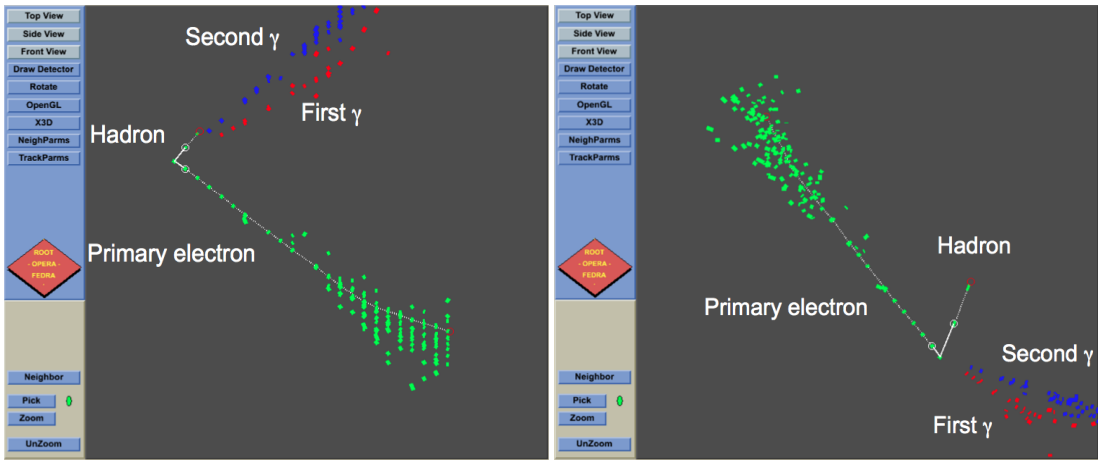


Figure 5.5 – Vertex display of the interaction contained in the brick 40009. Left: Side View; Right: Front View.

from plate 22 up to plate 57 has been made and a cone is defined starting from the primary vertex with the axis in the direction of the electron. Moreover, both the uncorrelated tracks in the emulsions integrated during the transportation from Japan to Gran Sasso and cosmic rays passing through the brick before its development were discarded by applying a dedicated procedure.

In order to do the signal/background separation, all the variables for all base-tracks inside the cone are calculated. By applying the BDT method and selecting the base-tracks with a BDT response greater than 0.2, the algorithm selected 298 base-tracks.

By using the parameters of the reconstructed energy, P0 and P1, for the Zone1 of  $\nu_e$  analysis, the energy is calculated as

$$E = 17.0 \pm 3.5 \text{ GeV.} \quad (5.1)$$

The error on the energy was calculated by propagating those on the number of tracks and on the parameters of the calibration curve. This error is consistent with the expected resolution calculated in the zone1. This result is in agreement with the measurement obtained with the standard algorithm,  $E = 15.4 \text{ GeV}$ .

### 5.1.2 Event 226395185

The event 226395185 was recorded by Electronic Detector on August 2008 and later was located in the Napoli scanning laboratory.

**Event Description:** According to the electronic detector reconstruction, this event also was identified as  $0\mu$  interaction as shown by the Electronic Detector display in Figure 5.6.

## Chapter 5. Results

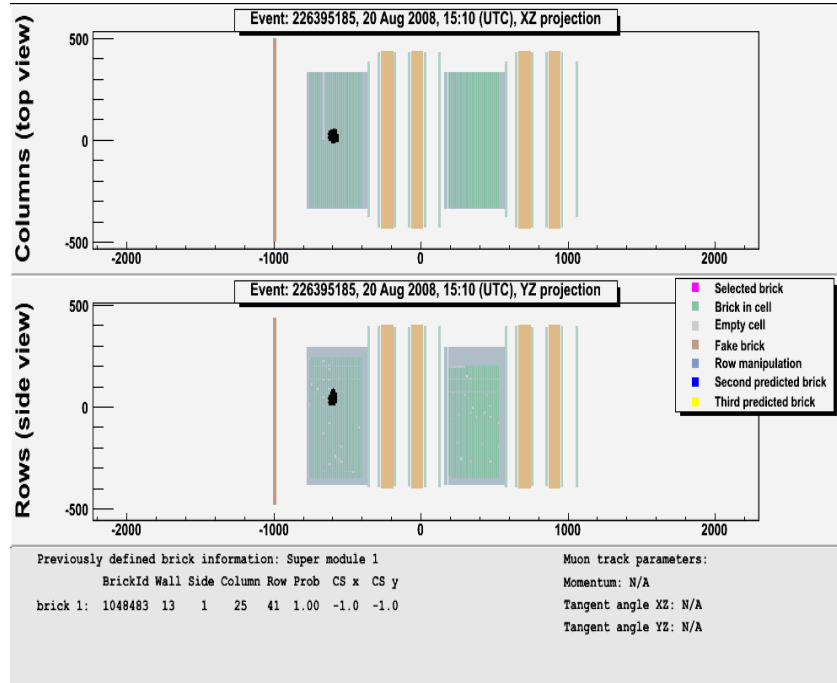


Figure 5.6 – Electronic detector display of the event 226395185; top: the XZ projection and bottom: the YZ projection.

A zoom of the target tracker of the event with the hits produced by the energy deposit inside the detector is shown in Figure 5.7. The brick finding algorithm selected the brick number 48483 as the most probable brick containing the interaction. Figure 5.8 shows the tracks found in the CS doublets of this brick.

The CS-brick connection of this brick was also done successfully and one of the found tracks in CS doublets was found in plate 57. This track was followed-up and it stopped after 5 plates.

After the scan-back procedure and finding the stopping point, the volume-scan procedure was applied. After analyzing the volume-scan data, a small electromagnetic shower was confirmed. The electron found in the shower stopped between plates 52 and 53. One single base-track was found in the plate 53 and 5 base-tracks were found in plate 54 (see Figure 5.9). No other tracks related to the event were found in the volume-scan data. Therefore the event was registered as a single prong event where its single prong is an electron.

In addition, the DS procedure was applied to this event but no extra track was found.

As mentioned before, the interaction was located in very downstream portion of the brick. Therefore, the major part of the shower has occurred in its following brick. In order to reconstruct the electromagnetic shower of this event, the downstream brick was requested by Napoli group to be developed. This brick, number 47839, was developed and sent to Napoli scanning laboratory. In the following the reconstruction of the electromagnetic shower and

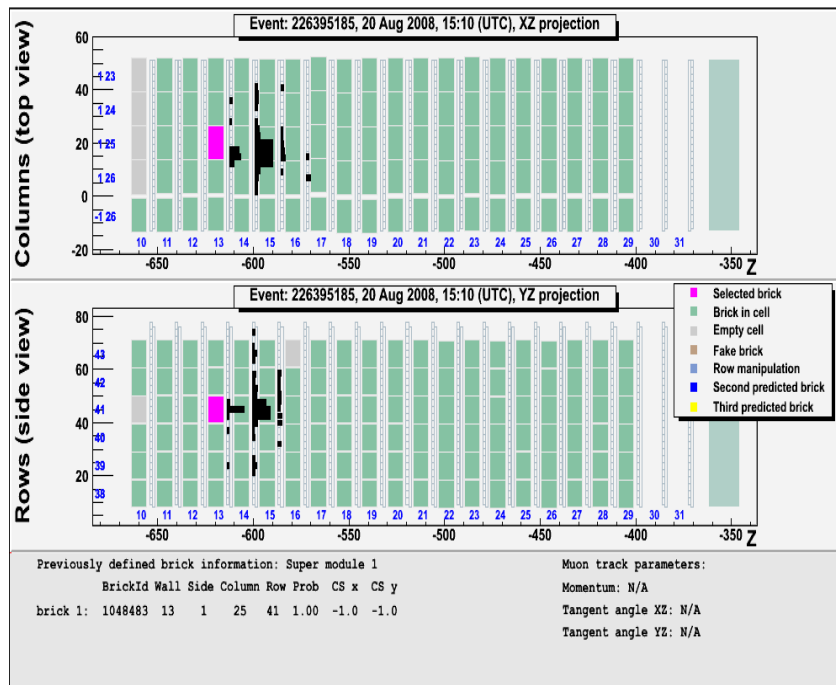


Figure 5.7 – Zoom of the target tracker where the interaction occurred (it is highlighted in pink).

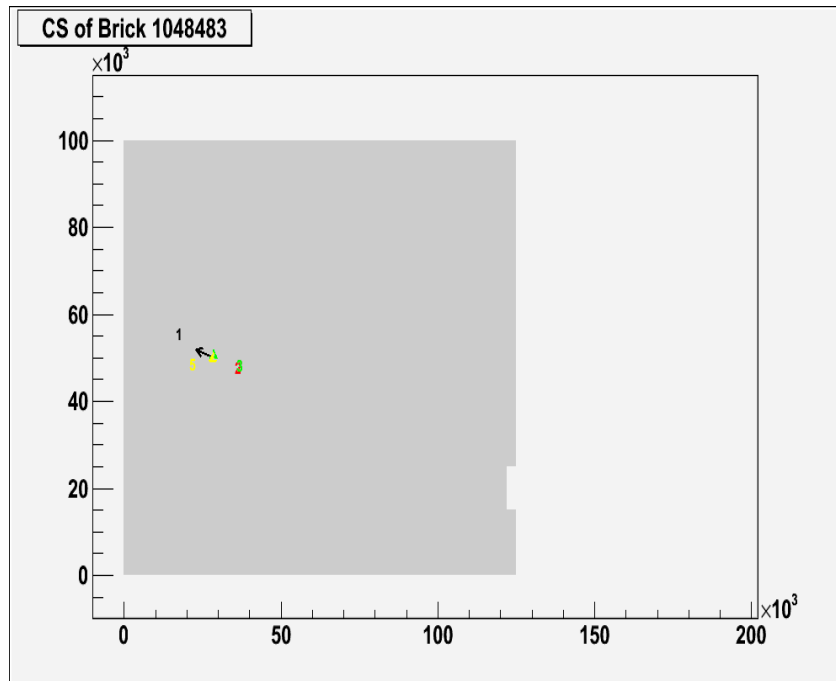


Figure 5.8 – Tracks found in the CS analysis. The lengths of the arrows are proportional to their slopes.

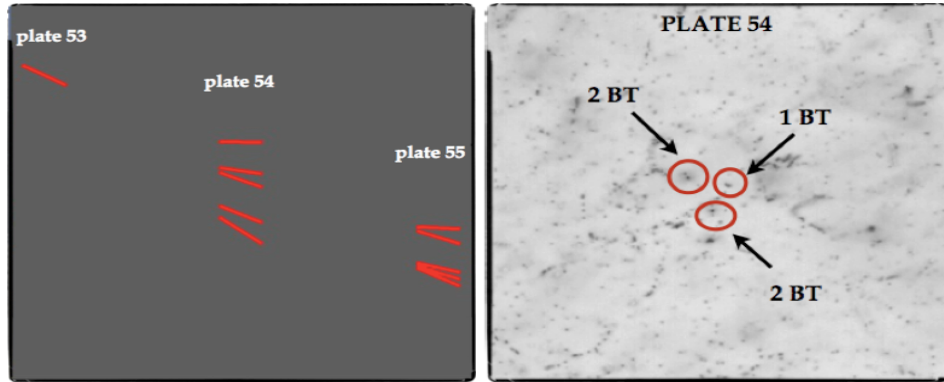


Figure 5.9 – The base-tracks found in plates 53 and 54.

the energy estimation will be described.

#### **Energy Measurement:**

The electromagnetic shower is reconstructed and its energy is estimated using the new algorithm developed for this work. This event is located in the 2nd zone (see Section 4.4.1) between plates 52 and 53. Therefore, the reconstruction and energy estimation of this event is calculated with the selection used for the events in zone2. In the first brick, a volume from plate 48 up to plate 57 is analyzed and the strategy to reconstruct the showers in this zone is applied. In addition, the first 20 plates of its downstream brick are used to find the rest of the electromagnetic shower in the second brick. The alignment between the two bricks was done by finding the primary electron in 2nd brick. The uncorrelated tracks in the emulsions due to the transportation from Japan to Gran Sasso and due to the cosmic rays passing through the brick were discarded for this event.

The signal/background separation process is applied and base-tracks having a BDT response greater than 0.33 in the second brick are selected. The algorithm selected 14 base-tracks located in the first brick and 434 base-tracks in the second brick.

By using the parameters of the reconstructed energy, P0 and P1, for the Zone2 of  $\nu_e$  analysis, the energy is calculated as

$$E = 22.8 \pm 5.2 \text{ GeV.} \quad (5.2)$$

This error is consistent with the expected resolution calculated in the zone2.

Figure 5.10 shows a schematic view of the electromagnetic shower reconstruction within two bricks.

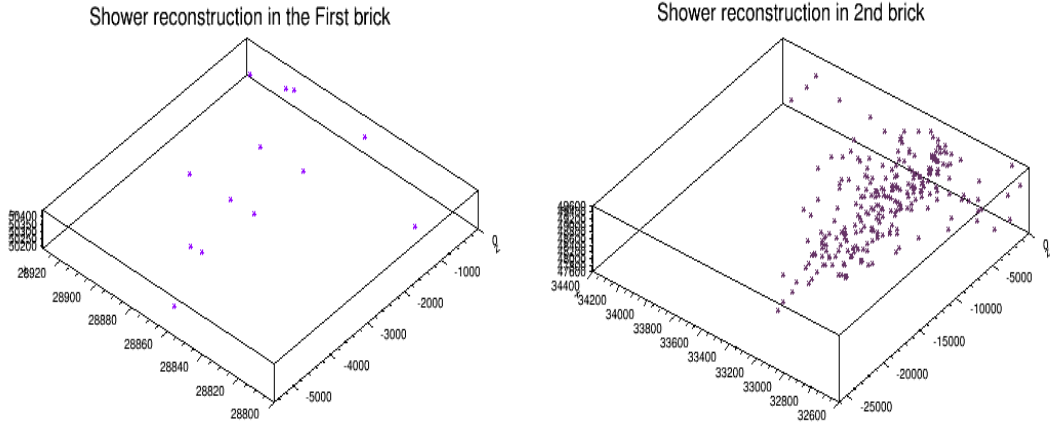


Figure 5.10 – A schematic view of the electromagnetic shower reconstruction within two bricks.

## 5.2 Kinematical Selection

The presence of a  $\nu_\tau$  interaction is initiated by the decay search procedure that defines its decay topology. A high resolution scanning is applied on the primary and decay daughter tracks to measure their energy through the detection of the Multiple Coulomb Scattering for hadrons and through the detection of the shower for electrons.

In order to distinguish the real  $\tau$  events from the backgrounds it is necessary to apply a kinematical selection to the  $\tau$  neutrino interactions. The kinematical cuts are different for each particular  $\tau$  decay channel to suppress the possible background of each decay channel. In the following, the kinematical and topological variables used for the selection of the  $\tau \rightarrow e$  decay channel are explained:

- $z_{dec}$ : the z-coordinate of the decay vertex with respect to the downstream face of the lead plate containing the primary vertex, see Figure 5.11.
- $p_T^{electron}$ : the transverse momentum of the electron with respect to the direction of  $\tau$  lepton.
- $E_{electron}$ : the energy of electron.
- $\theta_{kink}$ : the average 3D angle between the  $\tau$  lepton and its electron (kink angle).

When  $\tau$  lepton decays into the electron, it is required to have a  $z_{dec}$  smaller than  $2600 \mu m$ . It

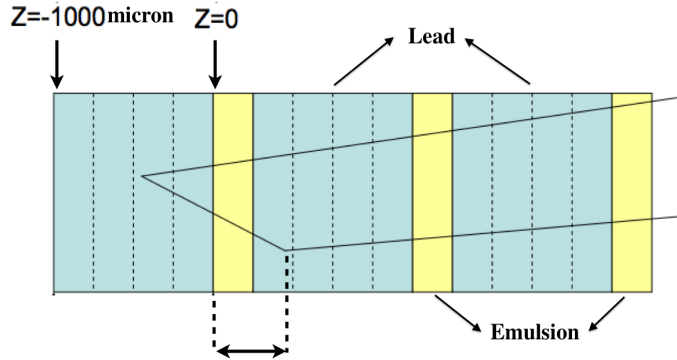


Figure 5.11 – Definition of the  $z_{dec}$  variable. Blue rectangles represent the 1 mm lead plates; yellow rectangles represent the emulsion films.

also has to satisfy the cut  $p_T^{electron} > 0.1 \text{ GeV/c}$  in order to eliminate the contamination from  $\nu_e^{CC}$  interactions.

To reduce the background from low energy electrons (induced by,  $\gamma \rightarrow e^+ e^-$ ) and also to improve the electron identification, the electron ( $\tau$ 's daughter) is required to have an energy higher than 1 GeV. In addition to this, an upper cut on the energy, 15 GeV, reduces the background coming from the prompt electrons produced in  $\nu_e^{CC}$  interactions. A cut on the kink angle,  $\theta_{kink}$  larger than 20 mrad, is also applied. The distribution of the kinematical variables used in this selection is shown in Figure 5.12. The values of the kinematical selection for this particular channel are summarized in Table 5.2.

The kinematical selection efficiencies for the  $\tau \rightarrow e$  decay channel is calculated as 59.7%.

Variable	Selection
$\theta_{kink}$ (mrad)	>20
$E_{electron}$ (GeV)	>1 and <15
$z_{dec}$ ( $\mu\text{m}$ )	<2600
$p_T^{electron}$ (GeV/c)	>0.1

Table 5.2 – Selection criteria for the  $\nu_\tau$  interaction search in the  $\tau \rightarrow e$  decay channel.

### 5.3 Overall Detection Efficiency

The overall detection efficiency,  $\epsilon_{total}$  for each channel is calculated as the product of all reconstruction efficiencies:

$$\epsilon_{total} = \epsilon_{trigger} \times \epsilon_{ED} \times \epsilon_{OpCarac} \times \epsilon_{BF} \times \epsilon_{CS} \times \epsilon_{SB} \times \epsilon_{LOC} \times \epsilon_{DS} \times \epsilon_{KIN}. \quad (5.3)$$

By multiplying all factors, the efficiency for the  $\tau \rightarrow e$  decay channel is evaluated and the

### 5.3. Overall Detection Efficiency

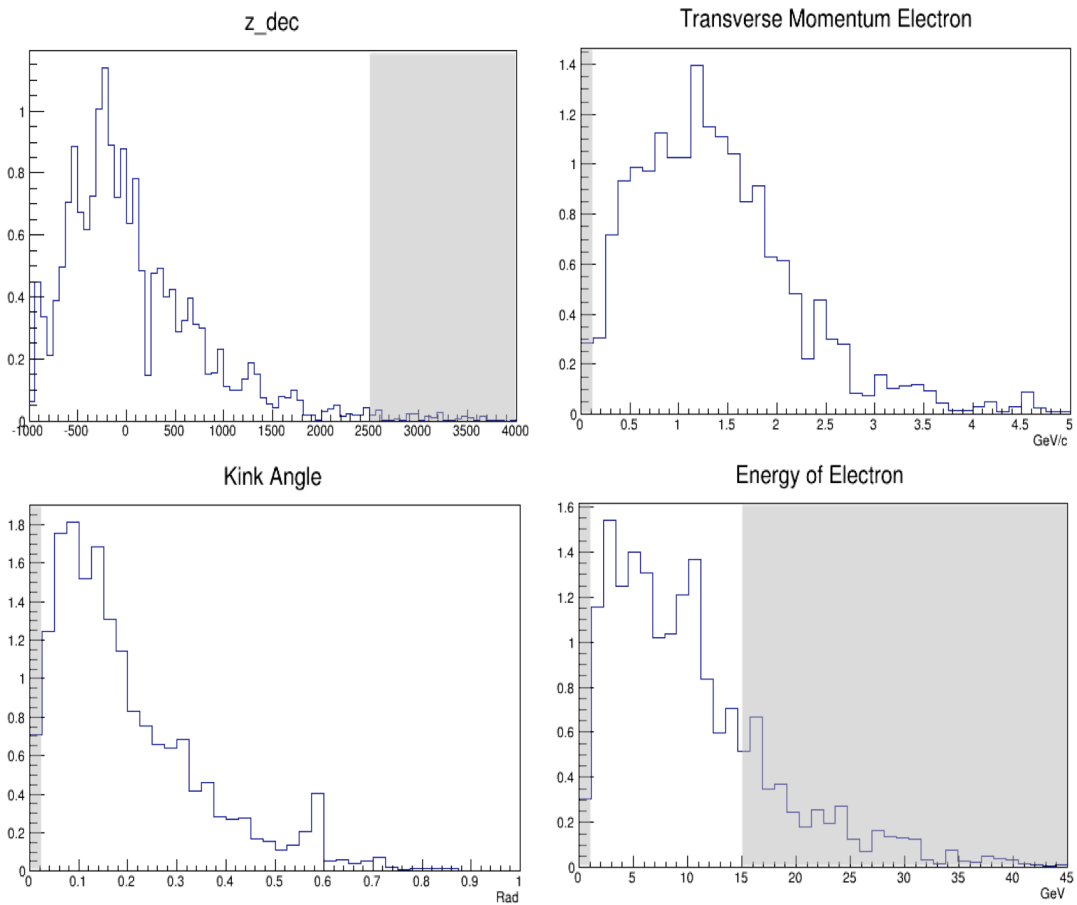


Figure 5.12 – Distribution of kinematical variables for the  $\tau \rightarrow e$  decay channel; Top Left:  $z_{dec}$ , Top Right:  $p_T^{electron}$ , Bottom Left: kink angle  $\theta_{kink}$ , Bottom Right:  $E_{electron}$ .

results are reported in Table 5.3.

	Long Decay	Short Decay
2008 and 2009 data selection	$0.136 \pm 0.005$	$0.103 \pm 0.005$

Table 5.3 – Summary of the  $\tau$  detection efficiency for 2008-2009 data selection. The uncertainties are due to statistical errors.

The algorithm developed in this work has improved the resolution in the energy estimation of the electron. This corresponds to higher efficiency in kinematical selection in the  $\tau \rightarrow e$  decay channel. As described in the previous chapters, the algorithm requires the showers to be within a fiducial volume. This produces the drawback to reduce the overall detection efficiency. These two effects, the first increasing the efficiency and the second one decreasing the efficiency, compensate each other thus making the overall detection efficiency in  $\tau \rightarrow e$  decay channel comparable with the one obtained with the previous estimations (summarized

## Chapter 5. Results

---

in Table 5.4). The application of the new algorithm, although with reduced efficiency, to events occurring near the edge will improve the overall detection efficiency in this channel.

	Long Decay	Short Decay
2008 and 2009 data selection	$13.5 \pm 0.5$	$9.8 \pm 0.5$

Table 5.4 – Summary of the  $\tau$  detection efficiency for 2008-2009 data selection done in the previous analysis [125].

Moreover, the energy spectrum of the electrons in  $\tau \rightarrow e$  decay channel is shown in Figure 5.13 left. Introducing the oscillation probability of neutrinos, the energy distribution of the electrons is shifted to left side favoring low energies, as shown in Figure 5.13 right.

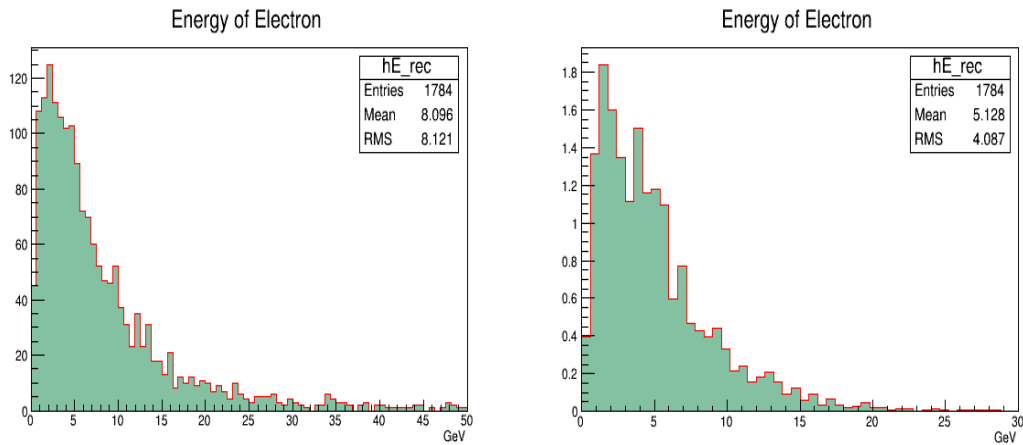


Figure 5.13 – Energy distribution of the electrons generated by the  $\tau$  decay; Left: before the application of the oscillation probability; Right: after the application of the oscillation probability.

# Conclusion

The OPERA experiment is a long baseline neutrino oscillation experiment designed to perform a conclusive proof of the  $\nu_\mu \rightarrow \nu_\tau$  oscillations hypothesis. The peculiarity of this experiment is a direct observation of  $\tau$  leptons in  $\nu_\tau$  charged-current interactions and therefore the observation of neutrino oscillation in appearance mode. OPERA exploits its electron identification capability to reconstruct the  $\tau \rightarrow e$  decay. As a byproduct, it is also able to perform a  $\nu_\mu \rightarrow \nu_e$  oscillation search, although this oscillation mode is subdominant. The OPERA detector is located in Gran Sasso underground laboratory, 730 km away from CERN where CNGS neutrino beam is produced.

A sample of 19505 contained neutrino interactions corresponding to  $17.97 \times 10^{19}$  protons on target have been registered by the OPERA detector after 5 years data taking, from 2008 to 2012. OPERA is the only experiment that has observed  $\nu_\tau$  appearance in a pure  $\nu_\mu$  neutrino beam. So far, 4  $\nu_\tau$  candidates have been observed in the OPERA detector with a background of 0.23 event. Given the low expected background,  $\nu_\mu \rightarrow \nu_\tau$  oscillations are established with a significance of  $4.2\sigma$ .

In this thesis, the analysis chain of neutrino interactions in the OPERA target has been fully simulated and the efficiencies are estimated for all the MC samples with an electron in the final state: prompt  $\nu_e$ , oscillated  $\nu_e$ ,  $\nu_\mu \rightarrow \nu_\tau$  in  $\tau \rightarrow e$  mode. The comparison between data and Monte Carlo performed with the  $\nu_\mu^{NC}$  samples shows a good agreement, thus validating the simulation used to describe the event analysis.

A good electromagnetic shower reconstruction is mandatory for the  $\tau$  detection in the  $\tau \rightarrow e$  decay channel given the branching ratio of about 18%.

The algorithm currently used by the Collaboration estimates the electron energy through a calorimetric measurement of the shower achieving a resolution not better than 30%.

The work done in this thesis is focused on the improvement of the electron energy resolution for both  $\tau \rightarrow e$  decays and  $\nu_e^{CC}$  interactions. A dedicated shower reconstruction algorithm is developed to evaluate the energy of electrons through the identification of its shower, using the OPERA brick as a calorimeter. The algorithm developed in this work selects all the tracks within a cone with the vertex located at the electron production point. It uses larger values of the geometrical parameters for the cone definition and the Boost Decision Tree method, by

## Conclusion

---

the TMVA toolkit, to get a better Signal/Background separation.

Normal reconstruction of a shower event depends upon the containment of the shower. However, when a shower is initiated in the downstream portion of the brick, the shower will partially develop in the downstream brick, making normal reconstruction methods unusable.

The approach developed for this thesis is using for the first time the information of the downstream brick to reconstruct and estimate the energy of electromagnetic showers.

In this work, the signal is studied by simulating the electromagnetic showers with the Monte Carlo simulation. Background tracks are evaluated by scanning an empty volume without any neutrino interaction inside. The algorithm selects all the tracks inside a cone, with the axis along the electron direction. Several variables are separately calculated for signal and background base-tracks inside the cone and the Boost Decision Tree method is used for the signal/background separation.

The energy of showering electrons is determined by its correlation with the number of reconstructed base-tracks in the cone. This number does not depend only on the electron energy but it's also affected by the position in the brick of the decay point of  $\tau$  lepton. Therefore, the ECC brick is divided in different zones. Showers initiated in the upstream 21 plates are fully reconstructed within that brick. However, for showers initiated in the downstream emulsion foils from 22nd to 57th, the full shower reconstruction is made within two bricks. To ensure the lateral containment of the shower, the events occurred within one centimeter from the lateral edge of the brick are discarded.

As the result, the fractional resolution,  $\sigma_E$ , of the events occurring in Zone1 is calculated based on MC simulation as  $\sigma_E = 0.21 \pm 0.01$ , while the fractional resolution for the events occurring in Zone2 is given as  $\sigma_E = 0.23 \pm 0.01$  using the information of the downstream brick.

As an application of the algorithm to data, two showers associated to two different electron neutrino interactions reconstructed in the Napoli laboratory, are studied. The electron tracks in both interactions were reconstructed and their energies are estimated. The electromagnetic shower of event 9197043461 is reconstructed within one brick and the electron energy is estimated as  $E = 17 \pm 3.5$  GeV. However, as the interaction of event 226395185 was located in very downstream portion of the brick, the electromagnetic shower reconstruction and its energy estimation is done within two bricks. For this event the electron energy is estimated as  $E = 22.8 \pm 5.2$  GeV.

A kinematical selection is applied to the  $\tau$  neutrino interactions in order to distinguish the real  $\tau$  events from the backgrounds. The kinematical and topological variables used for the selection of the  $\tau \rightarrow e$  decay channel are studied with MC simulations and by using the electromagnetic shower reconstruction and electron energy estimation evaluated through the new algorithm developed in this work.

This algorithm gives an improved resolution of the electron energy estimation, achieving

a higher kinematical selection efficiency in the  $\tau \rightarrow e$  decay channel. On the other hand, the containment requirement (1 cm from the edge) for the application of the algorithm compensates the gain in the efficiency, thus producing a detection efficiency in the  $\tau \rightarrow e$  channel compared to the previous estimate. The application of this new algorithm, although with reduced performances, to the events close to the brick edge will improve the overall detection efficiency.



# Bibliography

- [1] Robert G. Arns, *Detecting the Neutrino*, Phys.pers. 3 314-334, 2001.
- [2] COBRA web page, <http://www.cobra-experiment.org/>. Retrieved on January, 2014.
- [3] M. Riordan, *Pauli's Ghost: The Conception and Discovery of Neutrinos*, in Current Aspects of Neutrino Physics ed. by D.O. Caldwell (Springer-Verlag Berlin Heidelberg New York), 2001.
- [4] W. Pauli, *Aufsatze und Vortrage uber Physik und Erkenntnistheorie*, ed. W. Westphal, Braunschweig (1961).
- [5] W. Pauli, Letter to *radioactive ladies and gentlemen at Tubingen conference*, 4th December 1930.
- [6] E. Fermi, *Tentativo di una teoria dei raggi  $\beta$* , *Nuovo Cimento* 11 (1934), 1-19.
- [7] C. L. Cowan, F. Reines, F. B. Harrison, H. W. Kruse and A. D. McGuire, *Detection of the Free Neutrino: a Confirmation*, *Science* 124 (1956), 103-104.
- [8] F. Reines, *The Neutrino: From Poltergeist to Particle*, University of California, 1995.
- [9] R. Davis Jr., *Solar neutrinos. II: Experimental*, *Phys.Rev.Lett.* 12, 303-305, 1964.
- [10] G. Danby, J-M. Gaillard, K. Goulian, L. M. Lederman, N. Mistry, M. Schwartz and Z. Steinbergert, *Observation of high-energy neutrino interactions and the existence of two kinds of neutrinos*, *Phys. Rev. Lett.* 9 (1962), 36-44.
- [11] K. Assamagan *et al.*, *Phys. Rev. D* 53 (1996) 6065.
- [12] BROOKHAVEN web page, <http://www.bnl.gov/science/neutrinos.php>. Retrieved on January, 2014.
- [13] Ezzat G. Bakhoum, *Are There "Neutrino Flavors"? : More on the Equation  $H = mv^2$* , *physics.gen-ph* 0302095v2, 2003.
- [14] M. L. Perl *et al.*, *Evidence for Anomalous Lepton Production in  $e^+ e^-$  Annihilation*, *Phys. Rev. Lett.* 35 (1975), 1489-1492.

## Bibliography

---

- [15] K. Kodama *et al.*, *Observation of tau neutrino interactions*, Phys. Lett. B504 (2001), 218-224.
- [16] The ALEPH Collaboration, The DELPHI Collaboration, The L3 Collaboration, The OPAL Collaboration, The SLD Collaboration, The LEP Electroweak Working Group, The SLD Electroweak and Heavy Flavour Groups, *Precision electroweak measurements on the Z resonance*, Phys. Rept. 427 (2006), 257-454.
- [17] W. N. Cottingham and D. A. Greenwood, *The Nature of Massive Neutrinos, An Introduction to the Standard Model of Particle Physics*, 2007.
- [18] J. Bonn *et al.*, Prog.Part.Nucl.Phys. 48, 133, 2002; V. M. Lobashev *et al.*, Nucl.Phys.Proc.Suppl. 91, 280, 2001.
- [19] K. Assamagan *et al.*, Preprint No. PSI-PR-94-19, 1994.
- [20] Fabio Cerutti, *Determination of the upper limit on  $m_{\tau}$  from LEP*, hep-ex/9903062v2, 1999.
- [21] Z. Maki, M. Nakagawa, and S. Sakata. *Remarks on the Unified Model of Elementary Particles*. Progress of Theoretical Physics, 28:870-880, 1962.
- [22] C. Giunti, C. W. Kim, *Fundamentals of Neutrino Physics and Astrophysics*, Oxford University Press, Oxford, 2007.
- [23] Ziro Maki, Masami Nakagawa and Shoichi Sakata, *Remarks on the Unified Model of Elementary Particles*, Prog. Theor. Phys. (1962) 28 (5): 870-880.
- [24] S. M. Bilenky and B. Pontecorvo, Sov. J. Nucl. Phys., 24, 316–319, 1976; S. M. Bilenky and B. Pontecorvo, Nuovo Cim. Lett., 17, 569, 1976.
- [25] Paweł Przewłocki, *A study of neutrino interactions constituting the background to electron neutrino appearance in T2K experiment*, Ph.D. thesis, Andrzej Sołtan Institute for Nuclear Studies, 2010.
- [26] M. Kobayashi and T. Maskawa, *CP-Violation in the Renormalizable Theory of Weak Interaction*, Prog. Theor. Phys. 49 (1973), 652-657.
- [27] Zhi-zhong Xing, *Neutrino Physics*, Phys. Rev. D17 (1978), The 1st Asia-Europe-Pacific School of HEP, 10/2012, Fukuoda.
- [28] L. Wolfenstein, *Neutrino oscillations in matter*, Phys. Rev. D17 (1978), 2369-2374.
- [29] C. Giunti and A. Studenikin, *Neutrino electromagnetic properties*, Phys.Atom.Nucl. 72 (2009) 2089-2125.
- [30] S. P . Mikheyev and A. Y. Smirnov, *Resonance Amplification of ν Oscillations in Matter and Solar Neutrino Spectroscopy*, Nuovo Cim. C9 (1986), 17-26.

- [31] T2K web page, <http://t2k-experiment.org/neutrinos/sources-and-experiments/>, Retrieved on January, 2014.
- [32] J.N. Abdurashitov *et al.*, *Measurement of the solar neutrino capture rate with Gallium metal*, Part III, Phys. Rev. C80 (2009) 015807.
- [33] M. Altmann *et al.*, *Complete results for five years of GNO solar neutrino observations*, Phys. Lett. B616 (2005) 174.
- [34] R. Davis, Prog. Part. Nucl. Phys. 32 (1994) 13.
- [35] Gallex Collaboration, W. Hampel *et al.*, Phys. Lett. B447 (1999) 127. GNO Collaboration, M. Altmann *et al.*, Phys. Lett. B490 (2000) 16. SAGE Collaboration, J. N. Abdurashitov *et al.*, Phys. Rev. Lett. 83 (1999) 4686.
- [36] The GALLEX Collaboration, P. Anselmann *et al.*, Phys. Lett. B285 376, 1992.
- [37] J.N. Abdurashitov *et al.*, *Measurement of the Solar Neutrino Capture Rate by the Russian-American Gallium Solar Neutrino Experiment During One Half of the 22-Year Cycle of Solar Activity*, JETP 95 (2002) 181.
- [38] Q. R. Ahmad *et al.*, *Measurement of the rate of  $\nu + D \rightarrow p + p + e^-$  interactions produced by  ${}^8B$  Solar Neutrinos at the Sudbury Neutrino Observatory*, Phys. Rev. Lett. 87 (2001) 071301.
- [39] J. N. Bahcall, SLAC Beam Line 31(1) (2001) 2.
- [40] S. Basu *et al.*, Mon. Not. R. Astron. Soc. 292 (1997) 1402.
- [41] Ahmad Q R *et al.*, (SNO) 2001 Phys. Rev. Lett. 87 071301 (Preprint nucl-ex/0106015).
- [42] Ahmad Q R *et al.*, (SNO) 2002 Phys. Rev. Lett. 89 011301 (Preprint nucl-ex/0204008).
- [43] The SNO Collaboration, J. Boger *et al.*, Nucl.Inst.Meth. A 449 172-207, 2000.
- [44] Kamiokande Collaboration, Y. Fukuda *et al.*, Phys. Rev. Lett. 77 (1996) 1683.
- [45] Super-Kamiokande Collaboration, S. Fukuda *et al.*, Phys. Rev. Lett. 86 (2001) 5651.
- [46] G.L. Fogli, E. Lisi, A. Marrone, A. Palazzo, A.M. Rotunno, *NEUTRINO MASS AND MIXING PARAMETERS: A SHORT REVIEW*, hep-ph/0506307v1, 2005.
- [47] A. Strumia, F.Vissani, *Neutrino masses and mixings and...*, arXiv:hep-ph/0606054v3.
- [48] Becker-Szendy R *et al.*, 1992 Phys. Rev. D46 3720–3724.
- [49] Y. Fukuda *et al.*, (Kamiokande) 1994 Phys. Lett. B335 237–245.
- [50] CV. Achar *et al.*, Phys. Lett. 18:196 (1965).
- [51] F. Reines *et al.*, Phys. Rev. Lett. 15:429 (1965).

## Bibliography

---

- [52] Hirata K.S., Kajita T., Koshiba M., Nakahata M., Ohara S., Oyama Y., *et al.*, *Experimental study of the atmospheric neutrino flux* Phys. Lett. B 205 (1988), 416–420.
- [53] Nakahata M., Arisaka K., Kajita T., Koshiba M., Oyama Y., Suzuki A., *et al.*, *Atmospheric neutrino background and pion nuclear effect for KAMIOKA nucleon decay experiment*, J. Phys. Soc. Jpn. 55 (1986), 3786–3805.
- [54] Haines T.J., Bionta R.M., Blewitt G., Bratton C.B., Casper D., Claus R., *et al.*, *Calculation of atmospheric neutrino-induced backgrounds in a nucleon-decay search*, Phys. Rev. Lett. 57 (1986), 1986–1989.
- [55] Super-Kamiokande Collaboration, Y. Fukuda *et al.*, *Evidence for Oscillation of Atmospheric Neutrinos*, Phys. Rev. Lett. 81 (1998) 1562.
- [56] Super-Kamiokande Collaboration, Y. Fukuda *et al.*, Phys. Lett. B 436, 33 (1999).
- [57] Super-Kamiokande Collaboration, Y. Ashie *et al.*, Phys.Rev.Lett.93:101801,2004.
- [58] L. S. Esposito, *Study of electron identification in the Emulsion Cloud Chambers of the OPERA experiment*, (Doctoral dissertation), Universita degli Studi di Bologna, 2005.
- [59] CHOOZ Collaboration, M. Apollonio *et al.*, Phys. Lett. B420 (1998) 397; M. Apollonio *et al.*, Eur. Phys. J. C27 (2003) 331.
- [60] Ardellier, F. *et al.*, *Letter of intent for Double-CHOOZ: A Search for the mixing angle theta(13)*, hep-ex/0405032 DAPNIA-04-84.
- [61] RENO Collaboration (Ahn, J.K. *et al.*): *An Experiment for Neutrino Oscillation Parameter theta\_{13} Using Reactor Neutrinos at Yonggwang*, arXiv:1003.1391 [hep-ex].
- [62] Dwyer, D.A. *et al.*, *Search for Sterile Neutrinos with a Radioactive Source at Daya Bay*, Phys.Rev. D87 (2013) 9, 093002 arXiv:1109.6036 [hep-ex].
- [63] T2K Collaboration, K. Abe *et al.*, *Indication of Electron Neutrino Appearance from an Accelerator-produced Off-axis Muon Neutrino Beam*, Phys.Rev.Lett. 107 (2011) 041801.
- [64] NOvA Collaboration, D. Ayres *et al.*, *NOvA: Proposal to build a 30 kiloton off-axis detector to study nu(mu) to nu(e) oscillations in the NuMI beamline*, hep-ex/0503053.
- [65] MINOS Collaboration, P. Adamson *et al.*, *Improved search for muon-neutrino to electron-neutrino oscillations in MINOS*, Phys.Rev.Lett. 107 (2011) 181802.
- [66] Y. Abe *et al.*, *Indication for the disappearance of reactor electron antineutrinos in the Double Chooz experiment*, Phys. Rev. Lett. 108 (2012) 131801.
- [67] DAYA-BAY Collaboration, D. Dwyer, *Improved measurement of electron–antineutrino disappearance at daya bay, 2012*. Talk given at the Neutrino 2012 Conference, June 3-9, 2012, Kyoto, Japan, <http://neu2012.kek.jp/>.

- [68] F.P. An *et al.*, *Observation of electron-antineutrino disappearance at Daya Bay*, Phys. Rev. Lett. 108 (2012) 171803.
- [69] RENO Collaboration, S. Kim, *Observation of reactor antineutrino disappearance at reno, 2012*. Talk given at the Neutrino 2012 Conference, June 3-9, 2012, Kyoto, Japan, <http://neu2012.kek.jp/>.
- [70] J.K. Ahn *et al.*, *Observation of Reactor Electron Antineutrino Disappearance in the RENO Experiment*, Phys. Rev. Lett. 108 (2012) 191802.
- [71] G.L. Fogli *et al.*, *Global analysis of neutrino masses, mixings and phases: entering the era of leptonic CP violation searches*, Phys. Rev. D 86 (2012) 013012.
- [72] JGU web page, <http://www.etap.physik.uni-mainz.de/685-ENG-HTML.php>. Retrieved on January, 2014.
- [73] S. M. Bilenky, *A lecture on neutrinos*, arXiv:hep-ph/0402153v1, 2004.
- [74] LBL web page, <http://hitoshi.berkeley.edu/neutrino/>. Retrieved on January, 2014.
- [75] The OPERA Collaboration, M. Guler *et al.*, *An appearance experiment to search for  $\nu_\mu \rightarrow \nu_\tau$  oscillations in the CNGS beam*, CERN/SPSC 028, 2000.
- [76] R. Acquafredda *et al.*, *First event from the CNGS neutrino beam detected in the OPERA experiment*, 8:303 23, 2006.
- [77] CERN, *General description of the CERN project for a neutrino beam to Gran Sasso (CNGS)*. CERN AC Note (2000-03), 2002.
- [78] CERN web page, URL <http://proj-cngs.web.cern.ch/proj-cngs/>. Retrieved on January, 2014.
- [79] E. Gschwendtner, *The CNGS Facility: Performance and operational Experience*. 11th ICATPP Conference on Astroparticle, Particle, Space Physics, Detectors and Medical Applications, Villa Olmo, Como, Italy, 2009.
- [80] Parth Devshankar Upadhyay web page, <http://parthdu.wordpress.com/>. Retrieved on January, 2014.
- [81] M. Dracos, *Neutrinos from CERN to Gran Sasso: The CNGS project*. Journal of Physics: Conference Series, 203(1):012013, 2010.
- [82] A. Ferrari, A. Guglielmi and P. R. Sala, *CNGS neutrino beam systematics for  $\theta_{13}$* . hep-ph/0501283v1 (2005).
- [83] G. Lutter, *The OPERA experiment: Preliminary results from the 2008 run*, 0905.4521v1 [hep-ex], 2009.
- [84] C. Bozza *et al.*, Published in Nucl.Inst.Meth. A525:485-495, 2004.

## Bibliography

---

- [85] Yu. A. Gornushkin, *Search for  $\nu_\mu \rightarrow \nu_\tau$  oscillations in appearance mode in the OPERA experiment*, PACS: 14.60.Pq, 2011.
- [86] C. Jollet, *The OPERA experiment*, IReS, IN2P3-CNRS and University Louis Pasteur, 2006.
- [87] T. Adam *et al.*, *The OPERA experiment Target Tracker*. Nucl. Instr. and Meth. A, 577(3):523 – 539, 2007.
- [88] M. Dracos *et al.*, *Description of the OPERA Target Tracker (TT) production in Strasbourg*. Institut de Recherches Subatomiques, Strasbourg.
- [89] A. Anokhina *et al.*, *Emulsion sheets doublets as interface trackers for the OPERA experiment*, JINST, 3:P07005, 2008.
- [90] J. Knusel. *Development of advanced measurement techniques for emulsion films of the OPERA neutrino experiment*. Master's thesis, University Bern, LHEP, 2007.
- [91] R. Acquafredda *et al.*, *The OPERA experiment in the CERN to Gran Sasso neutrino beam*. JINST, 4(04):P04018, 2009.
- [92] A. Cazes, A. Cecchetti, B. Dulach, F. Iungo, M. Incurvati, *et al.*, *Electromagnetic characterization of the 990 ton gapless magnets for the OPERA experiment*. JINST, 2(03):T03001, 2007.
- [93] S. Dusini *et al.*, *Design and prototype tests of the RPC system for the OPERA spectrometers*. Nucl. Instr. and Meth. A, 508(1-2):175 – 180, 2003.
- [94] M. Bazzi *The I-meter, a distributor unit for the OPERA RPC HV system*. Nucl. Instr. and Meth. A, 580(3):1441 – 1445, 2007.
- [95] R. Zimmermann, J. Ebert, C. Hagner, B. Koppitz, V. Saveliev, and Y. Z. W. Schmidt-Parzefall, J. Sewing. *The precision tracker of the OPERA detector*. Nucl. Instr. and Meth. A, 555(1-2):435–450, 2005.
- [96] M. Guler *et al.*, *OPERA: An appearance experiment to search for  $\nu_\mu \rightarrow \nu_\tau$  oscillations in the CNGS beam. Experimental proposal*. CERN-SPSC-2000-028, CERN-SPSC-P-318, LNGS-P25-00, page 265, July 2000. CERN-SPSC-2000-028.
- [97] A. Bergnoli *et al.*, Nucl.Inst.Meth. A602:653-657, 2009.
- [98] K. Morishima and T. Nakano, *Development of a new automatic nuclear emulsion scanning system, S-UTS, with continuous 3D tomographic image read-out*, JINST 5 (2010) PP04011.
- [99] N. Armenise *et al.*, *High-speed particle tracking in nuclear emulsion by last generation automatic microscopes*, Nucl. Instrum. Meth. A 551 (2005) 261.
- [100] L. Arrabito *et al.*, *Track reconstruction in the emulsion-lead target of the OPERA experiment using the ESS microscope*, JINST 2 (2007) P05004.

- [101] B. Hosseini, *Neutrino Interaction Analysis with an Automatic Scanning System in the OPERA Experiment*. Master's thesis, Middle East Technical University, 2012.
- [102] C. Pistillo, *An automatic scanning system for nuclear emulsion analysis in the OPERA*, PhD. thesis, Universita degli studi di Napoli Federico II, 2004.
- [103] OPERA collaboration, N. Agafonova *et al.*, *Observation of a first  $\nu_\tau$  candidate in the OPERA experiment in the CNGS beam*, Phys. Lett. B 691 (2010) 138.
- [104] N. Agafonova and the OPERA Collaboration, *Search for  $\nu_\mu \rightarrow \nu_\tau$  oscillations with the OPERA experiment in the CNGS beam.*, New Jornal of Physics, 14(3):033017, 2012.
- [105] N. Agafonova *et al.*, *New results on  $\nu_\mu \rightarrow \nu_\tau$  appearance with the OPERA experiment in the CNGS beam*, JHEP11 (2013) 036.
- [106] N. Agafonova *et al.*, *Observation of tau neutrino appearance in the CNGS beam with the OPERA experiment*, Prog. Theor. Exp. Phys. (2014) 101C01.
- [107] N. Agafonova *et al.* (OPERA Collaboration), New J. Phys. 14, 013026 (2012).
- [108] A. Ben Dhahbi, *Nuclear Fragmentation Study in Hadron Interactions within the OPERA Experiment*, Ph.D. thesis, University of Bern (2013).
- [109] R. Brun and F. Rademakers, *ROOT - An Object Oriented Data Analysis Framework*, Nucl. Inst. Meth. in Phys. Res. A 389, 81 (1997).
- [110] ATLAS Collaboration, *ATLAS software configuration and build tool optimisation*, J.Phys.Conf.Ser. 513 (2014) 052031.
- [111] J.K. Munro *et al.*, *Use of EPICS for high level control of SNS conventional facilities*, eConf C011127 (2001) TUAP030
- [112] C. Andreopoulos *et al.*, *The GENIE Neutrino Monte Carlo Generator*. Nucl. Instrum. Meth., A614:87–104, 2010.
- [113] L. S. Esposito, *Study of electron identification in the Emulsion Cloud Chambers of the OPERA experiment*, PhD. thesis, Universita degli Studi di Bologna, 2005.
- [114] A. Bertolin *et al.*, *An algorithm for the classification of the neutrino interactions recorded by the OPERA experiment*. OPERA internal note 100, 2009.
- [115] A. Bertolin, *Analysis of the OPERA events recorded since 2008 using the Electronic Detector data*. OPERA internal note 142, 2012.
- [116] N. Agafonova *et al.*, *Study of neutrino interactions with the electronic detectors of the OPERA experiment*. New J. Phys., 13:053051, 2011.
- [117] A. Ariga. *Development and realization of a super-low-background interface detector using emulsions for the OPERA experiment*. Ph.D. thesis, Nagoya University, 2008.

## Bibliography

---

- [118] E. Segre, *Nuclei and Particles*, New York, Benjamin (1964).
- [119] B. Rossi, *High energy particles*, Prentice Hall, New Jersey (1952).
- [120] Data from J.H. Hubbell, H. Gimm, and I. Øverbø, J. Phys. Chem. Ref. Data 9, 1023 (1980); parameters for  $\sigma_{g.d.r.}$  from A. Veyssiére *et al.*, Nucl. Phys. A159, 561 (1970).
- [121] Y.S. Tsai, Rev. Mod. Phys. 46, 815 (1974).
- [122] M.J. Berger and S.M. Seltzer, *Tables of Energy Losses and Ranges of Electrons and Positrons*, National Aeronautics and Space Administration Report NASA-SP-3012 (Washington DC 1964).
- [123] W.R. Nelson, T.M. Jenkins, R.C. McCall, and J.K. Cobb, Phys. Rev. 149 (1966) 201.
- [124] G. Bathow *et al.*, Nucl. Phys. B20 (1970) 592.
- [125] A. Di Crescenzo, *Search for  $\nu_\mu \rightarrow \nu_\tau$  oscillations in the OPERA experiment*, PhD. thesis, Universita degli studi di Napoli Federico II, 2013.

# Acknowledgments

First and foremost I want to thank my supervisor Prof. Giovanni De Lellis. It has been an honor to be his Ph.D. student. He has taught me, both consciously and unconsciously, how good experimental physics is done. I appreciate all his contributions of time, ideas, and funding to make my Ph.D. experience productive and stimulating. The joy and enthusiasm he has for his research was contagious and motivational for me. Above all, you made me feel a friend, which I appreciate from my heart.

I would like to express my gratitude to Prof. Paolo Strolin, for his valuable guidance and constant encouragement.

Furthermore, I am very grateful to my internal referees Dr. Francesco Tramontano and Prof. Giuliana Fiorillo, for insightful comments both in my work and in this thesis, for their supports, and for many motivating discussions.

A special thanks goes to Guido Celentano. He has been an invaluable support during all these years.

I would also like to thank my research group members at Napoli laboratory: Adele, Cristina, Lucia, Annarita, Giuliana, Martina, Andrey, Valeri, Tatiana and especially Antonia for their friendship and their helps.

I owe much thanks to the OPERA group, which has some great people working in it. I have been very privileged to get to know and to collaborate with many of you who became friends over the last several years.

Continuing a fine tradition, I want to thank our friends in the PhD room of Napoli: Alan, Andrea, Ehsan, Mohadeseh, Fatema, Susan, Aneta, Asad, Tahmina, Oktay, Asuman and of course Deborah for their endless supports and believe in me. In fact, I am indebted to many people for making the time of my Ph.D. an unforgettable experience.

Finally, I would like to thank my mom, dad, sister, my brother in law and certainly my pretty niece Jino for their infinite support throughout everything.

